UNIVERSITY OF TRENTO

Doctoral School in Civil, Environmental and Mechanical Engineering

Curriculum 3. Modelling and Simulation

Panagiotis Koutsogiannakis

Dynamics and instability of flexible structures with sliding constraints

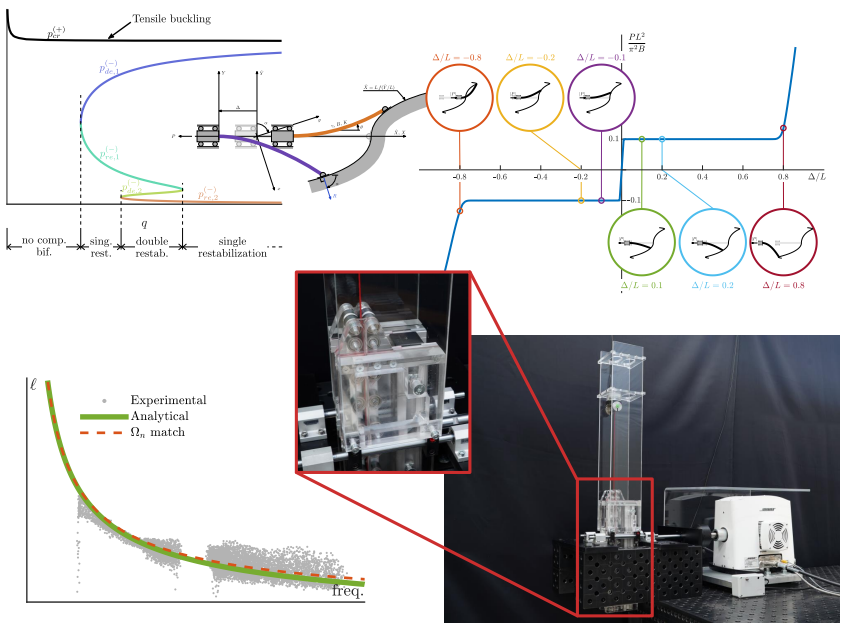

2022 - Doctoral thesis

DYNAMICS AND INSTABILITY OF FLEXIBLE STRUCTURES WITH SLIDING CONSTRAINTS

PANAGIOTIS KOUTSOGIANNAKIS

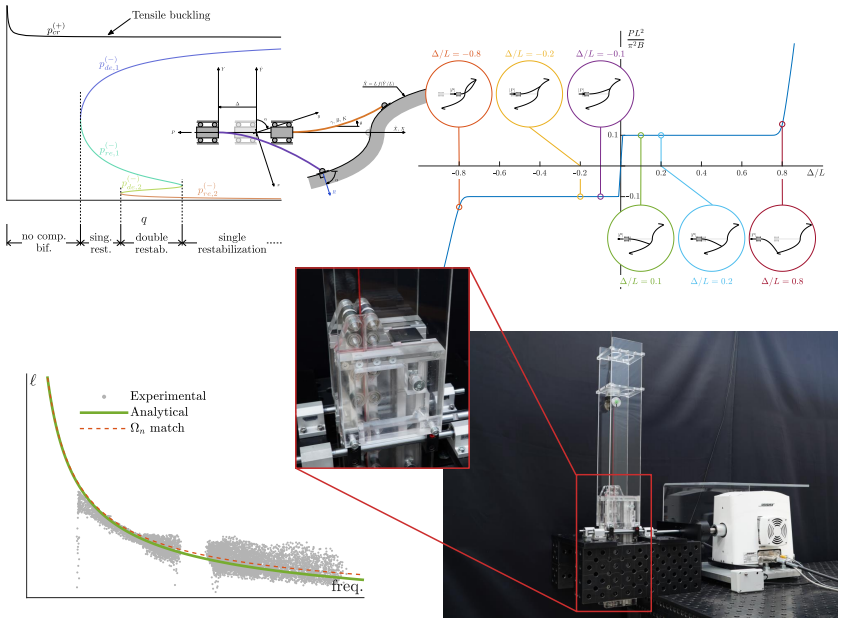

UNIVERSITÀ DI TRENTO

Department of Civil, Environmental and Mechanical Engineering
University of Trento

December 2022 – version 1.0

UNIVERSITÀ
DI TRENTO

"Logic is the foundation of the certainty
of all the knowledge we acquire."
— Leonhard Euler

ABSTRACT

Although instabilities and large oscillations are traditionally considered as conditions to be avoided in structures, a new design philosophy based on their exploitation towards the achievement of innovative mechanical features has been initiated in the last decade. In this spirit, instabilities are exploited towards the development of systems that can yield designed responses in the post-critical state. Further, the presence of oscillating constraints may allow for a stabilization of the dynamic response. These subjects entail a rich number of phenomena due to the non-linearity, so that the study of such mechanical systems becomes particularly complex, from both points of view of the mechanical modeling and of the computational tools.

Two elastic structures are studied. The first consists of a flexible and extensible rod that is clamped at one end and constrained to slide along a given profile at the other. This feature allows one to study the effect of the axial stiffness of the rod on the tensile buckling of the system and on the compressive restabilization. A very interesting effect is that in a region of parameters double restabilization is found to occur, involving four critical compressive loads. Also, the mechanical system is shown to work as a novel force limiter that does not depend on sacrificial mechanical elements. Further, it is shown that the system can be designed to be multi-stable and suitable for integration in metamaterials.

The second analyzed structure is a flexible but inextensible rod that is partially inserted into a movable rigid sliding sleeve which is kept vertical in a gravitational field. The system is analytically solved and numerically and experimentally investigated, when a horizontal sinusoidal input is prescribed at the sliding sleeve. In order to model the system, novel computational tools are developed, implementing the fully nonlinear inextensibility and kinematic constraints. It is shown that the mathematical model of the system agrees with the experimental data. Further, a study of the inclusion of dissipative terms is developed, to show that a steady motion of the rod can be accomplished by tuning the amplitude or the frequency of the sliding sleeve motion, in contrast with the situation in which a complete injection of the rod inside the sleeve occurs. A special discovery is that by slowly decreasing the frequency of the sleeve motion, the length of the rod outside the sleeve can be increased significantly,

paving the way to control the rod's end trajectory through frequency modulation.

PUBLICATIONS

Some ideas and figures have appeared previously in the following publication:

[1] P. Koutsogiannakis, D. Bigoni, and F. Dal Corso. "Double restabilization and design of force–displacement response of the extensible elastica with movable constraints." In: *European Journal of Mechanics - A/Solids* (2022), p. 104745. ISSN: 0997-7538. DOI: 10.1016/j.euromechsol.2022.104745.

ACKNOWLEDGEMENTS

In all honesty, I would like to thank the few true friends that stood by me during my studies in the University of Trento. But above all I feel the need to acknowledge my two great advisors Prof. Davide Bigoni and Prof. Francesco Dal Corso that proved to be amazing mentors and taught me well in the field of structural mechanics research, but also about academia and life in general. On that note, I would like to thank Prof. Theodosios Papathanasiou for his help and the useful discussions about numerical methods, and Prof. Diego Misseroni for his invaluable help with the conception and realization of the experimental setup of the oscillating sliding sleeve. Without all of them the quality of my research, carried out in the last three years, would have suffered greatly and I deeply thank them for everything.

Also, I would like to acknowledge the financial support from the European Union's Horizon 2020 research and innovation programme under the Marie Sklodowska-Curie grant agreement "INSPIRE - Innovative ground interface concepts for structure protection" PITN-GA-2019-813424-INSPIRE. But, the project is also the people of the consortium that were excellent collaborators and I would like to thank them for a very successful project. More specifically, I would like to thank the fellow Early Stage Researchers of my work package with whom we worked closer for compiling deliverables for the project and most importantly Marianna Loli for the excellent coordination of the project.

Finally, it goes without saying that the last three years were difficult also from the perspective of the pandemic that disrupted my life only three months after the start of my studies in Trento. Many weeks of isolation, long quarantines, heavy mobility restrictions and getting Covid twice, were enough to delay training activities, experiments and managed to introduce heavy stress in my life. In this regard, I would like to say to the tiny little virus: "Thanks for nothing..."

CONTENTS

LIST OF FIGURES

LIST OF TABLES

1 INTRODUCTION

Differently from linearized analysis, nonlinear models may lead to a non-uniqueness of the equilibrium, or dynamic, solution. The presence of multiple solutions can drive the change from stability to instability along a loading path, realized through a bifurcation or a snap-mechanism. Bifurcations are referred to the emergence of non-trivial modes, emanating from a trivial configuration. Examples come from diverse fields such as Engineering, Theoretical Physics (e.g. quantum bifurcations), Chemistry (e.g. bifurcating reactions), Biology and Ecology (e.g. three-species predator-pray models [61]). The term *bifurcation* was first used by Henri Poincaré in 1885 in the first scientific article showing the described behaviour in mathematics [43]. The phenomenon of bifurcation is closely tied to the *chaos theory*, as nonlinear dynamics lead to *period doubling* bifurcations and subsequently to non-periodic solutions for systems under periodic excitation [53]. The logistic map is another example of bifurcation and chaos in mathematics.

In a similar manner, of importance in many scientific fields are also the effects of instabilities. In a dynamic context, the term *instability* is used to describe a configuration on the equilibrium path for which a small deviation from the path implies a divergence when the system is evolved in time. In similar manner, the configuration is deemed *stable* when the deviated system converges back to the original equilibrium path.

Bifurcations and instabilities are strongly associated with one another, as in many cases the appearance of an instability implies a bifurcation in the equilibrium path. The most usual example is that of the buckling of beams subject to an axial load; see Fig. 1.

The study of instabilities of structures subject to these types of constraint is motivated by the possible disclosure of unexpected mechanical features that can be exploited to attain a designed response. The phrase ”transition from buckliphobia to buckliphilia” has been used to describe the current trend of exploring the advantageous properties of buckling structures [45]. The term ”buckliphobia” refers to the traditional thought that buckling has catastrophic consequences for the mechanical properties of a structure and as a result should be avoided at all cost. This is true for structures that are designed to display negligible deformations

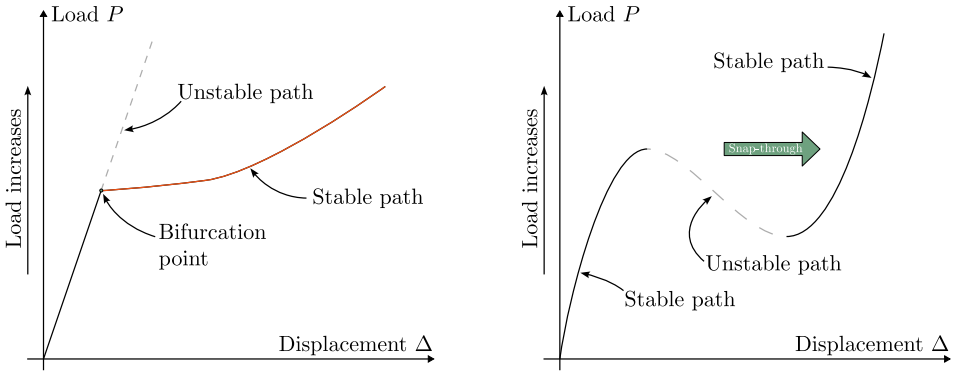

Figure 1: Typical instabilities in structural mechanics. (Left) Typical bifurcations of the equilibrium path related to the buckling of beams, (Right) Snap-through instability of a bistable structure (load-controlled conditions).

or rotations. However, recent advances in structural mechanics aim to produce structures that take advantage of structural instabilities in order obtain behaviours that are not possible or very difficult to obtain using mainstream designs, such as reconfigurable structures or designed mechanical properties. In that respect, instabilities are no longer considered catastrophic and undesirable effects but can be exploited to attain desirable properties from mechanical systems.

A first example of a reconfigurable structure is the "Buckliball", as the Authors of the original research paper called the spherical structure that was introduced as a first example of a new class of structures that can alter their configuration through pneumatic actuation [51]. The "buckliball" is a spherical shell with a pattern of voids cut out. When subject to a negative internal pressure, the structure folds and its size changes uniformly due to a negative Poison's ratio that results from the void pattern [8].

Building upon the work of the "buckliball", another example of a reconfigurable structure is a thin-stiff spherical shell attached to a thick-soft inner substrate that can produce a wrinkling pattern when subject to uniform stress [16]. The pattern on the structure surface can be altered through pneumatic actuation and the system has been used to change on demand the aerodynamic properties of a ball [56].

In a similar fashion, buckling has been used to create functional 2D microstructures [63]. These structures consist of thin ribbons that when stressed fold into predetermined configurations, such as coils, helices and a variety of more complex shapes. Also, nested structures can be created or the structures can be repeated to create interconnected 3D networks

that extend from the microscale to the mesoscale. Such microstructures can produce novel tunable electric, magnetic and mechanical microsystems.

Further, novel reconfigurable structures that exhibit designed mechanical properties have been inspired by the Japanese arts of folding and cutting paper, origami and kirigami respectively. These structures are used in compliant mechanisms [39, 40, 44], multistable mechanisms [44, 60], and proposed as building blocks of mechanical metamaterials [22, 29, 39, 44, 60].

In another example, buckling has been exploited to display zero or negative stiffness [11, 21, 31, 34], and designed force-displacement response [36, 54, 65, 67].

Potential applications for instability powered mechanisms include technologies for energy harvesting [22, 41], where snap-through instabilities provide fast kinematics and self-tuning properties [25], and for energy dissipation [4, 21, 31, 62].

In the present work structural instabilities are studied and more specifically instabilities of elastic rods subject to non-standard constraints. By the term *non-standard constraint* it is meant a constraint different than the traditional clamp and hinge constraints fixed in space. In particular, two types of constraints are considered in the present work. The first, a sliding profile, generalizes the hinge by assuming that the constrained point of the rod is able to move along a predefined profile, while the second, the sliding sleeve, generalizes the clamp by allowing the rod to slide inside the clamp. In order to study the effects of these constraints, two specific systems were devised and are briefly presented in the following sections of this chapter.

1.1 THE SLIDING PROFILE SYSTEM

This system is composed of an elastic rod that has one of its ends attached to a clamp that can move along the axis parallel to the undeformed rod and the other end attached to a hinge that is allowed to slide along a predetermined curved profile; see Fig. 2. The profile is designed such that in the unloaded condition the rod is perpendicular to the profile at the point of contact. When a force is applied to the clamped end, the rod remains in a straight configuration until the force reaches a critical value, either in compression or in tension, providing a buckling of the rod. This critical load depends on the curvature at the point of contact, while the

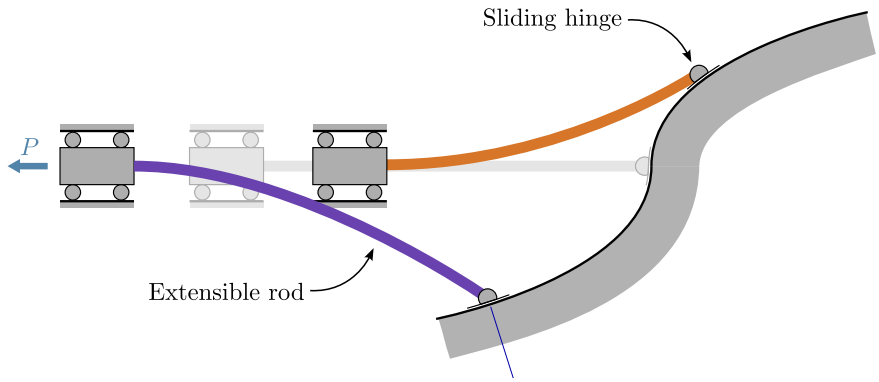

Figure 2: The sliding hinge system. The system is composed of an elastic rod that has one of its ends attached to a clamp that can move along the axis parallel to the undeformed rod and the other end attached to a hinge that is allowed to slide along a predetermined curved profile.

force-displacement behaviour of the system in the post-critical regime is determined by the whole shape of the profile.

From a theoretical point of view this system shows a variety of interesting phenomena, such as tensile buckling and negative stiffness. The system, originally proposed for the case of an inextensible rod along with an equivalent single degree of freedom system [11], is enhanced through the introduction of extensibility. Therefore, in addition to buckling, the rod displays a restabilization that appears as it reaches a length too short to make the trivial straight configuration unstable. Under specific properties of the profile shape, the system is shown to exhibit a double restabilization, meaning that the first restabilization is followed by a second buckling and a second restabilization as compression increases. In other words, the straight configuration loses stability twice and recovers it twice.

Practical examples for this structural system are force-limiters that can be designed to take advantage of the buckling of beams to activate, used to prevent unbounded growth of a force applied to a sensitive element. In this device, when a certain threshold of force is attained, the (incremental) stiffness vanishes, thus allowing the displacement to grow. This occurs until a certain limit stroke is reached, at which the device finally locks. If the force-limiter is purely elastic, dissipation is prevented, so that the displacement decreases back to zero when the force is released. A small positive incremental stiffness provides a mechanism for resetting the de-

vice once the force is small enough. Another advantage of this system is that the elastic buckling of the beam provides an activation mechanism that does not require the use of sacrificial elements. Force-limiting mechanisms may be used to bound the force transmitted during an impact, as is the case of automotive seat belt systems, where plastic deformation developing in mechanical elements prevents reuse of the device [7, 17, 19].

Another crucial application is for vibration isolation of scientific and measuring equipment [1, 28, 47], (e.g. optical tables [58]), or of gravitational-wave detection laboratories [20], but also of civil structures to be shielded from earthquakes [2, 32, 49].

Furthermore, the designed force-displacement curve can be enhanced to exhibit multistability, as in reconfigurable metamaterials for shock absorption [64], shape programming [55], elastic energy trapping [50], and wave guiding [30]. Several structural schemes have been so far proposed for these purposes, most incorporating negative stiffness elements, such as magnetic springs for active vibration control [48, 68, 69], oblique mechanical springs [18], extremely deformable [57], or buckling [38, 62] beams.

An extensive analysis of the sliding profile system is presented in Chapter 3.

1.2 THE SLIDING SLEEVE SYSTEM

The sliding sleeve system consists of a rod partially inserted within a frictionless and rigid sliding sleeve and with a mass attached at the tip of the rod outside this constraint; see Fig. 3. The quasi-static case of a rod constrained by a fixed sliding sleeve is studied in [12], where it is demonstrated for the first time the realization of an outward configurational force at the constraint, parallel to the sliding direction, as effect of a curvature discontinuity point moving along the elastic rod. The dynamic response of the same system within a gravitational field is studied in [3], showing complex dynamic transients ending with a complete injection or complete ejection of the elastic rod, towards the two trivial attractors of the dynamical system where the length external to the constraint becomes zero or infinite.

The oscillation of the sliding sleeve constraint provides an external input that allows the system to exhibit a quasi-periodic motion, without injecting into or ejecting out of the sliding sleeve. This may also occur

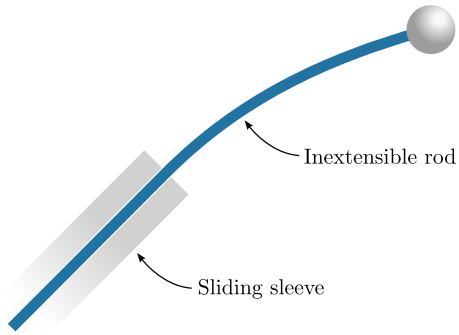

Figure 3: The sliding sleeve system. The system consists of a rod partially inserted within a frictionless and rigid sliding sleeve and with a mass attached at the tip of the rod outside this constraint.

even though the amplitude of the input motion is small, relative to the dimensions of the system and relative to the displacement of the mass at the tip of the rod. More specifically, the sliding sleeve oscillation can be interpreted as capable to introduce a third attractor associated with a finite external length, in addition to the two trivial one of null and infinite length. The third attractor is then realized as the result of a balance in average sense over the time of the configurational force and the gravitational force.

The configurational force constitutes the main driving force of excitation of the system. The term configurational force is chosen due to the fact that the force mainly depends on the configuration of the rod-sleeve system regardless of its dynamic state. These are *Eshelby-like* forces named after Eshelby that first introduced them in solid mechanics to model forces driving crack propagation.

The oscillating sliding sleeve system is discussed in detail in Chapter 4. It is shown to have self-tuning properties, a desirable effect in applications such as energy harvesting and energy dissipation. Mechanisms incorporating the sliding sleeve can be considered for applications in resonant metamaterials.

1.3 MATHEMATICAL MODELING OF THE SYSTEMS

Even in the simplest case that the material properties are linear, the study of buckling structures entails larger deflections and geometric nonlinearities. Therefore, linear models that work well under the assumption

of small deformations, as well as standard analysis techniques that are adapted to linear problems, are not sufficient and more sophisticated methods are required.

In order to study the two systems described above, analytical and numerical models are developed. Concerning the analytical models, a closed form solutions of the extensible and the inextensible elasticae are employed. Subsequently, a Finite Element framework is developed as an effort to gain a more accurate model that includes the mass of the rod and distributed forces.

For the sliding hinge system, the closed-form solution for a cantilever beam with a force imposed at the free end provided in [6] is exploited. In particular, this solution, based on Jacobi elliptic functions as an improvement over the elliptic integral approaches considered before [26, 27, 37, 42, 52]. For the sliding sleeve system the solution of the inextensible elastica presented in [3] is used. Further, a finite element formulation of the sliding sleeve constraint is developed as an extension of the method provided in [5].

For the purposes of evolving in time the theoretical models a variety of numerical methods are tested. More specifically, for the time integration of the elastica models a Crank-Nicolson scheme is used, and for the finite element model an Implicit Euler method is selected.

The theoretical background of these models is provided in Chapter 2.

2 THEORETICAL BACKGROUND

In this chapter the theoretical background, the mathematical models and the numerical methods used in the next chapters are presented. First the static and dynamic models for the elastica are defined for the most general case that takes into account the extensibility of the elastic rod and then the case of the inextensible elastica is discussed. Following this, the numerical finite element methods are briefly presented. The models and methods presented in this chapter will be adapted to the specific problems solved in the subsequent chapters.

2.1 THE QUASI-STATIC MODEL FOR THE EXTENSIBLE ELASTICA

The closed form solution of the extensible elastica of undeformed length L is used to solve the governing equations in the quasi-static case, as a simplification that ignores the density of the rod and other distributed forces along the rod. The solutions are obtained for the case of the elastica clamped at one end at some angle α and loaded at the other one through a force of magnitude $R(t)$ and inclination angle $\beta(t)$ with respect to the clamp inclination, as shown in Fig. 4. The solution is obtained in the rotated coordinate system x-y, rotated by the angle $\alpha + \beta(t)$, and the deformation of the rod is described through the rotation $\theta(s)$ and the axial strain $\varepsilon(s)$ fields function of the curvilinear coordinate $s \in [0, L]$.

KINEMATICS The deformed rod's configuration can be described in the rotated reference frame x-y with varying the coordinate s through the integration of the $\theta(s)$ and $\varepsilon(s)$[1] fields as follows

$$\begin{aligned} x(s,t) &= \int_0^s [1+\varepsilon(\sigma,t)]\cos(\theta(\sigma,t)+\beta(t))\,d\sigma, \\ y(s,t) &= \int_0^s [1+\varepsilon(\sigma,t)]\sin(\theta(\sigma,t)+\beta(t))\,d\sigma, \end{aligned} \tag{1}$$

1 In order to simplify the notation, from this point forward the time variable t is omitted in the argument list of time-varying quantities and it is implied wherever time-dependent quantities are considered. When confusion may arise, the time variable will be explicitly provided.

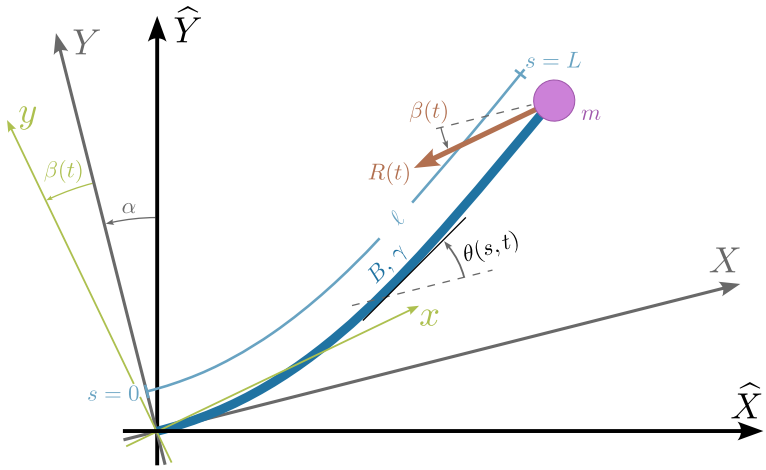

Figure 4: The simplest problem of the elastica considered in the present work. The rod of length L and flexural stiffness B is clamped on one end at an angle alpha and a concentrated mass m is attached to the rod tip. A general force R is applied to the mass.

or in the original reference frame X-Y as

$$\begin{aligned} X(s,t) &= \int_0^s [1+\varepsilon(\sigma,t)]\cos(\theta(\sigma,t))d\sigma, \\ Y(s,t) &= \int_0^s [1+\varepsilon(\sigma,t)]\sin(\theta(\sigma,t))d\sigma, \end{aligned} \tag{2}$$

by considering that both reference systems have their origin at the position of the clamped end of the rod (curvilinear coordinate $s = 0$), namely, $X(0,t) = Y(0,t) = x(0,t) = y(0,t) = 0$. The equations above imply the following transformation

$$X(S) = x(S)\,\cos\beta + y(S)\,\sin\beta, \quad Y(S) = -x(S)\,\sin\beta + y(S)\,\cos\beta, \tag{3}$$

between the x-y reference system and the X-Y reference system. The position of the elastica with a clamp rotated by an angle α with respect to a given reference frame $\widehat{X}$ - $\widehat{Y}$ can be found by applying the rotation

$$\begin{aligned} \widehat{X}(s) &= X(s)\,\cos\alpha + Y(s)\,\sin\alpha, \\ \widehat{Y}(s) &= -X(s)\,\sin\alpha + Y(s)\,\cos\alpha. \end{aligned} \tag{4}$$

STATICS The total potential energy of the deformed elastic curve can be written as

$$\mathcal{V}_{ext}(\varepsilon,\theta) = \frac{K}{2}\int_0^L [\varepsilon(\sigma)]^2\,d\sigma + \frac{B}{2}\int_0^L \left[\theta'(\sigma)\right]^2 d\sigma + R\,x(L), \tag{5}$$

where a prime stands for differentiation with respect to the relevant (spatial) argument. The first variation $\delta\mathcal{V}$ of the potential energy for perturbations in the strain $\delta\varepsilon$ and rotation $\delta\theta$ is given by

$$\delta\mathcal{V}_{ext} = \int_0^L K\,\varepsilon(\sigma)\,\delta\varepsilon(\sigma)\;d\sigma - \int_0^L B\,\theta''(\sigma)\,\delta\theta(\sigma)\;d\sigma + R\,\delta x(L), \tag{6}$$

where

$$\begin{aligned}\delta x(s) = &-\int_0^s [1+\varepsilon(\sigma)]\sin(\theta(\sigma)+\beta)\delta\theta(\sigma)\,d\sigma \\ &+\int_0^s \delta\varepsilon(\sigma)\cos(\theta(\sigma)+\beta)\,d\sigma,\\ \delta y(s) = &\int_0^s [1+\varepsilon(\sigma)]\cos(\theta(\sigma)+\beta)\delta\theta(\sigma)\,d\sigma \\ &+\int_0^s \delta\varepsilon(\sigma)\sin(\theta(\sigma)+\beta)\,d\sigma.\end{aligned} \tag{7}$$

From Eq. (6) and (7) the following governing equations can be derived

$$\begin{aligned}&B\,\theta''(s) + R\,[1+\varepsilon(s)]\sin(\theta(s)+\beta) = 0,\\ &K\,\varepsilon(s) + R\sin(\theta(s)+\beta) = 0.\end{aligned} \tag{8}$$

CLOSED-FORM SOLUTION For the extensible elastica, the closed-form solution for a cantilever beam with a concentrated load at the free end has been derived by Batista [6]. This solution is exploited here in the case of unshearable rod (parameter $\nu = 1$ in [6]).

Introducing the following non-dimensional parameters[2]

$$\rho^2 = \frac{R\,L^2}{B}, \quad \lambda = L\sqrt{\frac{K}{B}}, \quad \hat{s} = \frac{s}{L}, \tag{9}$$

the rotation $\theta(s)$ and strain $\varepsilon(s)$ fields are given by

$$\begin{aligned}\theta(s) &= 2\arcsin\left[k\frac{\operatorname{sn}(\tilde{\rho}\,\hat{s}+C,\tilde{k})}{\sqrt{1+m^2\operatorname{cn}^2(\tilde{\rho}\,\hat{s}+C,\tilde{k})}}\right] - \beta,\\ \varepsilon(s) &= -\frac{\rho^2}{\lambda^2}\cos(\theta(s)+\beta),\end{aligned} \tag{10}$$

2 It should be noted that here the symbol ρ is used instead of ω used originally in [6] in order to not create confusion with the analogous symbols used to denote the angular frequencies in Sect. 3.3.2.

where

$$m^2 = \frac{\frac{\rho^2 k^2}{\lambda^2}}{1 - \frac{\rho^2(1-k^2)}{\lambda^2}}, \quad \tilde{\rho} = \rho\sqrt{1 + \frac{\rho^2(2\,k^2-1)}{\lambda^2}}, \quad \tilde{k}^2 = \frac{k^2+m^2}{1+m^2}. \tag{11}$$

The integration of the kinematic fields $(10)_1$ through Eq. (1) provides the position of the rod, in the rotated reference frame, at the curvilinear coordinate s as

$$\begin{aligned} x(s) = \; & \frac{2\tilde{\rho}}{\rho^2}\left\{\left(\frac{E(\tilde{k})}{K(\tilde{k})} - \frac{1}{2}\right)\tilde{\rho}\,\hat{s} + Z(\tilde{\rho}\,\hat{S} + C, \tilde{k}) - Z(C, \tilde{k})\right. \\ & -m^2\left[\frac{sn(\tilde{\rho}\hat{s}+C,\tilde{k})\,cn(\tilde{\rho}\hat{S}+C,\tilde{k})\,dn(\tilde{\rho}\hat{s}+C,\tilde{k})}{1+m^2\,cn^2(\tilde{\rho}\hat{s}+C,\tilde{k})}\right. \\ & \left.\left.-\frac{sn(C,\tilde{k})\,cn(C,\tilde{k})\,dn(C,\tilde{k})}{1+m^2\,cn^2(C,\tilde{k})}\right]\right\} L, \end{aligned} \tag{12}$$

$$\begin{aligned} y(s) = \; & \frac{2\,k\,\tilde{\rho}\,\sqrt{1+m^2}}{\rho^2}\left[\frac{cn(C,\tilde{k})}{1+m^2\,cn^2(C,\tilde{k})}\right. \\ & \left.-\frac{cn(\tilde{\rho}\hat{s}+C,\tilde{k})}{1+m^2\,cn^2(\tilde{\rho}\hat{s}+C,\tilde{k})}\right] L, \end{aligned}$$

while the rod's curvature $\kappa(s) = \theta'(s)$ follows as

$$\kappa(s) = \frac{1}{L}\frac{2\,\tilde{\rho}\,k\,\sqrt{1+m^2}\,cn(\tilde{\rho}\,\hat{s}+C,\tilde{k})}{1+m^2\,cn^2(\tilde{\rho}\,\hat{s}+C,\tilde{k})}. \tag{13}$$

In the above equations, K and E are the complete elliptic integrals of the first and second kind, Z, sn, cn, dn are Jacobi elliptic functions, and C is the constant of integration that can be found by imposing the boundary condition of zero bending moment, equivalent to null curvature, at the free end, $\theta'(L) = \kappa(L) = 0$.

From the boundary condition of null rotation at the clamp, $\theta(0) = 0$, the following equation is obtained

$$k\frac{sn(C,\tilde{k})}{\sqrt{1+m^2\,cn^2(C,\tilde{k})}} - \sin\frac{\beta}{2} = 0, \tag{14}$$

to be solved for the value of k. The boundary condition at the right end $\kappa(L) = 0$ yields a formula for C

$$C = -\tilde{\rho} + (2n-1)\,K(\tilde{k}), \qquad n \in \mathbb{N}^+, \tag{15}$$

where n is the mode number. Once k is determined, the coordinates of the curve in the rotated reference frame $x-y$ can be evaluated from Eq. (12), and those in the reference frame $X-Y$ from Eq. (3).

Because $\kappa(L) = 0$, the parameter k can be related with the rotation of the beam at the free end $\theta_L = \theta(L)$, by evaluating (10) at $s = L$, through the following formula

$$k = \sin\frac{\theta_L + \beta}{2}. \tag{16}$$

2.2 THE QUASI-STATIC MODEL FOR THE INEXTENSIBLE ELASTICA

The inextensible elastica can be obtained from the extensible case by imposing the constraint that the axial strain ε is zero.

KINEMATICS Under the assumption of null axial strain the position of the elastic curve becomes

$$\begin{aligned} x(s) &= \int_0^s \cos(\theta(\sigma) + \beta)\, d\sigma, \\ y(s) &= \int_0^s \sin(\theta(\sigma) + \beta)\, d\sigma. \end{aligned} \tag{17}$$

STATICS In order to find the deformation of the inextensible elastica the following constraint is imposed

$$\varepsilon(s) = 0 \quad \forall s \in (0, L), \tag{18}$$

implying that the measure of the tangent vector to the elastic curve is equal to one, $\|(X'(s), Y'(s))\| = 1$, and

$$X'(s) = \cos\theta(s), \qquad Y'(s) = \sin\theta(s). \tag{19}$$

Then, the total potential energy of the inextensible system can be written as

$$\mathcal{V}_{inext} = \mathcal{V}_{ext} - \int_0^L N(\sigma)\varepsilon(\sigma)\, d\sigma, \tag{20}$$

where N is a lagrange multiplier and in the physical model coinsides with the axial component of the internal force. The governing equations in the weak form can be written as

$$\delta\mathcal{V}_{inext} = \delta\mathcal{V}_{ext} - \int_0^L N(\sigma)\delta\varepsilon(\sigma)\, d\sigma = 0, \tag{21}$$

and in strong form as

$$\begin{aligned} &B\theta''(s) + R\sin(\theta(s)+\beta) = 0, \\ &N = R\cos(\theta(s)+\beta). \end{aligned} \tag{22}$$

CLOSED-FORM SOLUTION The closed form solution of the inextensible elastica can also be adapted from [6] by setting $\nu = 0$. Then, the constants m^2,$\tilde{\rho}$ and $\tilde{k}$ become

$$m^2 = 0, \quad \tilde{\rho} = \rho, \quad \tilde{k}^2 = k^2, \tag{23}$$

and the rotation $\theta(s)$ field is given by

$$\theta(s) = 2\arcsin\left[k\,sn(\rho\,\hat{s} + C, k)\right] - \beta. \tag{24}$$

The integration of the kinematic field (24) through Eq. (1) provides the position of points on the rod, in the rotated reference frame, at the curvilinear coordinate s as

$$\begin{aligned} x(s) = &\quad -\frac{\rho^2}{2\lambda^2}\hat{s} + \frac{2L}{\rho}\left\{\left(\frac{E(k)}{K(k)} - \frac{1}{2}\right)\rho\,\hat{s} + Z(\rho\,\hat{s} + C, k) - Z(C, k)\right\}, \\ y(s) = &\quad \frac{2\,k\,L}{\rho}\left[cn(C, k) - cn(\rho\hat{s} + C, k)\right], \end{aligned} \tag{25}$$

while the rod's curvature $\kappa(s) = \theta'(s)$ follows as

$$\kappa(s) = \frac{2\,\rho\,k}{L}\,cn(\rho\,\hat{s} + C, k). \tag{26}$$

In the above equations, K and E are the complete elliptic integrals of the first and second kind, Z, sn, cn, dn are Jacobi elliptic functions, and C is the constant of integration that can be found by imposing the boundary condition of zero bending moment, equivalent to null curvature, at the free end, $\theta'(L) = \kappa(L) = 0$.

From the boundary condition of null rotation at the clamp, $\theta(0) = 0$, the following equation is obtained

$$k\,sn(C, k) - \sin\frac{\beta}{2} = 0, \tag{27}$$

to be solved for the value of k. The boundary condition at the right end $\kappa(L) = 0$ yields a formula for C

$$C = -\rho + (2n - 1)\,K(k), \qquad n \in \mathbb{N}^+, \tag{28}$$

where n is the mode number. Once k is determined, the coordinates of the curve in the rotated reference frame $x - y$ can be evaluated from Eq. (25), and those in the reference frame $X - Y$ from Eq. (3).

2.3 THE DYNAMIC MODEL FOR THE EXTENSIBLE ELASTICA

Here the mass of the system is thought to be composed by a distributed mass of linear density γ and a concentrated mass m at the free end of the elastica, and in the most general case of a distributed force $w(s)$ at an angle $\beta_w(s)$ with respect to the x axis along the entire rod, in addition to the concentrated load R. For simplicity the rotational inertia of the elastica is neglected.

The total potential energy of the system is

$$\begin{aligned} \mathcal{V}_{ext}^{dyn} &= \mathcal{V}_{ext}(\varepsilon,\theta) \\ &- \int_0^L w(\sigma)\cos(\beta_w(\sigma))\,x(\sigma)\,d\sigma + \int_0^L w(\sigma)\sin(\beta_w(\sigma))\,y(\sigma)\,d\sigma, \end{aligned} \tag{29}$$

and the kinetic energy is

$$\mathcal{T}^{dyn} = \frac{1}{2}\int_0^L \gamma(\dot{x}^2(\sigma)+\dot{y}^2(\sigma))\,d\sigma + \frac{1}{2}m(\dot{x}^2(L)+\dot{y}^2(L)). \tag{30}$$

The Lagrangian of the system is

$$\begin{aligned} \mathcal{L}_{ext} &= \mathcal{T}^{dyn} - \mathcal{V}_{ext}^{dyn} \\ &- \int_0^L N_x(\sigma)[x'(\sigma)-(1+\varepsilon(\sigma))]\cos(\theta(\sigma+\beta))\,d\sigma \\ &- \int_0^L N_y(\sigma)[y'(\sigma)-(1+\varepsilon(\sigma)))\sin(\theta(\sigma+\beta)]\,d\sigma. \end{aligned} \tag{31}$$

Through the Hamiltonian Principle the following equations of motion can be derived

$$\begin{aligned} &N_x'(s) = \gamma\ddot{x}(s) + w(s)\cos(\beta_w(s)), \\ &N_y'(s) = \gamma\ddot{y}(s) - w(s)\sin(\beta_w(s)), \\ &K\varepsilon(s) - N_x(s)\cos(\theta(s)+\beta) - N_y(s)\sin(\theta(s)+\beta) = 0, \\ &B\theta''(s) - (1+\varepsilon(s))[N_x(s)\sin(\theta(s)+\beta) + N_y(s)\cos(\theta(s)+\beta)] = 0, \end{aligned} \tag{32}$$

complemented by the following natural boundary conditions

$$\theta'(L) = 0, \qquad N_x(L) = -m\ddot{x}(L) - R, \quad N_y(L) = -m\ddot{y}(L). \tag{33}$$

THE CASE OF NO DISTRIBUTED MASS AND NO DISTRIBUTED FORCES

In the special case that the distributed mass and the distributed forces are thought to be negligible the equations of motion (32) become

$$\begin{aligned} &N_x'(s) = 0, \\ &N_y'(s) = 0, \\ &K\varepsilon(s) - N_x(s)\cos(\theta(s)+\beta) - N_y(s)\sin(\theta(s)+\beta) = 0, \\ &B\theta''(s) - (1+\varepsilon(s))[N_x(s)\sin(\theta(s)+\beta) + N_y(s)\cos(\theta(s)+\beta)] = 0. \end{aligned} \tag{34}$$

In this case the internal forces $N_x(s)$ and $N_y(s)$ become constant

$$N_x(s) = \overline{N}_x, \qquad N_y(s) = \overline{N}_y, \tag{35}$$

and their values can be found from the boundary conditions (33)

$$\overline{N}_x = -m\ddot{x}(L) - R, \qquad \overline{N}_y = -m\ddot{y}(L). \tag{36}$$

Since the distributed effects are neglected, the quasistatic solution of the extensible elastica can be exploited in order to derive a solution to the dynamic system of equations. For this reason the total force

$$\tilde{\mathbf{R}} = (-\overline{N}_x, -\overline{N}_y)^T \tag{37}$$

applied to the free end of the elastica is defined, along with the corresponding angle $\tilde{\beta}$ as

$$\tilde{R}(t) = \sqrt{\overline{N}_x^2(t) + \overline{N}_y^2(t)}, \qquad \tan\tilde{\beta}(t) = -\frac{\overline{N}_y(t)}{\overline{N}_x(t)}, \tag{38}$$

and $\overline{N}_x$, and $\overline{N}_y$ can be written as

$$\overline{N}_x(t) = -\tilde{R}(t)\cos\tilde{\beta}(t), \qquad \overline{N}_y(t) = -\tilde{R}(t)\sin\tilde{\beta}(t). \tag{39}$$

Next, the equations of motion can be written as

$$\begin{cases} \overline{N}_x(t) = -m\ddot{x}_L(t) - R(t), \\ \\ \overline{N}_y(t) = -m\ddot{y}_L(t), \\ \\ k(t)\dfrac{\operatorname{sn}(C(t),\tilde{k}(t))}{\sqrt{1+m^2\operatorname{cn}^2(C(t),\tilde{k}(t))}} - \sin\dfrac{\beta(t)+\tilde{\beta}(t)}{2} = 0, \end{cases} \tag{40}$$

where the latter equation is the condition for null rotation at the clamp as defined in Eq. (14). This system of equations can be evolved in time for the variables $x_L(t)$, $y_L(t)$, and $\theta_L(t)$ or alternatively for the quantities $\tilde{R}(t)$, $\tilde{\beta}(t)$, and $\theta_L(t)$. For this reason, the connection between the total force $\tilde{R}(t)$ and the coordinates $x_L(t)$, $y_L(t)$ is provided through Eqs. (12).

2.4 THE DYNAMICS OF THE INEXTENSIBLE ELASTICA

In similar fashion to the quasi-static case for the inextensible elastica, the equations of motion can be derived from the extensible case by applying the constraint $\varepsilon(s) = 0$. In this case the solution can be given in a closed form using the quasi-static solution as seen in the previous paragraph. The equations of motion in this case become

$$\begin{cases} \overline{N}_x(t) = -m\,\ddot{x}_L(t) - R(t), \\ \\ \overline{N}_y(t) = -m\,\ddot{y}_L(t), \\ \\ k(t)\,\mathrm{sn}(C(t), k(t)) - \sin\dfrac{\beta(t) + \tilde{\beta}(t)}{2} = 0. \end{cases} \tag{41}$$

Similarly to the extensible case, the relation between the total force $\tilde{R}$ and the coordinates $x_L(t)$, $y_L(t)$ is provided through Eqs. (25).

2.5 POSITION-BASED INEXTENSIBLE ELASTIC CURVE DYNAMICS

The position of the elastic curve $\mathbf{X}(s,t)$ is parametrized by a curvilinear parameter $s \in \Omega = [0, L]$ that runs along its length. A vector tangent to the curve can be obtained by differentiating the curve with respect to the parameter s and a vector normal to the curve is given by a second differentiation of the curve with respect to s. The case where a distributed force $\mathbf{w}(s,t)$ is applied on the elastica is considered here.

In order to produce the equations of motion, the inextensibility condition has to be treated. The inclusion of this constraint in the model produces a system of Differential Algebraic Equations (DAE). The inextensibility condition means that the modulus of the first derivative of the arc-length parametrized curve is equal to one and mathematically it is written as

$$\|\mathbf{X}'(s,t)\| = 1 \qquad \forall\, s \in [0, L]\, \forall t, \tag{42}$$

or equivalently

$$\|\mathbf{X}'(s,t)\|^2 = \mathbf{X}'(s,t) \cdot \mathbf{X}'(s,t) = 1 \qquad \forall\, s \in [0, L],\ \forall t. \tag{43}$$

It should be noted here that the inextensibility condition (43) is imposed directly in contrast with a common technique of differentiating the constraint in time to reduce the index of the final system of DAEs, as in [5].

This is to eliminate any drifting effects, that would be detrimental to the accuracy of long simulations.

In addition to the inextensibility condition, the following boundary conditions are applied, due to the clamp,

$$\begin{aligned} &\mathbf{X}(0,t) = \mathbf{O}, \\ &\mathbf{n}(t) \cdot \mathbf{X}'(0,t) = 0, \end{aligned} \tag{44}$$

where $\mathbf{n}(t)$ is the unit vector normal to the direction of the clamp.

The kinetic energy of the system is

$$\mathcal{T}(t) = \int_0^L \frac{1}{2}\gamma \left(\dot{\mathbf{X}}(s,t)\right)^2 \, ds, \tag{45}$$

and the total potential energy can be written as the sum of the bending energy stored in the elastic curve and the work of the distributed force $\mathbf{w}$

$$\mathcal{V}(t) = \int_0^L \frac{1}{2} B \left(\mathbf{X}''(s,t)\right)^2 \, ds - \int_0^L \mathbf{X}(s,t) \cdot \mathbf{w}(s,t) \, ds, \tag{46}$$

Then the extended Lagrangian of the clamped rod is

$$\begin{aligned} \mathcal{L}(t) = \mathcal{T}(t) - \mathcal{V}(t) - \int_0^L N(s,t) \, \left[\left(\mathbf{X}'(s,t)\right)^2 - 1 \right] ds \\ - \mathbf{R}(t) \cdot [\mathbf{X}(0,t) - \mathbf{O}] - M(t) \, \left[\mathbf{n}(t) \cdot \mathbf{X}'(0,t)\right], \end{aligned} \tag{47}$$

where $N(s,t)$ is the Lagrange multiplier associated with the inextensibility condition (modelling the axial component of the internal action), and $\mathbf{R}(t)$, $M(t)$ are the Lagrange multipliers modeling the reaction force and the reaction moment at the clamp.

After applying the Hamiltonian Principle,

$$\int_{t_0}^{t^*} \delta\mathcal{L}(t) \, dt = 0, \tag{48}$$

the governing equations can be written in weak form as

$$\begin{aligned}
&\int_{t_0}^{t^*}\int_0^L \gamma\,\delta\mathbf{X}(s,t)\cdot\ddot{\mathbf{X}}(s,t)\;\mathrm{d}s\;\mathrm{d}t \\
&\qquad + \int_{t_0}^{t^*}\int_0^L B\,\delta\mathbf{X}''(s,t)\cdot\mathbf{X}''(s,t)\;\mathrm{d}s\;\mathrm{d}t \\
&- \int_{t_0}^{t^*}\int_0^L \delta\mathbf{X}(s,t)\cdot\mathbf{w}(s,t)\;\mathrm{d}s\;\mathrm{d}t + \int_{t_0}^{t^*}\delta\mathbf{X}(0,t)\cdot\mathbf{R}(t)\;\mathrm{d}t \\
&\qquad + \int_{t_0}^{t^*}(\delta\mathbf{X}'(0,t))\cdot\mathbf{n}(t)\,M(t)\;\mathrm{d}t \\
&\quad + \int_{t_0}^{t^*}\int_0^L 2\,\delta\mathbf{X}'(s,t)\cdot\mathbf{X}'(s,t)\,N(s,t)\;\mathrm{d}s\;\mathrm{d}t = 0,
\end{aligned} \tag{49}$$

$$\int_{t_0}^{t^*}\delta\mathbf{R}(t)\cdot[\mathbf{X}(0,t)-\mathbf{O}]\,\mathrm{d}t = 0,$$

$$\int_{t_0}^{t^*}\delta M(t)\;\left[\mathbf{n}(t)\cdot\mathbf{X}'(0,t)\right]\mathrm{d}t = 0,$$

$$\int_{t_0}^{t^*}\int_0^L \delta N(s,t)\;\left[(\mathbf{X}'(s,t))^2-1\right]\mathrm{d}s\,\mathrm{d}t = 0,$$

for all $\delta\mathbf{X}\in H^2((0,L);\mathbb{R}^d)$, $\delta\mathbf{R}(t)\in\mathbb{R}^d$, where d denotes the number of spatial dimensions considered in the simulation, $\delta M(t)\in\mathbb{R}$ and $\delta N\in H^1((0,L);\mathbb{R})$. In the present work, the inextensible curve is considered in 2D space, due to the nature of the configuration under examination.

STRONG FORM Eq. 49 can be written in strong form as

$$\begin{aligned}
&\gamma\,(\ddot{\mathbf{X}}(s,t)-\mathbf{g}) + B\mathbf{X}^{(4)}(s,t) - 2(\mathbf{X}'(s,t)\,N)' = 0\,, \\
&\qquad\qquad \forall\, s\in(0,L),\; t\in(t_0,t^*).
\end{aligned} \tag{50}$$

The strong form is complemented by the constraints

$$\begin{aligned}
&\mathbf{X}(0,t) = \mathbf{O}\,,\ \forall\, t \in (t_0, t^*),\\
&\mathbf{n}(t)\cdot\mathbf{X}'(0,t) = 0\,,\ \forall\, t \in (t_0, t^*),\\
&\|\mathbf{X}'(s,t)\| - 1 = 0\,,\ \forall\, s \in (0,L),\ t \in (t_0, t^*),
\end{aligned} \tag{51}$$

and the following boundary conditions

$$\begin{aligned}
&B\,\mathbf{X}''(L,t) = \mathbf{O},\\
&\mathbf{X}'(0,t)N(0,t) = \mathbf{R}(t) + B\,\mathbf{X}'''(0,t),\\
&B\,\mathbf{X}'''(L,t) = m(\ddot{\mathbf{X}}(L,t) - \mathbf{g}) + \mathbf{X}'(L,t)\,N(L,t).
\end{aligned} \tag{52}$$

2.6 NUMERICAL METHODS

In this section the numerical methods and computational tools used to obtain some of the results presented in the next chapters are discussed.

2.6.1 *Numerical integration of the derived ODEs*

The numerical solution of ODEs can be obtained in two ways. The straightforward way is to approximate the derivatives of the ODE by some finite difference rule, exploiting the limit definition of the derivative. The second way to obtain a numerical solution is the integration over a timespan of the ODE and, using a reconstruction of the solution (e.g. a piece-wise linear continuous function), obtain a time-stepping rule. Both methods give rules to obtain the solution on time t^{n+1} given the timehistory up to the time t^n.

The ODEs considered here are of the form

$$\dot{u} = f(t,u), \tag{53}$$

ODEs of higher order can be solved as a system of ODEs of first order by using the order reduction technique.

2.6.1.1 *Solution of ODEs using finite differences*

The idea is to approximate the time derivatives as a finite difference. The choice of the finite difference rule is going to yield different numerical schemes. The schemes used in the present work make use of a first order approximation of the time derivatives if the form

$$\dot{u}(t) = \frac{u(t) - u(t-h)}{h}, \tag{54}$$

where h is the timestep size and the main difference lies on the choice of the point in time that the function f is evaluated.

IMPLICIT EULER SCHEME The evaluation of the function f is on the time of the new solution t^{n+1}, giving the following rule

$$u(t^{n+1}) = u(t^n) + hf(t^{n+1}, u(t^{n+1})). \tag{55}$$

CRANK-NICOLSON SCHEME The evaluation of the function f is on the middle of the timestep from t^n to t^{n+1}, assuming that the solution is linear in that timespan. Then the value of the function f can be calculated as

$$f(t^{n+1/2}, u(t^{n+1/2})) = \frac{1}{2}\left[f(t^n, u(t^n)) + f(t^{n+1}, u(t^{n+1}))\right], \tag{56}$$

and the rule becomes

$$u(t^{n+1}) = u(t^n) + \frac{1}{2}h\left[f(t^n, u(t^n)) + f(t^{n+1}, u(t^{n+1}))\right]. \tag{57}$$

This method is called semi-implicit due to the appearance of both known and unknown quantities in the right hand side.

NEWMARK METHOD A widely used method for time integration of second order ODEs in the form

$$m\,\ddot{u}(t) + f(u(t), \dot{u}(t)) = q(t), \tag{58}$$

is that of the Newmark method. Assuming a solution at the timestep n, compatible with the constraints, the solution at the timestep $n+1$ can be obtained by the following formulae

$$\begin{aligned}
\dot{u}^{n+1} &= \dot{u}^n + (1-\beta_1)h\,\ddot{u}^n + \beta_1 h\,\ddot{u}^{n+1},\\
u^{n+1} &= u^n + h\,\dot{u}^n + \frac{h^2}{2}\left[(1-2\beta_2)\,\ddot{u}^n + 2\beta_2\,\ddot{u}^{n+1}\right],\\
m\,\ddot{u}^{n+1} &+ f(u^{n+1}, \dot{u}^{n+1}) = q^{n+1},
\end{aligned} \tag{59}$$

where β_1 and β_2 are the two parameters of the time-marching scheme. The choice $\beta_1 = 0.5$ and $\beta_2 = 0.25$ would result in a scheme with zero numerically-induced dissipation.

2.6.1.2 *Solution of ODEs by integrating over the timestep*

By integrating the ODE in the interval $[t^n, t^{n+1}]$ and integrating by parts the left hand side we get

$$u(t^{n+1}) - u(t^n) = \int_{t^n}^{t^{n+1}} f(t, u)\, dt. \tag{60}$$

Then different rules can be obtained through an appropriate reconstruction of the function $u(t)$ in that time interval. The schemes obtained in section 2.6.1.1 can be obtained also using this method. The Implicit-Euler rule can be found by approximating the integral as

$$\int_{t^n}^{t^{n+1}} f(t, u)\, dt = h\, f(t^{n+1}, u(t^{n+1})), \tag{61}$$

and the Crank-Nicolson scheme by approximating the integral with the trapezoid rule as

$$\int_{t^n}^{t^{n+1}} f(t, u)\, dt = \frac{1}{2} h \left[f(t^n, u(t^n)) + f(t^{n+1}, u(t^{n+1})) \right]. \tag{62}$$

The integration approach can be more versatile, as it gives more choices for obtaining solutions that respect desired continuity properties. Further, advantages of this approach become apparent in the case of Differential-Algebraic Systems of Equations (DAEs) or Equations that cannot be written in the standard form (53).

2.6.2 *Finite element formulation of the inextensible elastica*

The Hamiltonian principle defines a functional operator over space and time. In order to solve the integral equations that have been derived from the minimization of this functional, the space and time integrals are treated separately. First, for every given time t the unknown fields are reconstructed from discrete data with the aid of known basis functions of the function space the fields belong to. The discrete data associated with the space reconstruction are only functions of time. Then, the integration in time can be performed by a usual time marching scheme. It should be noted that due to the complex constraints explicit time marching schemes are not expected to work.

The spatial integration domain $\Omega = [0, L]$ is split in N_{el} non-overlapping subdomains $\Omega_i = [s_i, s_{i+1}]$. Then the integrals in space can be calculated as the sum of the integrals over the subdomains Ω_i,

$$\int_0^L f(s)\,ds = \sum_{i=1}^{N_{el}} \int_{\Omega_i} f(s)\,ds. \tag{63}$$

On every subdomain Ω_i the curve $\mathbf{X}(s,t)$ is approximated with cubic Hermite polynomials, while the Lagrange multiplier distribution $N(s,t)$ is approximated with a linear function. The unknown fields are reconstructed in Ω_i as

$$\mathbf{X}(\xi,t) = \mathbf{H}_i(\xi)\cdot\hat{\mathbf{X}}_i(t), \quad N(\xi,t) = \mathbf{P}_i(\xi)\cdot\hat{\mathbf{N}}_i(t), \tag{64}$$

where $\xi = \frac{s-s_i}{s_{i+1}-s_i} \in [0,1]$, $\hat{\mathbf{X}}_i(t)$ and $\hat{\mathbf{N}}_i(t)$ are the space-discrete data that define the approximate fields $\mathbf{X}(\xi,t)$ and $N(\xi,t)$ respectively and

$$\mathbf{H}_i(\xi) = \begin{bmatrix}\phi_1(\xi)\,\mathbf{I}, & h_i\,\phi_2(\xi)\,\mathbf{I}, & \phi_3(\xi)\,\mathbf{I}, & h_i\,\phi_4(\xi)\,\mathbf{I}\end{bmatrix}, \tag{65}$$

$$\mathbf{P}_i(\xi) = \begin{bmatrix}\ell_1(\xi) & \ell_2(\xi)\end{bmatrix}, \tag{66}$$

where $h_i = s_{i+1} - s_i$ denotes the length of the line segment in the parameter space, $\{\phi_k(\xi)\}$ are the Hermite cubic spline basis, $\{\ell_k(xi)\}$ are the nodal basis of the space of linear functions, and $\mathbf{I}$ is a 2-by-2 or 3-by-3 identity matrix depending on the number of spatial dimensions considered.

Assuming the same spatial reconstruction of the fields $\mathbf{X}_{var}(s,t)$ and $N_{var}(s,t)$, Eq. (49) can be written as

$$\int_{t_0}^{t^*} \mathbf{A}\,\ddot{\mathbf{U}}\,dt + \int_{t_0}^{t^*} \mathbf{B}\,\mathbf{U}\,dt = \int_{t_0}^{t^*} \mathbf{Q}\,dt, \tag{67}$$

where

$$\mathbf{A} = \begin{bmatrix}\mathbf{M} & \mathbf{0} & \mathbf{0}\\ \mathbf{0} & \mathbf{0} & \mathbf{0}\\ \mathbf{0} & \mathbf{0} & \mathbf{0}\end{bmatrix}, \quad \mathbf{B}(\hat{\mathbf{X}}) = \begin{bmatrix}\mathbf{K} & \mathbf{S}_{cl} & \mathbf{S}_N(\hat{\mathbf{X}})\\ \mathbf{S}_{cl}^T & \mathbf{0} & \mathbf{0}\\ \frac{1}{2}\mathbf{S}_N^T(\hat{\mathbf{X}}) & \mathbf{0} & \mathbf{0}\end{bmatrix},$$

$$\mathbf{U}(t) = \begin{pmatrix}\hat{\mathbf{X}}(t)\\ \mathbf{R}(t)\\ M(t)\\ \hat{\mathbf{N}}(t)\end{pmatrix}, \quad \mathbf{Q} = \begin{pmatrix}\mathbf{G}\\ \mathbf{0}\\ 0\\ \mathbf{1}\end{pmatrix}, \tag{68}$$

$\mathbf{M}$ is the mass matrix, $\mathbf{K}$ is the stiffness matrix, $\mathbf{S}_{cl}$ is the matrix encoding the clamp constraints and $\mathbf{S}_N(\hat{\mathbf{X}})$ the matrix encoding the inextensibility constraint. It should be noted that in the nonlinear case considered here $\mathbf{S}_N(\hat{\mathbf{X}})$ depends on the solution $\hat{\mathbf{X}}$ and therefore an iterative nonlinear solver is needed to solve the resulting equations. It should be noted, that in contrast to linear finite element formulations the Matrix $\mathbf{B}$ is not symmetric ($\mathbf{B} \neq \mathbf{B}^T$).

The system of equations (67) is a Differential-Algebraic system of Equations (DAE). As such, the matrix $\mathbf{A}$ is singular and non invertible as a whole and the standard procedures for ODEs cannot be applied directly.

One way to integrate the system in time is to use the Newmark method, however in Chapter 4 an implicit Euler scheme is adopted in order to avoid some stability issues with the specific constraints. In order to apply the Implicit Euler scheme, the order of the ODEs is reduced from 2 to 1, by the following relation

$$\begin{aligned} \hat{\mathbf{X}}(t) &= \hat{\mathbf{X}}_1(t), \\ \dot{\hat{\mathbf{X}}}_1(t) &= \hat{\mathbf{X}}_2(t). \end{aligned} \tag{69}$$

A convergence analysis and a comparison between different solution strategies of the discretized model is provided in Appendix C.

3 INSTABILITIES OF EXTENSIBLE ROD

3.1 INTRODUCTION

An innovative structural system, based on tensile and compressive buckling of an elastic rod, is proposed in the present chapter. More specifically, an axially and flexurally deformable rod is considered with one clamped end constrained to move along a straight direction and the other along a curved profile with a possible discontinuous curvature. The soft rod remains straight until the axial force is sufficiently small, but it buckles (under either compression or tension) and enters in a strongly nonlinear post-critical behaviour, when the load surpasses a critical limit, thus forcing rod deflection. Therefore, in contrast with an inextensible rod, the soft rod deforms axially before buckling, thus allowing to display an initial linear force-displacement response. The considered structural system is analytically solved in its nonlinear range and an optimization algorithm is developed, allowing the design of a desired force-displacement response. As an example of the obtained results, Fig. 5 reports the response of a force-limiting device designed by us and showing an excellent performance. In a more general context, the force-displacement response of the proposed structure depends only on the constraint's profile shape and on the (axial vs bending) stiffness ratio, so that negative stiffness, or sinusoidal, or triangular, or many other 'exotic' responses can be designed (examples are presented in Section 3.5).

The analysis of the proposed structure leads to another important feature, never observed before: the *d*ouble restabilization in compression. Indeed, due to the axial compliance of the rod, it is expected that the straight configuration recovers stability after buckling, similarly to the behaviour of the 'penetrating blade' [9], and therefore displays a restabilization in compression. However, within a specific set of stiffness ratios and profile curvatures at the origin, the proposed structure displays a *d*ouble restabilization of the trivial (straight) configuration, where four exchanges of stability are observed. This unexpected feature is analysed in detail in Section 3.3, but a concise explanation is anticipated in Section 3.1.1.

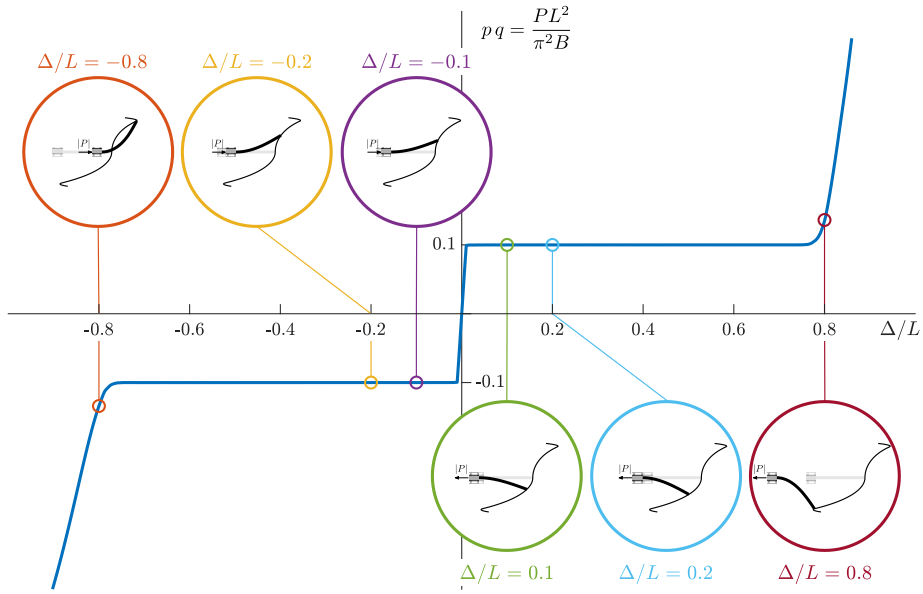

Figure 5: Dimensionless force $PL^2/(\pi^2 B)$ vs. dimensionless displacement Δ/L for an elastic rod (flexurally and axially deformable and subject to a curved constraint), with a stiffness ratio $q = KL^2/(\pi^2 B) = 10$, optimized to realize a force limiter device with $|P_{cr}|L^2/(\pi^2 B) = 0.1$ and locking near the end of the stroke (from $\Delta/L = \pm 0.73$). Deformed configurations of the elastic rod are displayed for $\Delta/L = \pm\{0.1, 0.2, 0.8\}$, along with the optimized shape of the constraint's profile, found to have a discontinuous curvature at the origin ($f''(0^-) = -4.186$ and $f''(0^+) = 1.897$). The definition of the displacement Δ is shown in Fig. 7.

The present theoretical analysis initiates with the derivation of the nonlinear equilibrium equations for the extensible elastica (Sect. 3.2). Linearization of these equations governs the determination of bifurcation (Sect. 3.3.1), which is complemented by a stability analysis of the trivial configuration (by means of a dynamic approach, Sect. 3.3.2). The post-critical response is evaluated analytically by adapting an available closed-form solution [6] to the present boundary conditions (Sect. 3.4). Finally, an optimization algorithm is developed to find the profile shape displaying a prescribed force-displacement curve (Sect. 3.5). The solution of this problem is shown to change with varying the (axial vs bending) stiffness ratio, so that many systems can provide the same structural response. Finally, it is shown that a broad range of post-critical behaviours can be achieved (including bilinear, sinusoidal, triangular) and that more axially compliant rods facilitate the optimization.

The results presented in this chapter can be used in the design of *passive* mechanical devices (i.e. not needing external control), delivering a designed force-displacement response and possibly encompassing multistable behaviour, with applications in the field of force-limiters and soft mechanisms. Movies of the present structure optimized to provide specific force-displacement diagrams are available as electronic supporting material.

3.1.1 *A premise on (single and double) restabilization*

Using linearization, a simple explanation is provided below for the destabilization and subsequent restabilization of the straight configuration of an axially and flexurally deformable elastic rod, with a movable clamp at its left end and a pin at the right one, subject to an axial load P that is assumed positive when tensile.

The linearized axial and flexural equilibrium equations are

$$K\varepsilon(S) - P = 0, \quad B\,\theta''(S) - \left(1 + \frac{P}{K}\right) P\,\theta(S) = F, \tag{70}$$

where K and B are the axial and bending stiffness respectively, $\varepsilon(S)$ the local axial strain, $\theta(S)$ the rotation of the rod's tangent with respect to the undeformed straight configuration, F is the (unknown) reaction at the pin (orthogonal to P), and the prime denotes the derivative with respect to the undeformed curvilinear rod's coordinate S.[1]

The boundary conditions $\theta(0) = 0$, $\theta'(L) = 0$, and $\int_0^L \theta(S)\,dS = 0$ lead to the following expression for the bifurcation loads

$$\pi\,\sqrt{-(1+p)\,p\,q}\,\cot\!\left(\pi\,\sqrt{-(1+p)\,p\,q}\right) = 1, \tag{71}$$

where p is the non-dimensional load and q is the (axial vs bending) stiffness ratio, defined as

$$p = \frac{P}{K}, \quad q = \frac{KL^2}{\pi^2 B}. \tag{72}$$

When the rod is made up of a homogeneous material (and with uniform cross-section), the stiffness ratio reduces to $q = \lambda^2/\pi^2 \gtrsim 10^3$, where

1 For simplicity the present analysis is developed under the assumption of linear axial behaviour. Although highly elastic materials such as rubber often display a nonlinear force/displacement behaviour, the linearity assumption introduced here strongly simplifies the treatment and is however adequate when the strain is not large or when the rod is realized via springs as the systems reported in Appendix A.

λ is the rod's slenderness. However, values of q below that range can be considered to model, via the extensible elastica, the mechanical response of architected one-dimensional structural elements. Although the identification of such structural elements falls outside the scope of the present research, a rough example is provided by a rectangular wire (die) helical spring, with a high cross section aspect-ratio. Moreover, by neglecting configurational forces [3, 10] (which do not influence bifurcation [9, 13]), another example is given by a round wire helical spring containing a coaxial flexible piston or a spring having one end sliding along a rod with uniform cross section.[2]

The bifurcation loads p for an extensible rod, subject to the above-mentioned boundary conditions, are reported in Fig. 6 (left part) for a range of values of the stiffness ratio q. This result shows that bifurcation does not occur for $q < 8.183$, while two bifurcation loads (characterized by the same instability mode) exist under compression for $q > 8.183$. In the latter case, the two bifurcation loads have different mechanical interpretations: the one with smallest (greatest) absolute value is referred to as $p_{de}^{(-)}$ $\left(p_{re}^{(-)}\right)$, because it is associated to destabilization (restabilization) of the trivial configuration at increasing compression. The structural system therefore displays a (single) restabilization.

Anticipating some of the results discussed in detail in section 3.3, the presence of a curved profile introduces a tensile instability [10, 11, 66] at the load value $p_{cr}^{(+)}$ and a double restabilization of the trivial configuration for $q \in (q_a, q_b)$, depending on the profile curvature. These features are shown on the right part of Fig. 6 for a profile with radius of curvature equal to $1/15$ of the undeformed rod's length, for which the stiffness ratio range for double restabilization is defined by $q_a = 12.457$ and $q_b = 19.191$. The two bound values q_a and q_b will be shown to be approximately linearly increasing with the modulus of the dimensionless (negative) profile curvature at the origin, $f''(0)$.

It is finally observed that the occurrence of the double restabilization requires a significant shortening of the structure, with the second (and final) restabilization displayed at a compressive deformation of more than 90% of the undeformed length. A spring, modelled as an extensional elastica, can be 'practically' used in order to achieve such a high compression experimentally. For example, 10 active coils with closed and ground ends

2 The evaluation of the shear and axial stiffness of these structural examples is deferred to Appendix A.

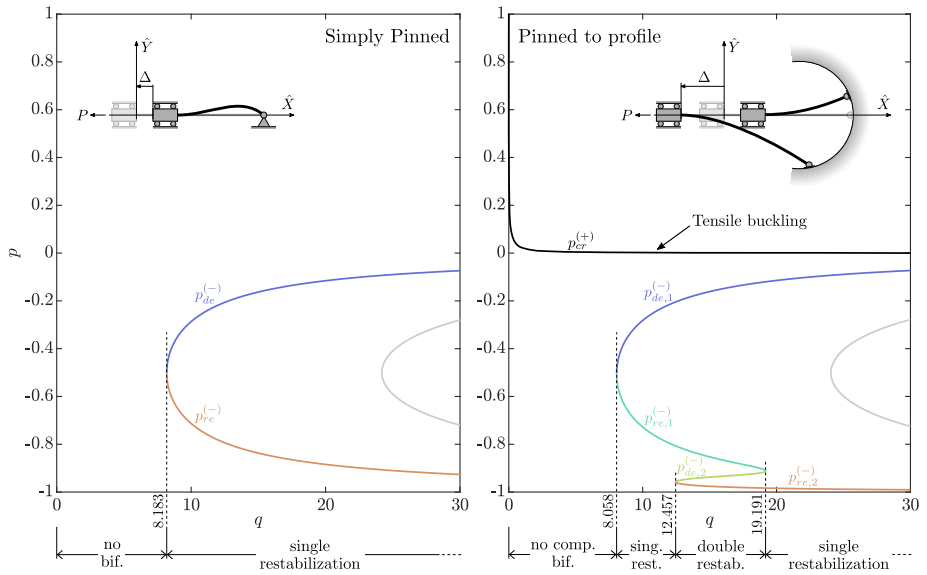

Figure 6: Bifurcation load p for an axially and flexurally deformable rod attached to a sliding clamp on its left end and pinned on the right end at a fixed point (left) or at a point constrained to move on a smooth curved profile (right, with a radius of curvature equal to $1/15$ of the undeformed rod's length, $f''(0) = -15$). The bifurcation loads are reported at varying axial/bending stiffness ratio q. The tensile buckling load $p_{cr}^{(+)}$ is reported as black line, the compressive bifurcation loads of destabilization $p_{de}^{(-)}$ and restabilization $p_{re}^{(-)}$ associated to the first mode as coloured lines, while those of higher modes as gray lines. Ranges of stiffness ratio q for which single and double restabilization occurs are highlighted.

of an helicoidal spring (with a wire diameter of 0.4 mm, and coil pitch of 10 mm) can achieve a shortening of more than 95% when compressed.

3.2 THE EXTENSIBLE ELASTICA WITH AN END CONSTRAINED TO MOVE ALONG A FRICTIONLESS PROFILE

A soft rod is considered, connected to a sliding clamp on its left end, while the right end is constrained to move along a frictionless curved profile, Fig. 7. The rod has a straight undeformed configuration of length L and is characterized by both axial, K, and flexural, B, stiffnesses. Therefore, it is assumed to obey the Reissner rod model [6, 46] in which the shear stiffness is set to be infinite and the deformed configuration is described by the axial strain $\varepsilon(S)$ and the rotation $\theta(S)$ fields along the curvilinear un-

deformed coordinate $S \in [0, L]$. The spatial coordinate s on the deformed curve is related to the material coordinate S through

$$s(S) = \int_0^S [1 + \varepsilon(\sigma)]\, d\sigma, \quad S \in [0, L], \tag{73}$$

so that the length ℓ of the deformed rod is

$$\ell = s(L) = \int_0^L [1 + \varepsilon(\sigma)]\, d\sigma, \tag{74}$$

which differs from L because of the presence of the axial strain $\varepsilon(S)$. By introducing a moving Cartesian reference system X–Y, having its origin coincident with the moving clamp in the deformed configuration and with the X–axis aligned with the straight undeformed configuration, the coordinates of the section at a point S are given by

$$\begin{aligned} X(S;\varepsilon,\theta) &= \int_0^S [1 + \varepsilon(\sigma)] \cos\theta(\sigma)\, d\sigma, \\ Y(S;\varepsilon,\theta) &= \int_0^S [1 + \varepsilon(\sigma)] \sin\theta(\sigma)\, d\sigma. \end{aligned} \tag{75}$$

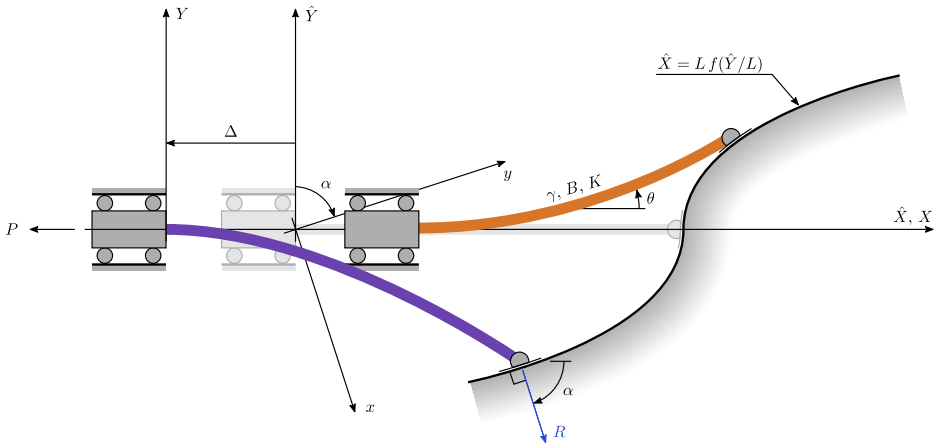

Figure 7: Scheme of the proposed structure, where an axially and flexurally deformable elastic rod is mounted on a moving clamp on its left end and slides with a pin on a curved profile on its right end. The profile is a perfectly frictionless constraint, defined by the curve $\widehat{X} = Lf(\widehat{Y}/L)$. The elastic rod is in a trivial equilibrium straight configuration and may buckle in tension and compression when a load P is applied.

The clamp can move only along the X–axis and its displacement from the undeformed state is measured by the distance Δ. Introducing a fixed

Cartesian reference system $\widehat{X}-\widehat{Y}$, with origin coincident with the moving clamp in the unloaded condition and parallel to the moving $X-Y$ system, the coordinates of the rod's axis can be written as

$$\widehat{X}(S) = X(S;\varepsilon,\theta) - \Delta, \qquad \widehat{Y}(S) = Y(S;\varepsilon,\theta). \tag{76}$$

In this reference system, the curved profile is described by

$$\widehat{X}\left(\widehat{Y}\right) = Lf\left(\frac{\widehat{Y}}{L}\right), \tag{77}$$

under the constraint $f(0) = 1$. Moreover, the displacement Δ (positive when opposite to the $\widehat{X}$-axis) is given by

$$\Delta = d_X(\varepsilon,\theta) - Lf\left(\frac{d_Y(\varepsilon,\theta)}{L}\right), \tag{78}$$

where d_X is the length of the elastica projection on the X–axis and d_Y is the vertical displacement of the pin on the right end of the rod

$$\begin{aligned} d_X(\varepsilon,\theta) &= \int_0^L [1+\varepsilon(\sigma)]\cos\theta(\sigma)\,d\sigma, \\ d_Y(\varepsilon,\theta) &= \int_0^L [1+\varepsilon(\sigma)]\sin\theta(\sigma)\,d\sigma. \end{aligned} \tag{79}$$

The moving clamp is subject to the dead load P, positive when opposite to the X axis (namely, tensile state for the section at $S = 0$), and therefore the mechanical system is conservative. The potential energy $\mathcal{V}$ of the structure is the sum of the axial and flexural elastic energies and the potential energy of the dead load,

$$\mathcal{V}(\varepsilon,\theta) = \frac{K}{2}\int_0^L [\varepsilon(\sigma)]^2\,d\sigma + \frac{B}{2}\int_0^L \left[\theta'(\sigma)\right]^2 d\sigma - P\,\Delta, \tag{80}$$

where a prime stands for differentiation with respect to the relevant (spatial) argument. The first variation $\delta\mathcal{V}$ of the potential energy for perturbations in the strain $\delta\varepsilon$ and rotation $\delta\theta$ is given by

$$\delta\mathcal{V} = \int_0^L K\,\varepsilon(\sigma)\,\delta\varepsilon(\sigma)\;d\sigma - \int_0^L B\,\theta''(\sigma)\,\delta\theta(\sigma)\;d\sigma - P\,\delta\Delta, \tag{81}$$

where

$$\delta\Delta = \delta d_X - f'\left(\frac{d_Y}{L}\right)\;\delta d_Y, \tag{82}$$

$$\delta d_Y = \int_0^L [1+\varepsilon(\sigma)]\,\cos\theta(\sigma)\,\delta\theta(\sigma)\,d\sigma + \int_0^L \sin\theta(\sigma)\,\delta\varepsilon(\sigma)\,d\sigma, \tag{83}$$

and

$$\delta d_X = -\int_0^L [1+\varepsilon(\sigma)]\,\sin\theta(\sigma)\,\delta\theta(\sigma)\,d\sigma + \int_0^L \cos\theta(\sigma)\,\delta\varepsilon(\sigma)\,d\sigma. \tag{84}$$

The vanishing of the first variation $\delta\mathcal{V}$ for compatible perturbations $\delta\varepsilon$ and $\delta\theta$ provides the following coupled system of nonlinear equilibrium equations

$$\begin{aligned} &B\theta''(S) - P\,[1+\varepsilon(S)]\left[f'\left(\frac{d_Y}{L}\right)\cos\theta(S) + \sin\theta(S)\right] = 0,\\ &K\varepsilon(S) + P\left[f'\left(\frac{d_Y}{L}\right)\sin\theta(S) - \cos\theta(S)\right] = 0, \end{aligned} \tag{85}$$

complemented by the algebraic constraint, Eq. (78), and the boundary conditions

$$Y(0) = 0, \quad \theta(0) = 0, \quad \theta'(L) = 0, \tag{86}$$

respectively prescribing the vanishing of the vertical displacement and of the rotation at the moving clamp, and the vanishing of the moment at the pin.

It should be noted that a reaction force R is realized at the pin on the profile. Due to the frictionless assumption, this force is orthogonal to the profile, and therefore inclined by the angle α with respect to the $\widehat{X}$–axis given by the following condition

$$\alpha = \arctan\left[f'\left(\frac{d_Y}{L}\right)\right]. \tag{87}$$

The trivial straight configuration,

$$\theta(S) = 0, \qquad \varepsilon(S) = \frac{P}{K}, \tag{88}$$

satisfies the equilibrium equations (85) if and only if $f'(0) = 0$. Henceforth, this profile property is assumed and under this circumstance bifurcation may be displayed depending on the dimensionless curvature of the profile at null $\widehat{Y}$ coordinate, $f''(0)$, and rod's properties (B, K, L) through the stiffness ratio q. As shown in [11], the profile shape can also be designed to present a discontinuous curvature at null $\widehat{Y}$ coordinate, $f''(0^+) \neq f''(0^-)$ (as in Fig. 7), to better tune the mechanical response under both signs of Δ (namely, both directions).

3.3 BIFURCATION AND STABILITY OF THE TRIVIAL CONFIGURATION

3.3.1 *Bifurcation loads*

Bifurcation conditions from the trivial straight configuration, Eq. (88), are investigated under small rotation $\theta(S)$ assumption, providing the linearized version of the equilibrium equations (85)

$$\begin{aligned} &B\theta''(S) - P\,[1+\varepsilon(S)]\left[\frac{d_Y}{L}f''(0) + \theta(S)\right] = 0, \\ &K\varepsilon(S) - P = 0, \end{aligned} \tag{89}$$

where the following approximation is considered

$$f'\left(\frac{d_Y}{L}\right) \approx \frac{d_Y}{L} f''(0)\,. \tag{90}$$

Eq. $(89)_2$ is automatically satisfied for the uniform axial strain field $(88)_2$ and Eq. $(79)_2$ can be linearized as

$$d_Y(\varepsilon,\theta) \approx \left(1+\frac{P}{K}\right)\int_0^L \theta(\sigma)\,d\sigma. \tag{91}$$

By considering this latter approximation and the uniform axial strain field $(88)_2$ and by using the dimensionless load p and the (axial vs bending) stiffness ratio q, defined by Eq. (72), the equilibrium equation $(89)_1$ reduces to the following homogeneous and linear integro-differential equation

$$\theta''(S) - p\,q\,(1+p)\,\frac{\pi^2}{L^2}\left(\theta(S) + \frac{f''(0)}{L}\,(1+p)\int_0^L \theta(\sigma)\,d\sigma\right) = 0. \tag{92}$$

The basis for non-trivial solutions of $\theta(S)$ is found to be[3]

$$\theta(S) = \begin{cases} a\cos\left(\sqrt{-(1+p)\,p\,q}\,\dfrac{\pi S}{L}\right) \\ \qquad + b\sin\left(\sqrt{-(1+p)\,p\,q}\,\dfrac{\pi S}{L}\right) + c, \qquad p \in [-1,0], \\ a\cosh\left(\sqrt{(p+1)\,p\,q}\,\dfrac{\pi S}{L}\right) \\ \qquad + b\sinh\left(\sqrt{(p+1)\,p\,q}\,\dfrac{\pi S}{L}\right) + c, \qquad p \in [0,\infty], \end{cases} \tag{93}$$

where a, b, and c are integration constants, where two of these can be computed as functions of the third one (which remains arbitrary, but small, in the present analysis) by imposing the boundary conditions.

Therefore, by substituting solutions (93) into the equilibrium equation (92) and imposing the boundary conditions $(86)_2$ and $(86)_3$, a bifurcation with non-trivial equilibrium configuration exists when[4]

$$\begin{aligned} &f''(0)\sqrt{-(1+p)\,p\,q} \\ &\quad + p\,q\,\pi\,[1+(1+p)\,f''(0)]\cot\left(\pi\sqrt{-(1+p)\,p\,q}\right) = 0, p \in [-1,0], \\ &f''(0)\sqrt{(1+p)\,p\,q} \\ &\quad - p\,q\,\pi\,[1+(1+p)\,f''(0)]\coth\left(\pi\sqrt{(1+p)\,p\,q}\right) = 0, p \in [0,\infty), \end{aligned} \tag{95}$$

defining the bifurcation load p as a function of the stiffness ratio q and dimensionless profile curvature at the origin $f''(0)$. It should be noted that

3 The range $p < -1$ is excluded because it is representative of unnatural bifurcation, involving self-copenetrated rod configurations.

4 In the inextensible limit ($K \to \infty$, $q \to \infty$, $p \to 0$, but $p\,q = PL^2/(\pi^2 B)$ remains finite), the bifurcation loads correspond to the solution of the following equations

$$\begin{aligned} &f''(0)\sqrt{-p\,q} + p\,q\,\pi\,[1+f''(0)]\cot\left(\pi\sqrt{-p\,q}\right) = 0, \quad p < 0, \\ &f''(0)\sqrt{p\,q} - p\,q\,\pi\,[1+f''(0)]\coth\left(\pi\sqrt{p\,q}\right) = 0, \qquad p \geqslant 0. \end{aligned} \tag{94}$$

The latter equations are equivalent to that provided in [11] for the bifurcation loads (their Eq. (17) for $k = 0$). Here, the cases of positive and negative p, corresponding to tension and compression respectively, are separated in order to highlight the differences between the two. The separation also facilitates calculations because developments with imaginary values can be avoided.

the shape of the profile affects the bifurcation loads only because of its dimensionless curvature at the origin, $f''(0)$. These bifurcation conditions are displayed in Fig. 8 as surfaces in the three-dimensional space defined by the parameters p, q and $f''(0)$. Moreover, sections of these surfaces at constant values of $f''(0) = \{-10, -2, -0.5, 0.5, 2, 10\}$ are reported in Fig. 9.

From all of these representations, the following conclusions can be drawn.

- Differently from a standard Sturm-Liouville problem, governing bifurcation for an inextensible rod ($q \to \infty$), the number of bifurcation loads and modes becomes finite due to rod's extensibility. For instance, in Fig. 9 (upper part on the left) for stiffness ratio $q < 1.231$ there is only one mode in tension, while for $q \in (1.231,\ 9.264)$ there is only one mode in tension and only one in compression. Moreover, in Fig. 9 (upper part on the right) there is only one mode in compression for stiffness ratio $q \in (0.822,\ 8.836)$.

- Another effect related to the axial compressibility of the rod is that a bifurcation *m*ode in compression corresponds to more than one bifurcation load. Indeed, except in the limit cases of coalescent loads (discussed below), the bifurcation loads in compression always occur *i*n pairs, so that one corresponds to the *destabilization* (loss of stability) of the straight configuration, while the other to its *restabilization*. For instance, in Fig. 9 (upper part on the left) for $q > 1.231$ there is one bifurcation load for the first mode corresponding to the transition from stability to instability (at increasing compressive load) of the straight configuration. In addition, one restabilization load is found for the first mode, corresponding to the transition from instability to stability. Moreover, it can be observed in the same figure that for higher stiffness ratio q, where a plurality of modes emerge, the compressive bifurcation loads always occur in pairs.

- In tension: none or only one bifurcation load may exist, depending on the sign of the profile curvature at the origin $f''(0)$. The fact that only one critical load is found is related to the presence of the hyperbolic cotangent function in the bifurcation equation $(95)_2$. In particular:
  - for $f''(0) > 0$, tensile bifurcation does not occur, as in the inextensible case;
  - for $f''(0) < 0$, one tensile bifurcation occurs at $p_{cr}^{(+)} > 0$ (where the superscript $(+)$ reminds the reference to tensile load). This

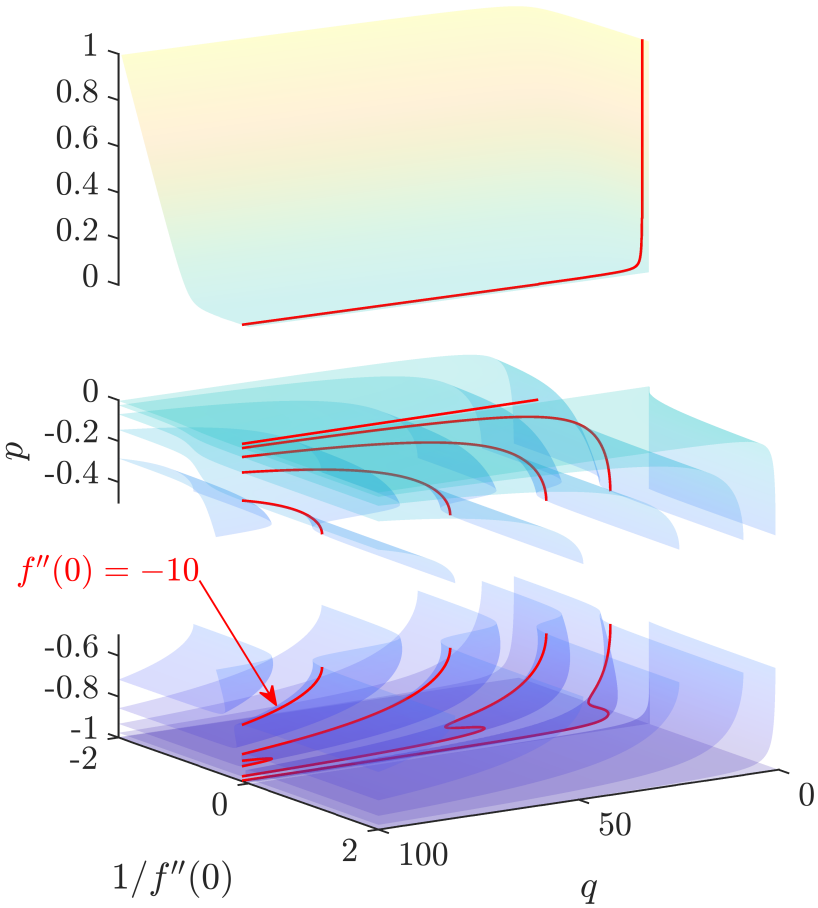

Figure 8: Isosurfaces of Eq. (95) showing the combination of stiffness ratio q, dimensionless radius of profile curvature at the origin $1/f''(0)$ and load p parameters for bifurcation. Note that all red curves belong to the same vertical plane defined by $1/f''(0) = -0.1$ and correspond to Fig. 9 (bottom, left). The representation of the lower surfaces has been slit to improve understanding.

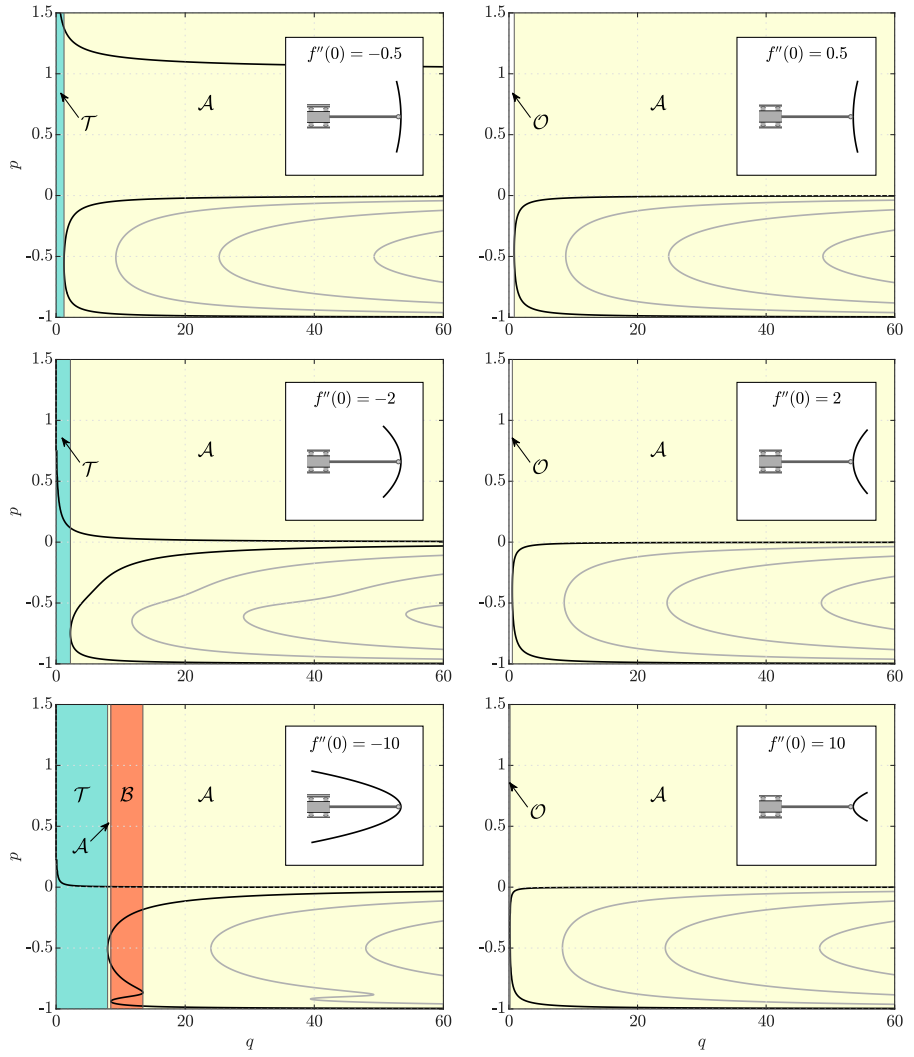

Figure 9: Tensile/compressive bifurcation load p as a function of q, for constant $f''(0) = \{-10, -2, -0.5, 0.5, 2, 10\}$. The regions $\mathcal{O}$, $\mathcal{T}$, $\mathcal{A}$, and $\mathcal{B}$ are also shown. Tensile bifurcation does not occur for $f''(0) > 0$, but always occurs for $f''(0) < 0$. In compression, multiple bifurcation modes can be observed and their number depends on the values of q and $f''(0)$; considering here the first mode, there are regions where there are none ($\mathcal{O}$ and $\mathcal{T}$), two ($\mathcal{A}$), and four (region $\mathcal{B}$) bifurcation compressive loads. The grey curves represent higher modes.

is in contrast with the inextensible case, where tensile bifurcation was existing in a more limited set, $f''(0) < -1$ [11].

- In compression: either bifurcation is excluded, or it may occur with 2 or 4 bifurcation loads associated to the same mode, depending on the values of q and $f''(0)$. More specifically, restricting attention only to the first compression mode, 2 main cases can be distinguished, differing in the number of bifurcations at varying q and $f''(0)$:
  - 2 bifurcation loads occur, associated to the first mode. Each of these corresponds to a destabilization load $\left(p_{de}^{(-)}\right)$ and a restabilization load $\left(p_{re}^{(-)}\right)$ (where the superscript $(-)$ reminds the reference to compressive load),

$$-1 < p_{re}^{(-)} < p_{de}^{(-)} < 0. \tag{96}$$

    An example of this behaviour is visible in Fig. 9 in the upper part on the left for $q > 1.231$;
  - 4 bifurcation loads occur, associated to the first mode, corresponding to two pairs of destabilization/restabilization loads, $\left(p_{de,1}^{(-)}, p_{re,1}^{(-)}\right)$ and $\left(p_{de,2}^{(-)}, p_{re,2}^{(-)}\right)$, occurring in the following order[5]

$$-1 < p_{re,2}^{(-)} < p_{de,2}^{(-)} < p_{re,1}^{(-)} < p_{de,1}^{(-)} < 0. \tag{97}$$

    An example of this behaviour is visible in Fig. 9 in the lower part on the left $q \in (8.488, 13.451)$;

- In compression: multiple bifurcation loads associated to the same mode may occur for modes higher than the first. An example is visible in Fig. 9 in the lower part on the left.

By considering all of the above described cases, four different subsets $\mathcal{O}$, $\mathcal{T}$, $\mathcal{A}$, and $\mathcal{B}$ are distinguished in the $q - f''(0)$ plane (Fig. 10, upper part,

5 In the case when double restabilization may occur for a value of $f''(0)$, the nomenclature of the bifurcation loads $p_{de}^{(-)}$ and $p_{re}^{(-)}$ is enhanced by introducing a subscript 1 or 2 to distinguish between the first and second destabilization/restabilization loads. In order to simplify the presentation, this notation is preserved through a continuation principle for the roots passing from a set of q values where double restabilization is displayed to the set of single restabilization, as illustrated in Fig. 6.

on the left), differing in the number of the main bifurcation conditions as reported in Tab. 1.

Table 1: Numbers of main bifurcations for the subsets $\mathcal{O}$, $\mathcal{T}$, $\mathcal{A}$, and $\mathcal{B}$.

	Tensile bifurcation	Compressive bifurcation
$\mathcal{O}$	0	0
$\mathcal{T}$	1	0
$\mathcal{A}$	1	2 bif. loads associated with 1st mode
$\mathcal{B}$	1	4 bif. loads associated with 1st mode

In the following description of the bifurcation response, the terms '*destabilization*' and '*restabilization*' are introduced to respectively define a bifurcation load in compression representing a transition for the trivial configuration to become unstable or to return to being stable for compressive loads at increasing magnitude.

The $q - f''(0)$ pairs, defining the boundary of each subset, represent the transition in the bifurcation response. More specifically:

- the transition from subset $\mathcal{A}$ to $\mathcal{O}$ or $\mathcal{T}$ corresponds to the transition from the presence of a destabilization $p_{de}^{(-)}$ and restabilization $p_{re}^{(-)}$ load (belonging to the subset $\mathcal{A}$) to a situation where bifurcation is excluded. This occurs at the coalescence
$$p_{de}^{(-)} = p_{re}^{(-)}; \tag{98}$$
- the transition from subset $\mathcal{A}$ to $\mathcal{B}$ correspond to the transition from a pair of bifurcation loads $\left(p_{de}^{(-)}, p_{re}^{(-)}\right)$ to two pairs $\left(p_{de,1}^{(-)}, p_{re,1}^{(-)}\right)$ and $\left(p_{de,2}^{(-)}, p_{re,2}^{(-)}\right)$, all associated to the first bifurcation mode in compression. This necessarily involves one of the following coalescences
$$p_{de,1}^{(-)} = p_{re,1}^{(-)}, \qquad \text{or} \qquad p_{de,2}^{(-)} = p_{re,2}^{(-)}, \qquad \text{or} \qquad p_{de,2}^{(-)} = p_{re,1}^{(-)}. \tag{99}$$

Defining the range of $q \in (q_a, q_b)$ limiting the $\mathcal{B}$ region, the bound values q_a and q_b are approximately linear in the dimensionless profile curvature when this takes large negative values,

$$\left.\begin{aligned} q_a &\approx 0.526 - 0.796 f''(0), \\ q_b &\approx 1.655 - 1.167 f''(0), \end{aligned}\right\} \qquad \text{when } f''(0) < -10. \tag{100}$$

It is anticipated from Section 3.3.2 that, considering also tensile buckling (occurring at $p_{cr}^{(+)} \geqslant 0$), the set $\mathcal{A}$ can be divided into two pairs of subsets, so that when the load p belongs to one pair the trivial configuration is stable, otherwise is unstable

$$\begin{aligned} p \in \left(-1, p_{re}^{(-)}\right) \cup \left(p_{de}^{(-)}, p_{cr}^{(+)}\right) \quad &\Rightarrow \quad \textit{stable} \text{ trivial conf.}, \\ p \in \left(p_{re}^{(-)}, p_{de}^{(-)}\right) \cup \left(p_{cr}^{(+)}, \infty\right) \quad &\Rightarrow \quad \textit{unstable} \text{ trivial conf.}, \end{aligned} \tag{101}$$

while the set $\mathcal{B}$ can be divided into two triplets of subsets

$$\begin{aligned} p \in \left(-1, p_{re,2}^{(-)}\right) \cup \left(p_{de,2}^{(-)}, p_{re,1}^{(-)}\right) \cup \left(p_{de,1}^{(-)}, p_{cr}^{(+)}\right) \quad &\Rightarrow \quad \textit{stable}, \\ p \in \left(p_{re,2}^{(-)}, p_{de,2}^{(-)}\right) \cup \left(p_{re,1}^{(-)}, p_{de,1}^{(-)}\right) \cup \left(p_{cr}^{(+)}, \infty\right) \quad &\Rightarrow \quad \textit{unstable} \end{aligned} \tag{102}$$

The conditions of coalescence correspond to triplets of values for the parameters p, q, and $f''(0)$ and can be visualized as a curve in a three-dimensional parameter space. To investigate coalescence in a two-dimensional representation, Fig. 10 is introduced. In the upper part (on the left) of this figure, all transitions between the different sets $\mathcal{O}$, $\mathcal{T}$, $\mathcal{A}$, and $\mathcal{B}$ are reported in the $q - f''(0)$ plane as curves drawn with different colours. The bifurcation load at which coalescence occurs is indicated with p^* and is reported in Fig. 10 at varying q (lower part, on the left) and at varying $f''(0)$ (upper part, on the right). Note that in the former case $f''(0)$ (in the latter case q) does not assume a fixed value, but varies.

A detail of the bifurcation p-q curves at fixed $f''(0) = \{-6, -15\}$ is reported in the lower part (on the right) of Fig. 10. Here, occurrences of coalescence $p = p^*$ are marked with diamonds of the same colour as the corresponding transition curve.

A comparison is presented in Fig. 11 between bifurcations calculated with two models of elastic rod, namely, an inextensible Euler-Bernoulli rod, and the axially deformable rod investigated in this article, both characterized by the same bending stiffness B and the latter investigated for constant values of $q = \{0.5, 10, 400\}$.

The comparison is reported in terms of a dimensionless value of the axial load P, namely, $pq = PL^2/(\pi^2 B)$, reported as a function of the dimensionless radius of profile curvature at the origin $1/f''(0)$.

Note in the figure that: (i.) tensile and compressive loads are considered; (ii.) some modes higher than the first are included (in light colour); (iii.) the response of the inextensible (extensible) model is reported with a dashed (continuous) line; (iv.) the region $p < -1$, highlighted though a

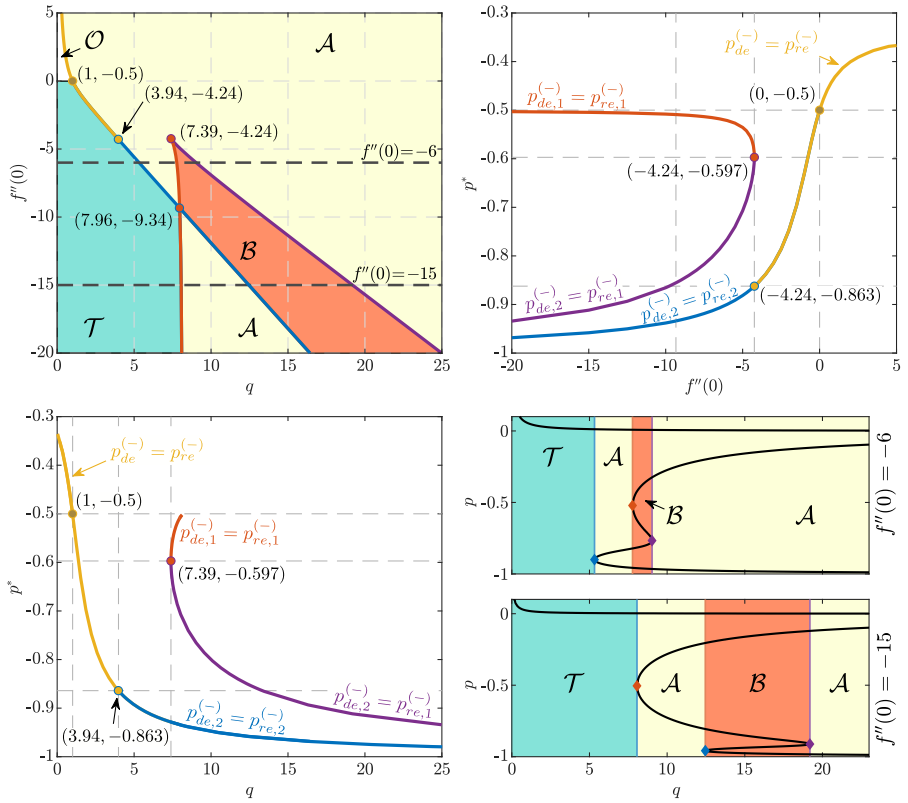

Figure 10: Upper part, left: Sets $\mathcal{O}$, $\mathcal{T}$, $\mathcal{A}$, and $\mathcal{B}$ defined by the number of critical loads in compression (restricted to first mode) and in tension, as described in Table 1. Upper part, right and lower part, left: Coalescent bifurcation load p^* as a function of q (left, lower part) and of $f''(0)$ (right, upper part), defining the different boundaries between two of the sets $\mathcal{O}$, $\mathcal{T}$, $\mathcal{A}$, and $\mathcal{B}$. Lower part, right: Bifurcation load p versus q, evaluated for two values of $f''(0)$; here p^* is marked with a diamond of the same colour as the corresponding transition curve.

gray background, should not be considered as the related compression level has no physical meaning.

From this figure, two main conclusions can be drawn:

- as the stiffness ratio q increases (from left to right in the figure), the bifurcation behaviour of the extensible rod converges to that pertaining to the inextensible one;
- in the figure on the left both models show a transition from a tensile to a compressive bifurcation load (the latter terminates when $p = -1$) and other bifurcation modes are not available. Even in both figures pertaining to $q = 10$ and 400, and for both rod models, a tensile bifurcation load becomes compressive at the point $1/f''(0) = 0$. However, defined as the smaller (in absolute value) load, the critical load evidences a jump at this point, because the continuation of the tensile critical load prevails on a higher-order mode, which is critical for $1/f''(0) < 0$.

For completeness, the regions $\mathcal{O}$, $\mathcal{T}$, $\mathcal{A}$, and $\mathcal{B}$ are also shown in Fig. 11 and these regions suggest the following observations.

- The compressive critical load $p_{de}^{(-)}$ for positive profile curvature $f''(0) = f''_a$ is bounded as follows (Fig. 10)

$$p_{de}^{(-)}\left(f''_a, q\right) \in \left[-\frac{1}{2}, 0\right], \qquad \forall\ f''_a > 0. \tag{103}$$

- With reference to two values f''_a and f''_b of profile curvature at the origin $f''(0)$, the following inequalities hold for the critical loads in tension (Fig. 11)

$$f''_a < 0 \quad \text{and} \quad f''_a < f''_b \quad \Leftrightarrow \quad p_{cr}^{(+)}\left(f''_a, q\right) \leqslant p_{cr}^{(+)}\left(f''_b, q\right), \quad \forall\ q > 0, \tag{104}$$

and in compression

$$f''_a < f''_b \quad \Rightarrow \quad p_{de,1}^{(-)}\left(f''_a, q\right) < p_{de,1}^{(-)}\left(f''_b, q\right), \tag{105}$$

where the definition of critical loads is extended to include cases in which bifurcation does not occur, by assuming $p_{cr}^{(+)}\left(f'', q\right) = +\infty$ for $\{f'', q\} \in \mathcal{O}$ and $p_{de,1}^{(-)}\left(f'', q\right) = -\infty$ for $\{f'', q\} \in \mathcal{O} \cup \mathcal{T}$.

Asymptotic expressions for the bifurcation loads in the limit of vanishing profile curvatures, $f''(0) \to 0^{\pm}$, are reported in Appendix B.

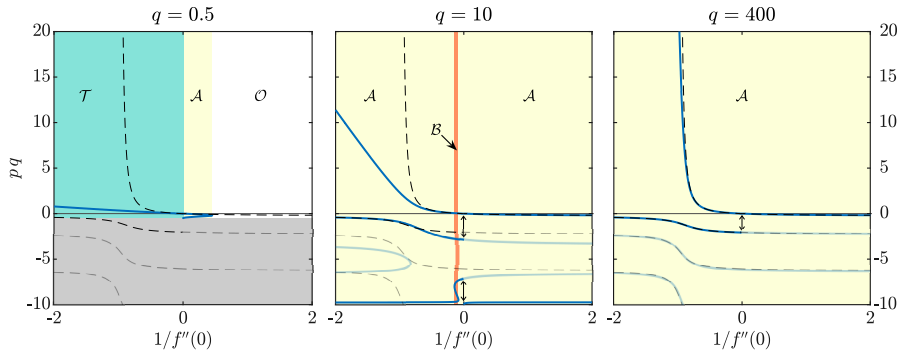

Figure 11: Comparison between tensile/compressive bifurcation loads $pq = PL^2/(\pi^2 B)$ for extensible (dashed lines) and inextensible (continuous lines) rod models and for $q = \{0.5, 10, 400\}$. The region shaded in gray corresponds to $p < -1$, which has no mechanical meaning. Bifurcation loads corresponding to modes higher than the first are drawn with lighter lines. As the stiffness ratio q increases, the bifurcation models converge. At the transition point $1/f''(0) = 0$ tensile instability turns to compressive and the critical load suffers a jump.

PROFILE WITH CURVATURE DISCONTINUITY AT THE ORIGIN. When the profile possesses a curvature discontinuity at the origin, $f''(0^+) \neq f''(0^-)$, each part of the profile defines its 'own' critical loads in tension $p_{cr}^{(+)}(f''(0^\pm), q)$ and in compression $p_{de}^{(-)}(f''(0^\pm), q)$. The tensile (compressive) critical load for the structure corresponds to the smallest (the highest) load,

$$\begin{aligned} p_{cr}^{(+)} &= \min\left[p_{cr}^{(+)}(f''(0^+), q), p_{cr}^{(+)}(f''(0^-), q)\right] > 0, \\ p_{cr}^{(-)} &= \max\left[p_{de,1}^{(-)}(f''(0^+), q), p_{de,1}^{(-)}(f''(0^-), q)\right] < 0. \end{aligned} \tag{106}$$

With the above premise, the design proposed in this article for the profile is based on the following two requirements.

- The first design requirement is a prescription that the shape of the profile that leads to a postcritical behaviour in tension and in compression is of the type illustrated in Fig. 7, so that in tension $p_{cr}^{(+)} = p_{cr}^{(+)}(f''(0^-), q)$ and in compression $p_{cr}^{(-)} = p_{de,1}^{(-)}(f''(0^+), q)$. From a kinematical point of view, this requirement is equivalent to the prescription that bifurcation under compression occurs with $d_Y > 0$ and under tension with $d_Y < 0$. When these conditions prevail, the following inequality holds

$$\Delta(p)\, d_Y(p) \leqslant 0, \tag{107}$$

and the critical loads (106) become only functions of $f''(0)$ and q

$$p_{cr}^{(+)} = p_{cr}^{(+)}\left(f''(0^-),\, q\right), \qquad p_{cr}^{(-)} = p_{cr}^{(-)}\left(f''(0^+),\, q\right). \tag{108}$$

- The second design requirement is that the values of the two critical loads $p_{cr}^{(+)}$ and $p_{cr}^{(-)}$ must be assigned as desired.

It is clear that the inequality (107) imposes a restriction on the possibility to arbitrarily assign the two critical loads. This restriction can be obtained as follows.

After the loads are assigned, it can be proven that a specific value of q exists, say, $\bar{q}$, for which the critical loads are obtained with the same profile curvature at the origin, $f''(0^-) = f''(0^+)$, say, $\bar{f}''$.

For $q \geqslant \bar{q}$ the inequality (107) fails, because

$$\begin{aligned} &q > \bar{q} \implies f''(0^+) > f''(0^-) \quad \text{and} \\ &p_{de,1}^{(-)}\left(f''(0^-)\right) > p_{de,1}^{(-)}\left(f''(0^+)\right) \end{aligned} \tag{109}$$

meaning that the rod buckles in compression ($p < 0$) with $d_Y < 0$, oppositely to what is assumed through the inequality (107). More specifically, for given values of $p_{cr}^{(+)}$ and $p_{cr}^{(-)}$, the pairs $\left\{\bar{f}'', \bar{q}\right\}$ define the range of values of $f''(0^+)$, $f''(0^-)$ and q for which Eq. (107) holds as

$$f''(0^-) \leqslant \bar{f}'' \leqslant 0 \leqslant f''(0^+), \qquad q \leqslant \bar{q}. \tag{110}$$

Introducing the ratio $A = -p_{cr}^{(+)}/p_{cr}^{(-)}$, the parametric curves $\left\{\bar{f}''\left(p_{cr}^{(-)}, A\right), \bar{q}\left(p_{cr}^{(-)}, A\right)\right\}$ are reported in Fig. 12. The points at the intersection between a (dashed) curve pertaining to a value of $p_{cr}^{(-)}$ and a (coloured, solid) curve representative of a value of A lead the values of the pair $\bar{f}''$ and $\bar{q}$ reported on the axes. Note that inside the gray zone in the figure bifurcation is excluded. The boundary of this zone corresponds to the occurrence of coalescent bifurcation loads $p_{cr}^{(-)} = p^*$.

3.3.2 *Stability of the straight configuration from small amplitude vibration analysis*

The stability of the straight configuration can be assessed by analysing the nature of the frequency of the time-harmonic small amplitude vibrations around the straight configuration. In particular, the presence (or absence) of non-real eigenfrequencies defines the instability (or stability) of

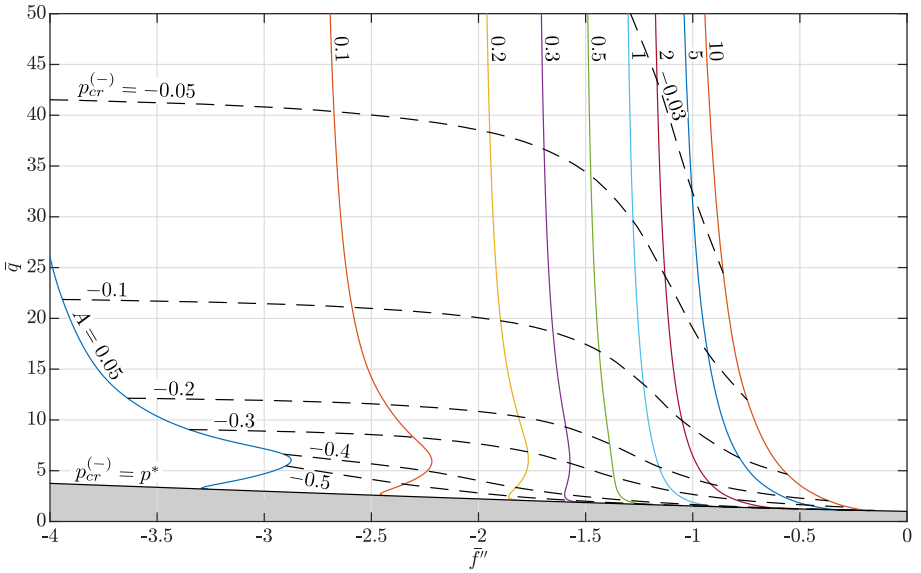

Figure 12: Parametric representation of profile curvature at the origin $\bar{f}''$ and stiffness ratio $\bar{q}$ defining the limit parameters for which the two critical loads can be tuned separately. The intersection between (solid and coloured) curves at different $A = -p_{cr}^{(+)}/p_{cr}^{(-)}$ and (dashed) curves pertaining to $p_{cr}^{(-)}$ defines the corresponding pair $(\bar{f}'', \bar{q})$. In the gray zone compressive bifurcation does not occur and its boundary corresponds to coalescent bifurcation loads $p_{cr}^{(-)} = p^*$.

the straight configuration, and the limit case of vanishing eigenfrequency would confirm the critical loads obtained from the quasi-static analysis performed in Sect. 3.3.1. With the purpose of studying the dynamic response of the system, a linear mass density γ is considered for the rod, so that the Lagrangian $\mathcal{L}$ of the system can be written as

$$\begin{aligned}\mathcal{L} = &\int_0^L \frac{\gamma}{2}\left(\dot{\widehat{X}}^2 + \dot{\widehat{Y}}^2\right) dS - \int_0^L \frac{B}{2}\left(\theta'\right)^2 dS - \int_0^L \frac{K}{2}\varepsilon^2 dS \\ &- \int_0^L N_X\left\{\widehat{X}' - (1+\varepsilon)\cos\theta\right\} dS - \int_0^L N_Y\left\{\widehat{Y}' - (1+\varepsilon)\sin\theta\right\} dS \\ &- P\,\widehat{X}(0) + R_X\left\{\widehat{X}(L) - L\left[f\left(\frac{\widehat{Y}(L)}{L}\right)\right]\right\},\end{aligned} \tag{111}$$

where N_X, N_Y, and R_X are Lagrangian multipliers (the first two representing the X and Y components of the internal force, the last representing the

X component of the reaction R at the pin on the curved profile) and the dot over the functions stands for differentiation with respect to the time variable t. The equations of motion can be derived from the principle of least action as

$$\begin{aligned}
&N_X' = \gamma\,\ddot{\widehat{X}},\\
&N_Y' = \gamma\,\ddot{\widehat{Y}},\\
&B\,\theta'' - (1+\varepsilon)[N_X\,\sin\theta - N_Y\,\cos\theta] = 0,\\
&K\,\varepsilon - N_X\,\cos\theta - N_Y\,\sin\theta = 0,
\end{aligned} \tag{112}$$

along with the boundary conditions

$$N_X(0) = P, \qquad N_X(L) = R_X, \qquad N_Y(L) = R_X\,f'\left(\frac{\widehat{Y}(L)}{L}\right). \tag{113}$$

Considering small time-harmonic vibrations [15] around the trivial equilibrium configuration (88), the relevant fields are assumed through the method of separation of variables as

$$\begin{aligned}
&\widehat{X}(S,t) = S + \frac{P}{K}(S-L) + \bar{X}(S)\,e^{i\,\omega_x t}, && \widehat{Y}(S,t) = \bar{Y}(S)\,e^{i\,\omega_y t},\\
&\varepsilon(S,t) = \frac{P}{K} + \bar{\varepsilon}(S)\,e^{i\,\omega_x t}, && \theta(S,t) = \bar{\theta}(S)\,e^{i\,\omega_y t},\\
&N_X(S,t) = P + \bar{N}_X(S)\,e^{i\,\omega_x t}, && N_Y(S,t) = \bar{N}_Y(S)\,e^{i\,\omega_y t},\\
&R_X(t) = P + \bar{R}_X\,e^{i\,\omega_x t},
\end{aligned} \tag{114}$$

where ω_x and ω_y are the circular frequencies for axial and flexural vibrations, respectively, and functions with an overbar denote functions of the spatial variable only. The amplitudes of the overbar functions are considered to be driven by a small positive parameter η, so that

$$|\bar{X}| \approx |\bar{Y}| \approx |\bar{\varepsilon}| \approx |\bar{\theta}| \approx |\bar{N}_X| \approx |\bar{N}_Y| \approx |\bar{R}_X| \approx \eta, \qquad \eta \gg \eta^2. \tag{115}$$

A substitution of the above expressions into Eqs. (112) and (113), by neglecting higher-order terms in η, yields the following decoupled differential equations in the axial and transverse amplitude oscillations

$$\begin{aligned}
&\bar{X}''(S) + \hat{\omega}_x^2\,\frac{\pi^2}{L^2}\,\bar{X}(S) = 0,\\
&\bar{Y}^{(iv)}(S) - (1+p)\,p\,q\,\frac{\pi^2}{L^2}\,\bar{Y}''(S) - (1+p)^2\,\hat{\omega}_y^2\,\frac{\pi^4}{L^4}\,\bar{Y}(S) = 0,
\end{aligned} \tag{116}$$

where

$$\hat{\omega}_x^2 = \frac{\gamma\,\omega_x^2 L^2}{\pi^2 K}, \quad \hat{\omega}_y^2 = \frac{\gamma\,\omega_y^2 L^4}{\pi^4 B}, \tag{117}$$

to be complemented with the boundary conditions[6]

$$\bar{X}'(0) = 0, \qquad \bar{X}(L) = 0, \tag{120}$$

for axial oscillations, and

$$\begin{aligned} &\bar{Y}(0) = \bar{Y}'(0) = \bar{Y}''(L) = 0, \\ &\bar{Y}'''(L) - (1+p)\,p\,q\,\frac{\pi^2}{L^2}\left[\bar{Y}'(L) + (1+p)\frac{f''(0)}{L}\,\bar{Y}(L)\right] = 0, \end{aligned} \tag{121}$$

for transverse ones. Due to motion decoupling from Eqs. (116), ω_x and ω_y are independent from each other. Taking into account the boundary conditions (120), the integration of Eq. $(116)_1$ provides the axial mode as

$$\bar{X}(S) = \cos\left(\frac{\pi\,\hat{\omega}_x\,S}{L}\right), \tag{122}$$

where

$$\hat{\omega}_x = n - \frac{1}{2}, \qquad n \in \mathbb{N}^+, \tag{123}$$

showing that the axial vibrations have always real circular frequencies ω_x. The transverse mode can be obtained from integration of Eq. $(116)_2$ as

$$\begin{aligned} \bar{Y}(S) = C_1 \cos\left(\frac{\pi\lambda_1 S}{L}\right) + C_2 \cos\left(\frac{\pi\lambda_2 S}{L}\right) \\ + C_3 \sin\left(\frac{\pi\lambda_1 S}{L}\right) + C_4 \sin\left(\frac{\pi\lambda_2 S}{L}\right), \end{aligned} \tag{124}$$

where

$$\lambda_{1,2} = \sqrt{\frac{1+p}{2}}\,\sqrt{-p\,q \pm \sqrt{(p\,q)^2 + 4\hat{\omega}_y^2}}, \tag{125}$$

6 The expansion of Eq. (77) truncated to linear terms in $\widehat{Y}(L)$ is

$$\widehat{X}(L) = Lf(0) + f'(0)\widehat{Y}(L), \tag{118}$$

which, under the considered assumption $f'(0) = 0$, reduces to

$$\widehat{X}(L) = Lf(0), \tag{119}$$

implying the boundary condition $(120)_2$.

and C_1, C_2, C_3, and C_4 are the coefficients defining the transverse shape. The homogeneous linear problem in the coefficients C_j ($j = 1, ..., 4$), obtained by imposing the boundary conditions (121) to the transverse shape, Eq. (124), represents an eigenvalue problem where $\hat{\omega}_y^2$ is the eigenvalue and the coefficients C_j define the eigenvector. In the present problem, it is found that an infinite set of $\hat{\omega}_y^2$ values exists, where each value is related to a specific transverse mode, and that these values are real numbers. Therefore, it can be concluded that:

- if the smallest eigenvalue $\hat{\omega}_y^2$ is positive ($\min[\hat{\omega}_y^2] > 0$), the trivial configuration is stable because all the eigenmodes have real circular eigenfrequency ω_y;
- if the smallest eigenvalue $\hat{\omega}_y^2$ is negative ($\min[\hat{\omega}_y^2] < 0$), the trivial configuration is unstable because at least one of the eigenmodes has an imaginary circular eigenfrequency ω_y (corresponding to a divergent oscillation);
- if one of the eigenvalues $\hat{\omega}_y^2$ vanishes, the trivial configuration is at the transition between the two previous cases for the specific eigenmode. This condition is the dynamic counterpart of the previously analysed bifurcation for quasi-static deformation.[7]

As example, the smallest eigenvalue $\hat{\omega}_y^2$ is reported as a function of the dimensionless load p in Fig. 13, for $f''(0) = -6$ and two different stiffness ratios, $q = 6.5$ (left) and $q = 8.5$ (right), representative of sets $\mathcal{A}$ and $\mathcal{B}$, respectively. Load ranges realizing stable (unstable) trivial configuration, and corresponding to positive (negative) smallest eigenvalue $\hat{\omega}_y^2$, are highlighted as white (gray) regions. These plots confirm the dimensionless load ranges corresponding to stable and unstable straight configuration as expressed by Eq. (101) for set $\mathcal{A}$ and by Eq. (102) for $\mathcal{B}$, and the associated restabilization and double-restabilization phenomena.

7 The equation of motion $(116)_2$, in the case when $\hat{\omega}_y^2 = 0$, is equivalent to the bifurcation equation (92), obtained for quasi-static deformation. These two just differ in the reference kinematic field, corresponding to $\widehat{Y}(S)$ in dynamics and $\theta(S)$ for quasi-static deformation. These are related to each other through $\widehat{Y}'(S) = (1 + p)\,\theta(S)$ under the small rotation assumption.

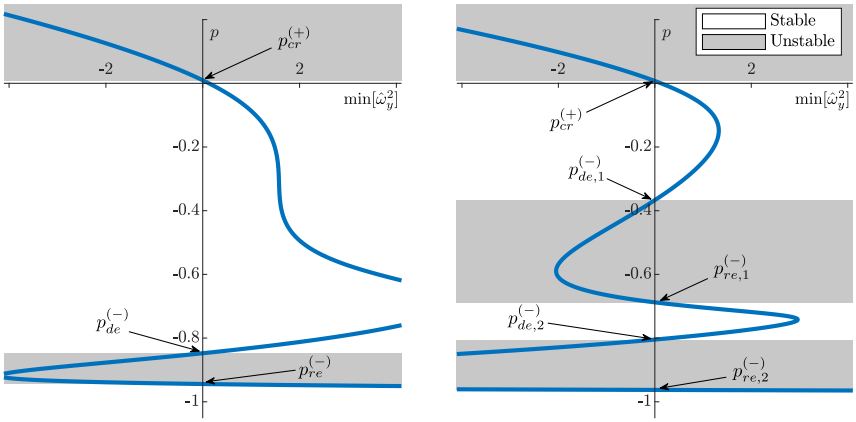

Figure 13: Smallest eigenvalue $\hat{\omega}_y^2 = \gamma\,\omega_y^2 L^4/(\pi^4 B)$ for $f''(0) = -6$ when the dimensionless applied load p is varied. Two stiffness ratios are considered to analyse the stability in subset $\mathcal{A}$ (left, $q = 6.5$) and subset $\mathcal{B}$ (right, $q = 8.5$). Stability (or instability) of the straight configuration corresponds to positiveness (or negativeness) of the smallest eigenvalue $\hat{\omega}_y^2$. Restabilization (left) or double restabilization (right) is found.

3.4 ANALYTICAL SOLUTION FOR THE NONLINEAR KINEMATICS OF THE STRUCTURE

3.4.1 *Imposition of the curved profile constraint*

The general solution for a cantilever beam recalled in Chapter 2 is now considered as having unknown reaction force R and angle α. Because the load P is imposed at the sliding clamp, equilibrium implies the following relation between the angle $\alpha \in [-\pi, \pi]$ and the positive reaction force R

$$P = R\cos\alpha. \tag{126}$$

Due to the absence of friction, the reaction force R is perpendicular to the constraint profile, relating α with the vertical deflection of the free end of the cantilever beam d_Y as[8]

$$\alpha = \arctan\left(f'\left(\frac{d_Y}{L}\right)\right) + \frac{\pi}{2}[1 - \operatorname{sgn}(P)]. \tag{127}$$

Recalling from Eq. (79) that

$$X(L) = d_X, \qquad Y(L) = d_Y, \tag{128}$$

8 The definition (127) for the angle α is introduced to ensure positiveness of the profile reaction, $R > 0$, independently from the sign of the applied load P. Moreover, the restriction $R > 0$ is also needed to exploit the solution obtained in [6].

these two quantities can be expressed as a respective function, $\mathcal{G}_X$ and $\mathcal{G}_Y$ (for conciseness not explicitly reported here), depending on the angle α and the reaction magnitude R,

$$d_X = \mathcal{G}_X(\alpha, R), \quad d_Y = \mathcal{G}_Y(\alpha, R). \tag{129}$$

Because $\kappa(L) = 0$, the parameter k can be related with the rotation of the beam at the free end $\theta_L = \theta(L)$, by evaluating (24) at $S = L$, through the following formula

$$k = \sin\frac{\theta_L + \alpha}{2}. \tag{130}$$

Considering Eq. (126), relation (129) can be rewritten as

$$d_X = \mathcal{G}_X\left(\alpha, \frac{P}{\cos\alpha}\right), \qquad d_Y = \mathcal{G}_Y\left(\alpha, \frac{P}{\cos\alpha}\right), \tag{131}$$

and, since the angle α is related to d_Y through Eq. (127), Eq. $(131)_2$ provides a fixed-point recursive relation for the value of d_Y.

The nonlinear equilibrium configurations can be obtained by solving a reverse problem, where the displacement Δ is imposed while the load P is unknown. In this way, Eqs. (78), (131), and (27) provide a system of three nonlinear equations in the three unknown parameters P, θ_L, and d_Y to be solved for a given Δ value

$$\begin{cases} \mathcal{G}_X\left(\alpha, \dfrac{P}{\cos\alpha}\right) - L\left[1 + f\left(\dfrac{d_Y}{L}\right)\right] - \Delta = 0, \\ \mathcal{G}_Y\left(\alpha, \dfrac{P}{\cos\alpha}\right) - d_Y = 0, \\ k\dfrac{\operatorname{sn}(C, \tilde{k})}{\sqrt{1 + m^2\operatorname{cn}^2(C, \tilde{k})}} - \sin\dfrac{\alpha}{2} = 0, \end{cases} \tag{132}$$

where $\tilde{k}$ is defined by Eq. $(11)_3$.

Due to the nonlinearity of system (132), none, one, or multiple non-trivial equilibrium configurations can be obtained for a given value of the end displacement Δ.

3.4.2 *Symmetric profile*

Reference is made to a parabolic constraint profile (symmetric about the $\widehat{X}$–axis) and described by

$$f(\xi) = 1 + \frac{f''(0)}{2}\,\xi^2, \tag{133}$$

where $\xi = \widehat{Y}/L$.

The equilibrium paths in terms of load p as a function of the clamp displacement Δ/L, rotation θ_L, and vertical coordinate d_Y/L of the end of the rod are shown in Fig. 14 for $f''(0) = -10$. Two different values of q are considered, $q = 8.4$ and $q = 10$, corresponding to a single and a double restabilization, respectively. Stable and unstable configurations are distinguished through continuous and dotted lines, respectively.[9] Restricting attention to non-trivial configurations, the force-displacement diagrams reveal one stable non-trivial configuration (highlighted with red lines) and, as a result, the system is bistable. Because none of the non-trivial bifurcation paths (highlighted with green dotted lines) is stable in compression, the loss of stability at these bifurcation points realizes a 'snap' motion towards the non-trivial stable configuration, as shown by the arrows in Fig. 14. Moreover, since $f''(0)$ is negative, a tensile bifurcation exists. The non-trivial path (highlighted with purple lines) at the tensile bifurcation is found to be stable.

3.4.3 *Skew-symmetric profile with discontinuous curvature at the origin*

A profile, skew-symmetric about the $\widehat{X}$–axis, is considered as

$$f(\xi) = 1 + \frac{f''(0^+)}{2}\,\xi\,|\xi|\,, \tag{134}$$

displaying a discontinuity in the profile curvature at the origin,

$$f''\left(0^-\right) = -f''\left(0^+\right). \tag{135}$$

For this system, attention is restricted only to the continuous stable path in terms of $p\,q$–Δ/L, reported in Fig. 15 for $q = \{4, 30\}$ and $f''\left(0^+\right) = \{2,\ 10\}$. It can be noted that, although the profile shape is skew-symmetric

9 Stability character of the non-trivial configurations and snap motion towards them have been assessed through the numerical solution of the nonlinear dynamic equations (112) and (113).

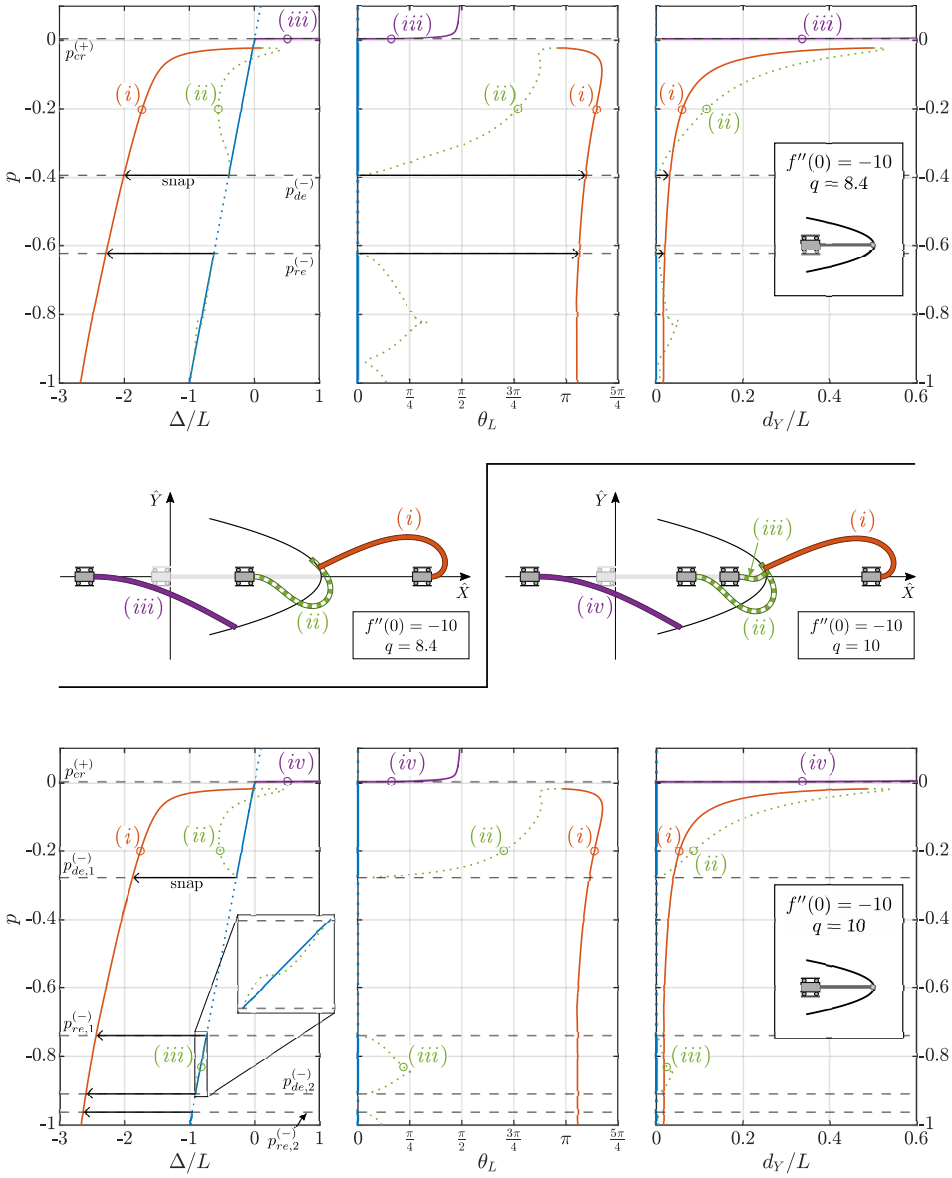

Figure 14: Post-critical behaviour in terms of dimensionless force p versus different measures of structural deformation: clamp displacement Δ, right end rotation θ_L and vertical displacement d_Y. $f''(0) = -10$ and $q = 8.4$ (upper part) and $q = 10$ (lower part). Some stable and unstable deformed configurations are shown for specific non-trivial states in the central part.

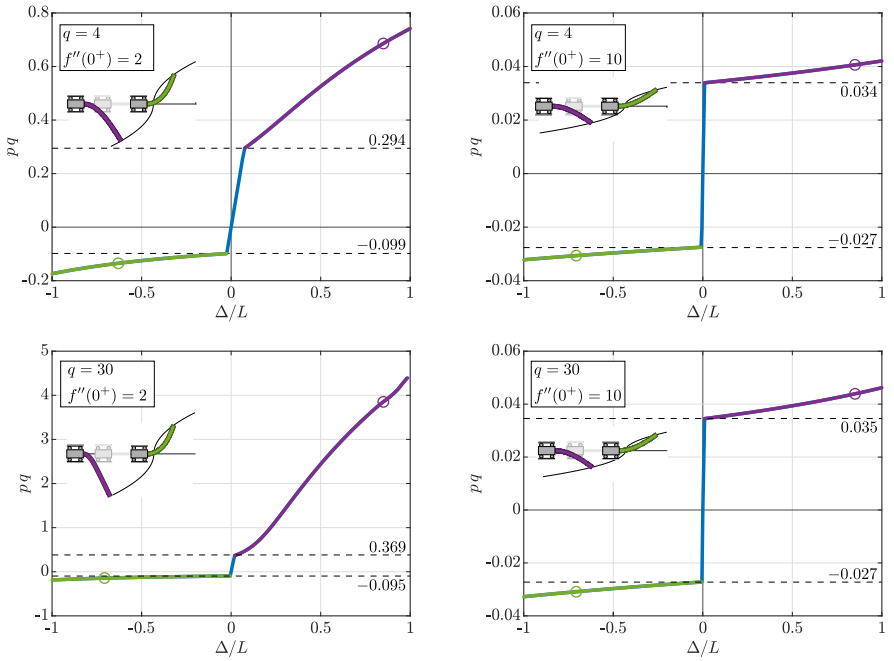

Figure 15: Force ($pq = PL^2/(\pi^2 B)$) – displacement (Δ/L) diagram for a structure with $q = 4$, 30 and skew-symmetric profile defined by Eq. (134) with $f''(0^+) = 2$ (left) and $f''(0^+) = 10$ (right). The deformed shapes shown in the inset correspond to the pq–Δ/L pairs highlighted with a circle (with corresponding colour) on the non-trivial path.

about the $\widehat{X}$–axis, the force-displacement curve does not evidence any symmetry, except along the trivial branch before bifurcation. In fact, the post-buckling behavior of the system depends not only on the constraint shape but also on the signs of the profile angle $f'(\xi)$ and curvature $f''(\xi)$.

3.5 OPTIMIZATION OF THE PROFILE SHAPE FOR A DESIGN FORCE-DISPLACEMENT CURVE

The developed theoretical framework is exploited here to design a device displaying a prescribed force-displacement $p - \Delta/L$ curve. The structure displays a linear elastic range, limited within the tensile/compressive bi-

furcations, $p = \Delta/L \in \left[p_{cr}^{(-)}, p_{cr}^{(+)}\right]$, defined by Eq. (106). The design force-displacement curve is assumed to be characterized as

$$p\left(\frac{\Delta}{L}\right) = \begin{cases} p^{(-)}\left(\frac{\Delta}{L}\right), & \frac{\Delta}{L} < p_{cr}^{(-)}, \\ \frac{\Delta}{L}, & \frac{\Delta}{L} \in \left[p_{cr}^{(-)}, p_{cr}^{(+)}\right], \\ p^{(+)}\left(\frac{\Delta}{L}\right), & \frac{\Delta}{L} > p_{cr}^{(+)}, \end{cases} \tag{136}$$

where $p^{(+)}(\Delta/L)$ and $p^{(-)}(\Delta/L)$ define a target behaviour to be displayed after bifurcation, tensile and compressive, respectively, and satisfying the continuity condition

$$p^{(\pm)}\left(p_{cr}^{(\pm)}\right) = p_{cr}^{(\pm)}. \tag{137}$$

Considering that the two critical values are independent of each other, a discontinuous profile curvature at the origin is needed to control independently these two thresholds as related to the tensile and compressive loading branches of the structure. As previously shown, the stiffness ratio q and two profile curvatures at the origin $f''(0^-)$ and $f''(0^+)$ have to lie within the ranges provided by Eq. (110).

The post-buckling displacement Δ is discretized in the two sets $\Delta_i^{(\pm)}$, characterized by $N^{(\pm)}$ discretization points ($i = 0, ..., N^{(\pm)}$), satisfying

$$\Delta_0^{(\pm)} = p_{cr}^{\pm} L, \qquad \left|\Delta_{i+1}^{(\pm)}\right| > \left|\Delta_i^{(\pm)}\right|, \qquad \pm\Delta_i^{(\pm)} > 0. \tag{138}$$

Considering the profile as the union of two parts differing in the sign of Y, the dimensionless coordinate Y/L is discretized through the unknown points $\xi_i^{(\pm)}$, corresponding to $\Delta_i^{(\pm)}$, where

$$\xi_0^{(\pm)} = 0^{\pm}, \qquad \left|\xi_{i+1}^{(\pm)}\right| > \left|\xi_i^{(\pm)}\right|, \qquad \pm\xi_i^{(\pm)} > 0. \tag{139}$$

The profile shape is discretized as

$$\begin{aligned} f(\xi) = 1 + \frac{1}{2}\sum_{j=0}^{i-1} h_{j+1}^{(\pm)}\left(\xi_{j+1}^{(\pm)} - \xi_j^{(\pm)}\right)^2 \\ + \frac{1}{2} h_{i+1}^{(\pm)}\left(\xi - \xi_i^{(\pm)}\right)^2, \quad \xi \in \left[\xi_i^{(\pm)}, \xi_{i+1}^{(\pm)}\right], \end{aligned} \tag{140}$$

where $h_{i+1}^{(\pm)}$ is the piecewise constant profile curvature value,

$$f''(\xi) = h_{i+1}^{(\pm)}, \qquad \xi \in \left(\xi_i^{(\pm)}, \xi_{i+1}^{(\pm)}\right). \tag{141}$$

In order to achieve the target force-displacement curve, a fitting loop is devised. The algorithm initiates with $i = 0$ and is repeated for increasing values of i. After selecting the stiffness ratio q of the rod, the generic unknown point $\xi_{i+1}^{(\pm)}$ and corresponding profile curvature value $h_{i+1}^{(\pm)}$ can be found through a solution of the nonlinear system (132) by imposing $\Delta_{i+1}^{(\pm)}$ and prescribing the force p in agreement with the target response, Eq. (136), as

$$p\left(\frac{\Delta_{i+1}^{(\pm)}}{L}; \xi_{i+1}^{(\pm)}, h_{i+1}^{(\pm)}\right) = p^{(\pm)}\left(\frac{\Delta_{i+1}^{(\pm)}}{L}\right). \tag{142}$$

It is worth noting that the profile optimization can be unsuccessful at a specific value of Δ for the following issues.

Issue 1 – A too stiff response is requested. Indeed, the target force-displacement curve $p^{(\pm)}(\Delta/L)$ has its first derivative bounded from above by the maximum post-critical stiffness ratio $k_{max} \in (0, 1)$ as[10]

$$\frac{dp^{(\pm)}(\Delta/L)}{d(\Delta/L)} < k_{max}\left(q, \widehat{Y}\right), \tag{144}$$

because a unit value would correspond to the stiffest behaviour given by the purely axial state, which is instead weakened in the post-critical region by flexure. It is also observed that high values of q and $\widehat{Y}$ define small maximum post-critical stiffness ratio k_{max};

Issue 2 – The elastica is unstable. Although a profile shape is found, the involved equilibrium configuration of the rod may become unstable. In particular, the stable/unstable response is affected by

10 The profile can be designed for realizing a post-bifurcation response with incremental negative stiffness,

$$\frac{dp^{(\pm)}(\Delta/L)}{d(\Delta/L)} < 0, \tag{143}$$

a concept under research for applications in vibration isolation and seismic engineering; see e.g. [2, 35, 49, 68].

the prescribed boundary condition, namely, it may change depending on whether the displacement Δ or the load p are imposed;

Issue 3 – A force reversal [11, 13, 14] is excluded. Because the profile shape is described via the horizontal coordinate $\widehat{X}$ through the function $f\left(\widehat{Y}/L\right)$, Eq. (77), the present formulation cannot be exploited to realize force reversals (p changing sign at a given end displacement $\Delta \neq 0$). Therefore, the target response is subject to the following constraint

$$\pm p^{(\pm)} > 0. \tag{145}$$

In the limit condition given by $p = 0$, the optimization procedure fails providing $f' \to \infty$, because the only possible equilibrium configuration is realized for a reaction inclination angle $\alpha = \pm\pi/2$.

While the first two issues above are inherent to the considered model and cannot be avoided, the latter restriction can be overcome through a parametric planar description of the profile curve, as for example describing the profile as $\hat{X}(\sigma)$ and $\hat{Y}(\sigma)$ through a parameter σ.

In the following, examples of application of the optimization algorithm are presented by considering a uniform spacing $\Delta_{i+1}^{(\pm)} - \Delta_i^{(\pm)} = \left(\Delta_N^{(\pm)} - \Delta_0^{(\pm)}\right)/N^{(\pm)}$ in the discretization, with $N^{(\pm)} = 120$, $\Delta_N^{(\pm)} = 2L$.

The following examples are also complemented by movies (available as electronic supplementary material) showing the theoretical behaviour of the structure optimized to display specific force-displacement curves.

3.5.1 *The design of an elastic force-limiting device*

In an ideal force-limiting device, the force P is expected to be initially linear with the displacement Δ, up to a threshold value at which the bifurcation occurs. Subsequently, the force is requested to remain constant (or slightly raise in its absolute value) at a further increase in the displacement magnitude, up to a point where the structure locks and the stroke of the device is attained. In practice however, a small increase in the force magnitude after buckling is desirable, to facilitate the return of the device to its initial configuration at unloading and to avoid snap motion due to

negative stiffness. By excluding for the moment the final locking part, this behaviour can be described in mathematical terms as a symmetric bilinear force-displacement curve, namely, Eq. (136) with $p^{(\pm)}$ given as

$$p^{(\pm)}\left(\frac{\Delta}{L}; p_{cr}, r\right) = \pm p_{cr} + r\left(\frac{\Delta}{L} \mp p_{cr}\right), \tag{146}$$

where r is the bilinear stiffness ratio, relating the incremental constant stiffness in the post-buckling regime to that characterizing the structure before bifurcation (therefore enforced by Eq. (144) to $r < k_{max} < 1$), and $p_{cr} = p_{cr}^{(+)} = -p_{cr}^{(-)}$.

The constraint's profile, which realizes a certain designed force-displacement behaviour (defined by p_{cr} and r), is not unique, rather, various shapes of the profile, realizing the target post-buckling behaviour $p^{(\pm)}$, can be found using the algorithm described in the previous section as a function of q.

A number of constraint's profile shapes are shown in Fig. 16 for $p_{cr} = \{0.01, 0.05, 0.3\}$ (from top to the bottom). The same force-displacement behaviour (reported in the insets) is obtained by changing q, assuming 2 pairs of values reported in each diagram. Profile shapes with different colours correspond to different values of bilinear stiffness ratio $r = \{-0.01, 0, 0.01\}$ (top), $r = \{-0.04, 0, 0.04\}$ (middle) and $r = \{-0.35, 0, 0.35\}$ (bottom).

Restricting attention to a null bilinear stiffness ratio, $r = 0$, the profile shapes are shown in Fig. 17 for $p_{cr} = 0.01$ (top left), $p_{cr} = 0.05$ (top right), and $p_{cr} = 0.3$ (bottom), for different values of the stiffness ratio q. The force-displacement diagrams are reported in the insets.

In both Figs. 16 and 17, some of the profile shapes and the corresponding load-displacement curves are ended with a marker (a cross or a circle). This marker shows the point where the optimization algorithm fails to converge because the target stiffness is too high (Issue 1, marked with a cross), or because a force reversal is found (Issue 3, marked with a circle). It should be noted that the blue curves in Fig. 16 show negative stiffness and therefore are unstable for imposed load p.

Also, small values of q provide smoother profiles than those obtained for large q. Moreover, small values of q lead to a large stroke, defined as the greatest displacement Δ reached with the device, see Fig. 17, showing that rod's extensibility facilitates the profile optimization. It is noted that small values of q can be obtained by using elements such as those described in Sect. 3.1.1. On the other hand, rods that are inextensible

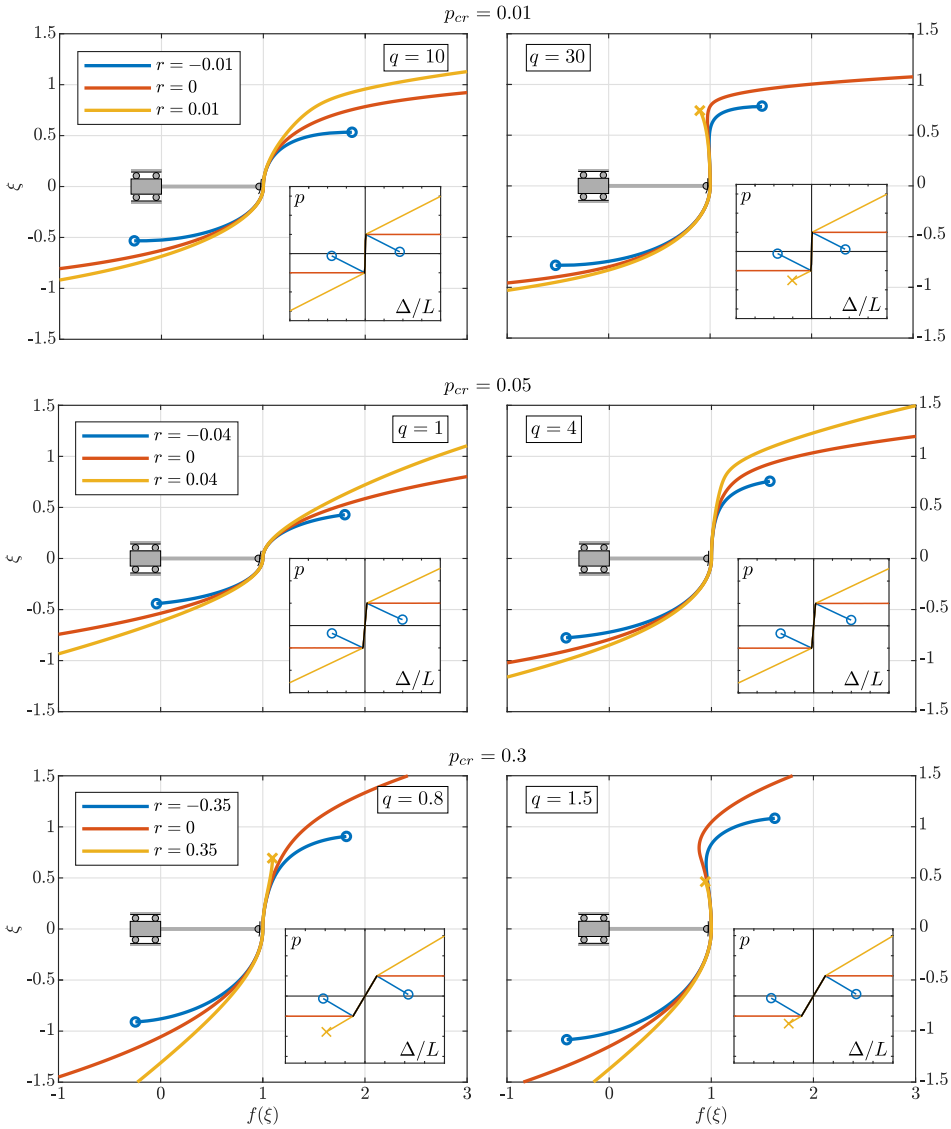

Figure 16: Profile's shapes realizing a symmetric bilinear force-displacement $p - \Delta$ curve (shown in the insets) with $p_{cr} = \{0.01, 0.05, 0.3\}$ (from top to the bottom) for three different values of the bilinear stiffness ratio $r = \{-0.01, 0, 0.01\}$ (top), $r = \{-0.04, 0, 0.04\}$ (middle) and $r = \{-0.35, 0, 0.35\}$ (bottom). Crosses and circles denote the points where the design $p - \Delta$ fails, putting out-of-service the device.

$(q \to \infty)$ could be used to achieve the same effect, although inextensibility reduces the performance of the device.

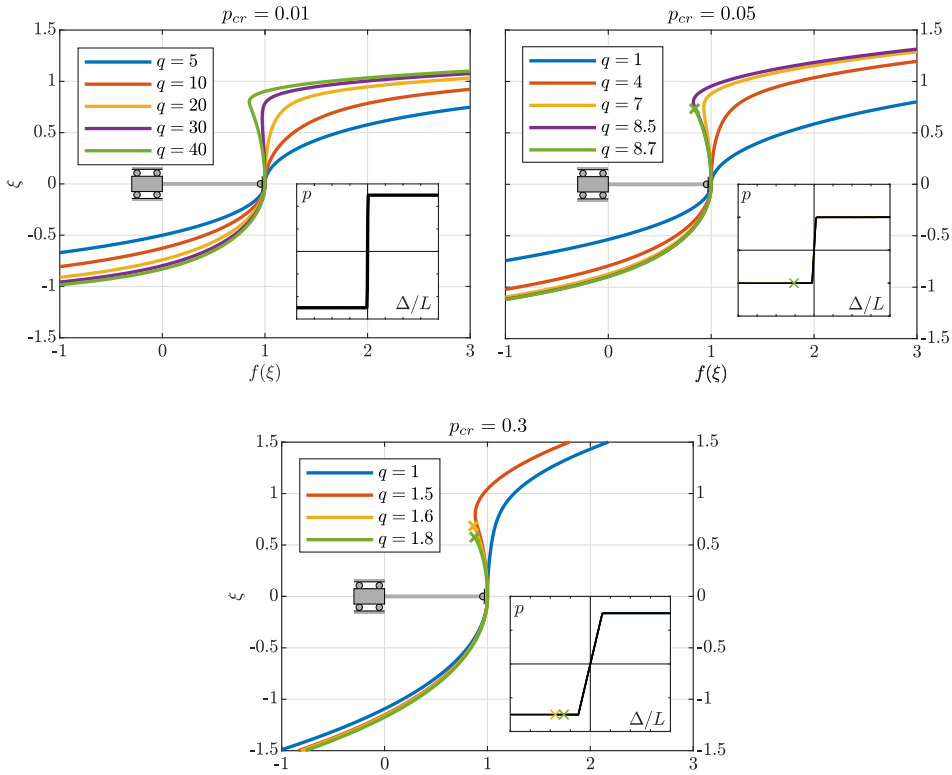

Figure 17: Profile's shapes realizing a symmetric bilinear force-displacement $p - \Delta$ curve with null bilinear stiffness ratio (shown in the insets), $r = 0$, for $p_{cr} = 0.05$ (top left), $p_{cr} = 0.05$ (top right) and $p_{cr} = 0.3$ (bottom). Crosses denote the points where the design $p - \Delta$ fails, putting out-of-service the device. Note that small values of q extend the range of displacement for which the designed response is displayed.

For the practical realization of a force-limiter, a secondary increase in the stiffness has to be introduced in order to achieve a smooth transition to a maximum allowable displacement Δ_{max}. This secondary increase in the stiffness can be achieved by modifying the final part of the profile shape. An example for $p_{cr} = 0.01$, $q = 10$, $r = 0$, and locking starting at $\Delta/L = \pm 0.73$ is shown in Fig. 5, along with the profile shape and the deformed configuration at $\Delta/L = \pm\{0.1, 0.2, 0.8\}$.

3.5.2 *Profile shape for complex force-displacement curves*

To show how far the present framework can be exploited to design constraint's profiles imposing highly complicated load-displacement curves,

the present analysis is concluded by finding the profile shapes for a sinusoidal post-critical response (with constant average load),

$$p^{(\pm)}\left(\frac{\Delta}{L}; p_{cr}, a, b\right) = \pm p_{cr} + a \sin\left[2\pi b\left(\frac{\Delta}{L} \mp p_{cr}\right)\right] \tag{147}$$

and for a *triangular* post-critical response (with non-constant average load),

$$\begin{aligned} p^{(\pm)}\left(\frac{\Delta}{L}; p_{cr}, r_1, r_2, c\right) = \pm p_{cr} + r_1\left(\frac{\Delta}{L} \mp p_{cr}\right) \\ \mp r_2\left|c\left(\frac{\Delta}{L} \mp p_{cr}\right) - \left\lfloor c\left(\frac{\Delta}{L} \mp p_{cr}\right) + \frac{1}{2}\right\rfloor\right|, \end{aligned} \tag{148}$$

with the symbol $\lfloor\cdot\rfloor$ standing for the integer part of the relevant argument. Both the above design post-critical responses define a multistable element, where more than one stable displacement Δ exist at a given load p.

The profile shape for the sinusoidal response (147) with $a = 0.05$ and $b = 2$ is reported in Fig. 18 (upper row) while that for the triangular one (148) with $r_1 = 0.05$, $r_2 = 0.1$, and $c = 2$ in Fig. 18 (lower row). Two values of critical load are prescribed, $p_{cr} = 0.1$ (left) and $p_{cr} = 0.2$ (right), while the stiffness ratio assumes three values, $q = \{0.5, 1, 2\}$. Similarly to the bilinear post-critical response, also for these other two cases, it is evident that the profile shape becomes smoother and can be defined for greater Δ and for small values of q.

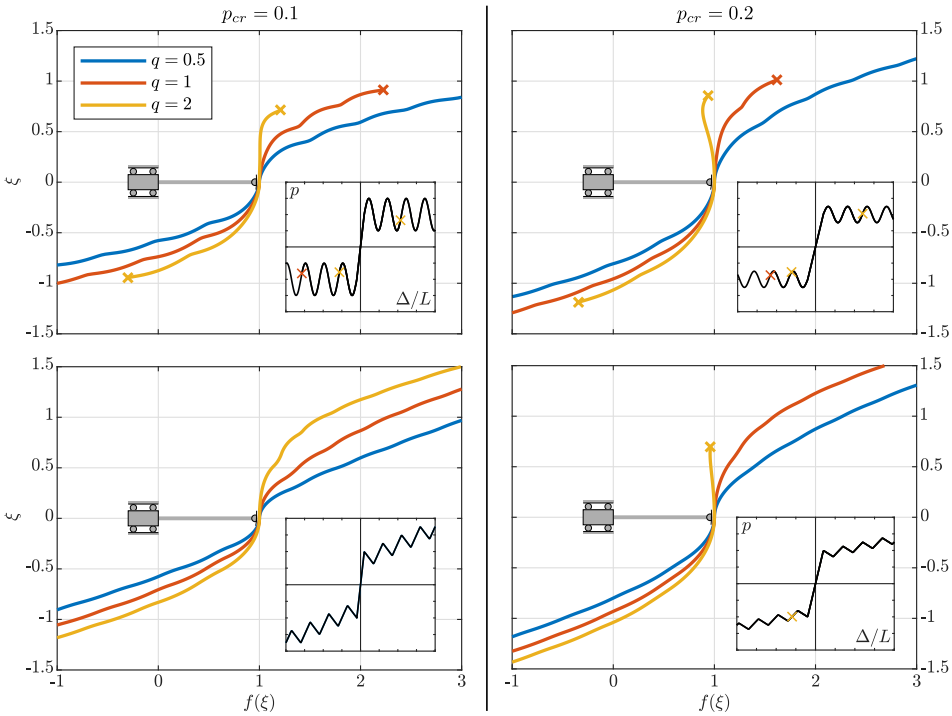

Figure 18: Constraint's profile shapes optimized for realizing (above) a sinusoidal force-displacement response, Eq. (147), with $a = 0.05$ and $b = 2$ and (bottom) a triangular response, Eq. (148), with $r_1 = 0.05$, $r_2 = 0.1$, and $c = 2$. Critical load is $p_{cr} = 0.1$ (left) and $p_{cr} = 0.2$ (right). Different shapes are reported for different values of the stiffness ratio q.

4 THE OSCILLATING SLIDING SLEEVE

In this chapter the oscillating sliding sleeve system is presented and analysed. First, the theoretical model of the system is provided using the rotation- and position-based formulations. While the former is used to derive a simple expression for the equations of motion and to attempt the description of an analytical solution, the latter leads to a robust Finite Element framework for the sliding-sleeve constraint. The general model for the system where the sleeve can move both horizontally and vertically is presented. Next, the system is studied both analytically and numerically for the case that only horizontal movement of the sliding-sleeve is considered. Finally, the analysis is concluded with an experimental campaign that confirms the theoretical predictions.

4.1 INTRODUCTION

The oscillating sliding sleeve system is composed by a flexible but inextensible rod, of length L, flexural stiffness B, linear mass density γ, and straight in its undeformed configuration, partially inserted inside a sliding sleeve. A mass m is attached at the tip of the rod and the sleeve is oriented in a vertical direction, as seen in Fig. 19. As mentioned in Chapter 1, the oscillation of the sliding sleeve constraint provides an external input that allows the system to exhibit a quasi-periodic motion. Anticipating the results, three qualitatively different behaviours can be observed; injection, ejection and quasi-periodic motion. The injection/ejection of the rod in/from the sliding sleeve represent behaviours that have been also experimentally observed in the case of motion absence for the sliding constraint [3, 9]. Differently, the quasi-periodic motion can be realized only when the sleeve is oscillating.

4.1.1 *Configurational forces*

Ignoring for the moment any friction effects inside the sliding sleeve, the vertical inertia is balanced by the sum of the gravity and the configurational force, the latter due to the discontinuity of the curvature of the rod

at the sliding sleeve exit. This force is realized at the sliding sleeve exit and is always outward from the sliding sleeve. Previous research [3, 9] confirms the relation for the magnitude of the configurational force

$$|F_C(t)| = \frac{M^2(t)}{2B}, \tag{149}$$

where $M(t)$ is the reaction moment at the sliding sleeve. As the sleeve oscillates and the rod-mass system is excited, the configurational force oscillates also. As a consequence, the oscillatory configurational force may play the role of dynamic stabilizer realising a quasi-periodic motion.

4.1.2 *Connection with resonant clamped-free rod*

The oscillating sliding sleeve system described above has self-tuning properties. When the system is excited at an angular frequency ω, the length of the rod external to the sliding sleeve adjusts so that the excitation frequency ω matches the natural frequency of a clamped rod of the same length. This prediction is obtained by analytical means and experiments carried out in the Instabilities Laboratory of the University of Trento confirm this finding.

4.2 THEORETICAL MODELING WITH THE ELASTICA

4.2.1 *Governing equations*

Because of the presence of the sliding sleeve, in addition to the rotation field $\theta(s,t)$, the structural system is also characterized by the configurational parameter $\ell(t) \in [0, L]$ measuring the length of the rod outside the constraint, defined by the set of points $s \in [L-\ell(t), L]$, being L the length of the entire rod. Considering the sliding sleeve exit as the origin of the $x-y$ reference system implies the following kinematic constraints for the position field at the curvilinear coordinate $s = L-\ell(t)$

$$X\big(L-\ell(t),t\big) = U(t), \qquad Y\big(L-\ell(t),t\big) = V(t), \tag{150}$$

$$x\big(L-\ell(t),t\big) = y\big(L-\ell(t),t\big) = 0, \tag{151}$$

while the rotation field of the part of the rod inside of the sliding sleeve remains null,

$$\theta(s,t) = 0, \qquad s \in [0, L-\ell(t)]. \tag{152}$$

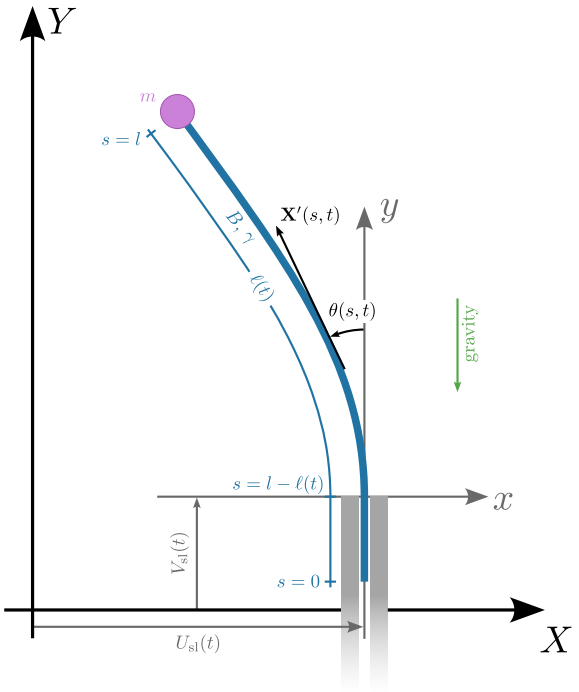

Figure 19: Oscillating sliding sleeve system. The rod of flexural stiffness B is inserted partially inside the sliding sleeve and a concentrated mass m is attached to the rod tip. The sliding-sleeve is allowed to move in the horizontal and in the vertical direction.

The time derivative of the null rotation condition (152) evaluated at the curvilinear coordinate corresponding to the sliding sleeve exit, $\theta(L-\ell(t),t)=0$, provides the following internal constraint between the time and spatial derivatives (the latter denoted by a prime symbol) of the rotational field at this point through the sliding velocity $\dot{\ell}(t)$ as

$$\dot{\theta}\left(L-\ell(t),t\right)=\dot{\ell}\left(t\right)\theta'\left(L-\ell(t),t\right). \tag{153}$$

From Eq.(153) it follows that, while the velocity fields are continuous at the sliding sleeve exit, the velocity of rotation $\dot{\theta}(s,t)$ is spatially discontinuous at $s=L-\ell(t)$ because of the discontinuity of the curvature field at the same point, so that the velocity of rotation can be evaluated just inside and outside the sliding sleeve as

$$\begin{aligned}&\lim_{|\delta|\to 0}\dot{\theta}\left(L-\ell(t)-|\delta|,t\right)=0,\\&\lim_{|\delta|\to 0}\dot{\theta}\left(L-\ell(t)+|\delta|,t\right)=\dot{\ell}(t)\lim_{|\delta|\to 0}\theta'\left(L-\ell(t)+|\delta|,t\right).\end{aligned} \tag{154}$$

The relative coordinates of the rod inside the sliding sleeve are trivially given as

$$\begin{aligned} x(s,t) &= 0, \\ y(s,t) &= s - L + \ell(t), \quad \forall s \in [0,\, L-\ell(t)], \end{aligned} \tag{155}$$

and the relative coordinated outside the sliding sleeve can be obtained by integrating the rotation field $\theta(s,t)$ as

$$\begin{aligned} x(s,t) &= \int_{L-\ell(t)}^{s} \sin\theta(s,t)ds, \\ y(s,t) &= \int_{L-\ell(t)}^{s} \cos\theta(s,t)ds, \quad \forall s \in [L-\ell(t), L]. \end{aligned} \tag{156}$$

The absolute coordinates of a point s on the rod outside the sliding-sleeve $s \in [L-\ell(t), L]$, in the earth-fixed inertial frame of reference $X-Y$, are decomposed in the following form

$$X(s,t) = U_{sl}(t) + x(s,t), \quad Y(s,t) = V_{sl}(t) + y(s,t), \tag{157}$$

where $U(t)$ and $V(t)$ are the displacements of the sliding sleeve exit in the horizontal and veritcal directions respectively, as seen in Fig. 19, and $x(t)$, $y(t)$ are the coordinates of the rod in the reference frame travelling with the sliding-sleeve and given by Eq. (156).

4.2.2 *Lagrangian and governing equations*

The Lagrangian $\mathcal{L}(t)$ for the considered system is given by

$$\begin{aligned} \mathcal{L}(t) = \;& \mathcal{T}(t) - \mathcal{V}(t) - \int_{L-\ell(t)}^{L} N_X(s,t)\,\left[X'(s,t) - \sin\theta(s,t)\right] ds \\ & - \int_{L-\ell(t)}^{L} N_Y(s,t)\,\left[Y'(s,t) - \cos\theta(s,t)\right] ds \\ & - \int_{0}^{L-\ell(t)} N_y(s,t)\,\left[y'(s,t) - 1\right] ds, \end{aligned} \tag{158}$$

where $\mathcal{T}(t)$ is the kinetic energy, $\mathcal{V}(t)$ is the potential energy, while $N_x(s)$ and $N_y(s)$ are Lagrangian multipliers (which can be mechanically interpreted as the internal forces along the x and y directions). Considering that the rod has uniform linear mass density γ and has attached a lumped

mass m (with rotational inertia I) at the coordinate $s = L$, the kinetic energy $\mathcal{T}(t)$ of the system is given by

$$\mathcal{T}(t) = \frac{m\,[\dot{X}(L,t)^2 + \dot{Y}(L,t)^2]}{2} + \frac{1}{2}\int_0^L \gamma\,[\dot{X}(s,t)^2 + \dot{Y}(s,t)^2]ds. \qquad (159)$$

The potential energy $\mathcal{V}(t)$ is given as the sum of the elastic energy stored inside of the rod and the negative of the work done by the loads applied to the system. A quadratic form in the rod's curvature $\theta'(s,t)$ is assumed for the strain energy of the elastic rod, so that the moment at the coordinate s is given by the linear relation $M(s,t) = B\theta'(s,t)$, where B is the uniform bending stiffness. Considering a gravitational field characterized by the acceleration g in the direction opposite to the y axis, the concentrated dead load $P = mg$ is applied at the coordinate $s = L$, while the uniform dead load γg is distributed all along the rod, the potential energy $\mathcal{V}(t)$ (neglecting an arbitrary constant) is given by

$$\mathcal{V}(t) = \frac{B}{2}\int_{L-\ell(t)}^{L} \theta'(s,t)^2\,ds + PY(L,t) + \int_0^L \gamma\,g\,Y(s,t)ds. \qquad (160)$$

The principle of least action can be applied to the functional $\mathcal{A}$ defined as the integration in time of $\mathcal{L}(t)$

$$\mathcal{A} = \int_{t_0}^{t^*} \mathcal{L}(t)\;dt, \qquad (161)$$

with t_0 and t^* being arbitrary initial and final instants of the analyzed time interval. The minimization procedure for the functional $\mathcal{A}$ is expressed by the vanishing of its variation (see Appendix A for details) and leads to the following equations of motion for the part of the rod inside the sliding sleeve

$$N_y'(s,t) = \gamma\left\{\ddot{V}_{sl}(t) - \ddot{\ell}(t)\right\}, \qquad s \in [0, L-\ell(t)], \qquad (162)$$

and for the part of rod outside the sliding sleeve

$$\begin{aligned} &B\theta''(s,t) + N_X(s,t)\cos\theta(s,t) - N_Y(s,t)\sin\theta(s,t) = 0,\\ &N_X'(s,t) - \gamma\ddot{X}(s,t) = 0,\\ &N_Y'(s,t) - \gamma\left(\ddot{Y}(s,t) + g\right) = 0, \qquad s \in [L-\ell(t), L]. \end{aligned} \qquad (163)$$

Furthermore, as a complement to the differential systems (162) and (163), the minimization procedure also provides the boundary conditions at the two ends of the rod

$$\begin{aligned} &N_y(0,t) = 0, && N_x(L,t) = -m\ddot{X}(L,t), \\ &N_y(L,t) = -m\left(\ddot{Y}(L,t) + g\right), && M(L,t) = 0, \end{aligned} \tag{164}$$

and the interface boundary condition at the sliding sleeve exit, $s = L - \ell(t)$,

$$[\![N_y(L-\ell(t),t)]\!] = \frac{M(t)^2}{2B}, \tag{165}$$

where $M(t)$ is the reaction moment provided by the sliding sleeve and the symbol $[\![\cdot]\!]$ denotes the jump in the relevant argument at a specific spatial coordinate, namely

$$\begin{aligned} [\![N_j(L-\ell(t),t)]\!] = \lim_{|\delta|\to 0} \Big[& N_j\left(L-\ell(t)+|\delta|,t\right) \\ & - N_j\left(L-\ell(t)-|\delta|,t\right)\Big], \quad j = x,y. \end{aligned} \tag{166}$$

By considering the moment-curvature linear constitutive relation $M(s,t) = B\,\theta'(s,t)$ and the condition of null curvature for the part of rod inside the sliding sleeve, the reaction moment $M(t)$ results coincident with the bending moment in the rod evaluated at the moving curvilinear coordinate $s = \lim_{|\delta|\to 0}(L-\ell(t)+|\delta|)$,

$$M(t) = \lim_{|\delta|\to 0} B\theta'\left(L-\ell(t)+|\delta|,t\right). \tag{167}$$

The moving coordinate $s = L - \ell(t)$ is associated with the cross section at the sliding sleeve exit, so that $M(t)$ corresponds to the bending moment value at the rod cross section just outside the constraint.

4.2.3 *Spatial closed-form solution of the sliding-sleeve system*

The closed form solution of the inextensible elastica and sliding sleeve system has been discussed in [3], for the case where the sliding sleeve is inclined and not moving. Here the same approach is used and adapted for the moving sliding sleeve. In order to obtain the closed-form solution for the sliding-sleeve system we assume that the inertia of the rod is negligible $\gamma = 0$. Then, the mass of the system is just the concentrated mass

m and from Eq. (163) the internal actions $N_X(s,t)$ and $N_Y(s,t)$ are spatially constant with values $\overline{N}_X(t)$ and $\overline{N}_Y(t)$ respectively. The equations of motion of the system can be written as

$$\begin{aligned}\overline{N}_X(t) &= -m\ddot{X}_L(t)\\ &= -m(\ddot{U}_{sl}(t)+\ddot{x}_L(t))\\ \overline{N}_Y(t) &= -m(g+\ddot{Y}_L(t))\\ &= -m(g+\ddot{V}_{sl}(t)+\ddot{y}_L(t)),\end{aligned} \tag{168}$$

where the subscript L denotes the evaluation of the field at $s = L$. The equation of the configurational force can be written as

$$\overline{N}_Y(t) = -\frac{\left[\,\overline{N}_X(t)y_L(t)-\overline{N}_Y(t)x_L(t)\,\right]^2}{2B}. \tag{169}$$

The quantities $\overline{N}_X(t)$ and $\overline{N}_Y(t)$ can be calculated by

$$\begin{aligned}\overline{N}_X(t) &= -\frac{B}{\ell^2(t)}\left[\mathcal{K}(k(t))-\mathcal{K}(\sigma(t),k(t))\right]^2\sin\beta(t)\\ \overline{N}_Y(t) &= -\frac{B}{\ell^2(t)}\left[\mathcal{K}(k(t))-\mathcal{K}(\sigma(t),k(t))\right]^2\cos\beta(t),\end{aligned} \tag{170}$$

where $\mathcal{K}(k(t))$ and $\mathcal{K}(\sigma(t),k(t))$ are the complete and incomplete elliptic integrals of the first kind respectively,

$$\beta(t) = \arctan\left(\frac{\overline{N}_X(t)}{\overline{N}_Y(t)}\right) \tag{171}$$

and

$$k(t) = \sin\frac{\theta_L(t)-\beta(t)}{2}, \quad \sigma(t) = -\arcsin\left[\frac{1}{k(t)}\sin\frac{\beta(t)}{2}\right]. \tag{172}$$

Moreover, the position of the tip of the rod can be evaluated as

$$\begin{aligned}x_L(t) &= \ell(t)\{A(t)\sin\beta(t)-B(t)\cos\beta(t)\},\\ y_L(t) &= \ell(t)\{A(t)\cos\beta(t)+B(t)\sin\beta(t)\},\end{aligned} \tag{173}$$

where

$$\begin{aligned}A(t) &= -1+\frac{2\left[\mathcal{E}(k(t))-\mathcal{E}(\sigma(t),k(t))\right]}{\mathcal{K}(k(t))-\mathcal{K}(\sigma(t),k(t))},\\ B(t) &= -\frac{2\,k(t)\,\cos\sigma(t)}{\mathcal{K}(k(t))-\mathcal{K}(\sigma(t),k(t))},\end{aligned} \tag{174}$$

and $\mathcal{E}(k)$ and $\mathcal{E}(\sigma, k)$ are the complete and incomplete elliptic integrals of the second kind.

Finally, the following differential-algebraic system of equations can be written

$$\begin{cases} m(\ddot{U}_{sl}(t) + \ddot{x}_L(t)) + c(t)(\dot{U}_{sl}(t) + \dot{x}_L(t)) \\ \qquad - \dfrac{B}{\ell^2(t)} \left[\mathcal{K}(k(t)) - \mathcal{K}(\sigma(t), k(t))\right]^2 \sin\beta(t) = 0 \\ m(g + \ddot{V}_{sl}(t) + \ddot{y}_L(t)) + c(t)(\dot{V}_{sl}(t) + \dot{y}_L(t)) \\ \qquad - \dfrac{B}{\ell^2(t)} \left[\mathcal{K}(k(t)) - \mathcal{K}(\sigma(t), k(t))\right]^2 \cos\beta(t) = 0 \\ \overline{N}_Y(t) = -\dfrac{\left[\overline{N}_X(t) y_L(t) - \overline{N}_Y(t) x_L(t)\right]^2}{2B} + \mu\, |\overline{N}_X(t)|\, \mathrm{sgn}[\dot{\ell}(t)] \\ x_L(t) = \ell(t)\{A(t)\sin\beta(t) - B(t)\cos\beta(t)\} \\ y_L(t) = \ell(t)\{A(t)\cos\beta(t) + B(t)\sin\beta(t)\} \end{cases} \tag{175}$$

The first two equations are the differential equations providing the equations of motion of the mass at the tip of the rod and the last three are the algebraic equations acting as constraints on the system. This system can be solved for the five unknowns $x_L(t)$, $y_L(t)$, $\ell(t)$, $\theta_L(t)$ and $\beta(t)$.

The differential system is improved by modelling dissipative behaviour through two different sources. A viscous damping term with time-variable coefficient $c(t)$ is introduced to model the dissipation of the rod and air interaction effects outside the sliding sleeve and equal to

$$c(t) = 2\,\zeta\,\sqrt{\frac{3\,m\,B}{\ell^3(t)}}, \tag{176}$$

where ζ is a non-dimensional value defining the viscous damping coefficient c. A dry (Coulomb) friction inside the sleeve with friction coefficient μ is introduced to model dissipation at the sliding sleeve. In order to assist the convergence of any iterative solver for nonlinear systems of equations, the discontinuous in time dry friction force is approximated by the following nonlinear smooth function

$$F_{\text{friction}} = -\mu\,|\overline{N}_X(t)|\,\mathrm{sgn}[\dot{\ell}(t)] \approx -\mu\,|\overline{N}_X(t)|\,\frac{\dot{\ell}(t)}{\sqrt{\dot{\ell}^2(t) + \epsilon^2}} \tag{177}$$

where ϵ is a small parameter, $\epsilon \ll 1$.

4.3 POSITION-BASED WEAK FORM

In order to develop a Finite Element model, the position-based formulation is used. The extended Lagrangian of the system for the position-based formulation is

$$\begin{aligned}\mathcal{L}(t) = \mathcal{T}(t) - \mathcal{V}(t) - \int_0^{L-\ell(t)} \lambda(s,t)\,\mathbf{n}(t)\cdot[\mathbf{X}(s,t) - \mathbf{U}(t)]\,ds \\ - \int_0^{L} N(s,t)\,\left[(\mathbf{X}'(s,t))^2 - 1\right] ds \\ - \mathbf{R}(t)\cdot[\mathbf{X}(L-\ell(t),t) - \mathbf{U}_{sl}(t)] - M(t)\,\left[\mathbf{n}(t)\cdot\mathbf{X}'(L-\ell^+(t),t)\right],\end{aligned} \tag{178}$$

where $\lambda(s,t)$ can be interpreted as the transverse reaction inside the sliding sleeve, $\mathbf{R}(t)$ and $M(t)$ as the reaction force and moment at the sliding sleeve opening (modelling the discontinuities), $N(s,t)$ as the internal action of the rod in the axial direction and

$$\mathcal{T}(t) = \int_0^L \frac{1}{2}\gamma\,(\dot{\mathbf{X}}(s,t))^2\,ds + \frac{1}{2}m\,(\dot{\mathbf{X}}(L,t))^2, \tag{179}$$

is the kinetic energy of the system and

$$\mathcal{V}(t) = \int_0^L \frac{1}{2}B\,(\mathbf{X}''(s,t))^2\,ds - \int_0^L \gamma\,\mathbf{X}(s,t)\cdot\mathbf{g}\,ds - m\,\mathbf{g}\,\mathbf{X}(L,t), \tag{180}$$

is the potential energy. The application of the Principle of Least Action to Eq. (178) leads to the equations of motion in weak form as

$$\begin{aligned}
&\int_{t_0}^{t^*}\int_0^L \gamma\,\delta\mathbf{X}(s,t)\cdot\ddot{\mathbf{X}}(s,t)\,ds\,dt+\int_{t_0}^{t^*} m\,\delta\mathbf{X}(L,t)\cdot\ddot{\mathbf{X}}(L,t)\,dt\\
&\quad+\int_{t_0}^{t^*}\int_0^l B\,\delta\mathbf{X}''(s,t)\cdot\mathbf{X}''(s,t)\,ds\,dt-\int_{t_0}^{t^*}\int_0^L \gamma\,\delta\mathbf{X}(s,t)\cdot\mathbf{g}\,ds\,dt\\
&\quad-\int_{t_0}^{t^*} m\,\delta\mathbf{X}(L,t)\cdot\mathbf{g}\,dt+\int_{t_0}^{t^*}\int_0^{L-\ell(t)}\delta\mathbf{X}(s,t)\cdot\mathbf{n}(t)\,\lambda(s,t)\,ds\,dt\\
&\quad+\int_{t_0}^{t^*}\delta\mathbf{X}(l-\ell(t),t)\cdot\mathbf{R}(t)\,dt+\int_{t_0}^{t^*}\delta\mathbf{X}'(L-\ell(t),t)\cdot\mathbf{n}(t)\,M(t)\,dt\\
&+\int_{t_0}^{t^*}\int_0^L 2\,\delta\mathbf{X}'(s,t)\cdot\mathbf{X}'(s,t)\,N(s,t)\,ds\,dt+\int_{t_0}^{t^*} c(t)\,\delta\mathbf{X}(L,t)\cdot\dot{\mathbf{X}}(L,t)\,dt\\
&\qquad+\int_{t_0}^{t^*}\mu\,\delta\mathbf{X}(L-\ell(t),t)\cdot\mathbf{X}'(L-\ell(t),t)|\mathbf{n}\cdot\mathbf{R}(t)|\\
&\qquad\quad\operatorname{sgn}\left[\mathbf{X}'(L-\ell(t),t)\cdot(\dot{\mathbf{X}}(L-\ell(t),t)-\dot{\mathbf{U}}_{sl}(t))\right]\,dt=0,
\end{aligned}$$

$$\int_{t_0}^{t^*}\int_0^{L-\ell(t)}\delta\lambda(s,t)\,\mathbf{n}(t)\cdot[\mathbf{X}(s,t)-\mathbf{U}_{sl}(t)]\,ds\,dt=0,$$

$$\int_{t_0}^{t^*}\delta\mathbf{R}\cdot[\mathbf{X}(L-\ell(t),t)-\mathbf{U}_{sl}(t)]\,dt=0,$$

$$\int_{t_0}^{t^*}\delta M\,\left[\mathbf{n}^T\mathbf{X}'(L-\ell(t),t)\right]dt=0,$$

$$\int_{t_0}^{t^*}\int_0^l \delta N(s,t)\,\left[(\mathbf{X}'(s,t))^2-1\right]ds\,dt=0,$$

$$\begin{aligned}
&\int_{t_0}^{t^*}\delta\ell\left\{\left[\frac{1}{2}B\,(\mathbf{X}''(s,t))^2\right]_{s=L-\ell^-(t)}^{s=L-\ell^+(t)}\right.\\
&\quad\left.-\mathbf{X}'(L-\ell(t),t)\cdot\mathbf{R}(t)-\mathbf{n}(t)\cdot\mathbf{X}''(L-\ell^+(t),t)\,M(t)\right\}dt=0.
\end{aligned}\tag{181}$$

Equation $(181)_1$ describes the dynamics of the constrained rod, where the last two terms are the viscous and dry-friction dissipation forces respectively, while equations $(181)_2$-$(181)_5$ impose the constraints. Equation

$(181)_6$ provides an interface condition at the sliding sleeve exit, that coincides with the configurational force obtained with the elastica model (165). Due to this condition, there exists a discontinuity in the internal action field N and as a result any spatial reconstruction of N should take into account this discontinuity. In Eqs. (181) the dissipation terms have been added as implicitly defined forces to the finite element framework.

4.4 NONLINEAR DYNAMICS OF THE OSCILLATING SLIDING SLEEVE - ROD - MASS SYSTEM

In this section the dynamics of the oscillating sliding-sleeve system are presented. The oscillation of the sliding sleeve is considered to be in the horizontal direction only and to assume a sinusoidal form given by

$$\begin{aligned} U_{sl}(t) &= u_g \cos(\omega t), \\ V_{sl}(t) &= 0, \end{aligned} \tag{182}$$

where u_g and ω are respectively the amplitude and the angular frequency of the sliding sleeve motion.

A dimensional analysis of the system shows that, apart from the dissipative terms, the oscillating sliding sleeve system can be described through three non-dimensional quantities

$$\Omega = \omega \sqrt{\frac{\ell_0}{g}}, \quad p = \frac{mg\ell_0^2}{B}, \quad U = \frac{u_g}{\ell_0}, \tag{183}$$

where ℓ_0 is chosen to be the external length at the initial time $\ell_0 = \ell(0)$.

Intuitively, it is expected that the rod is injected if the excitation frequency or amplitude approaches zero or if the value of the mass m is very large. Oppositely, the rod is not injected in the case that the frequency or the amplitude is large or the mass m is small. This limit behaviour is summarized in Table 2.

Table 2: Limit behaviour of the oscillating sleeve system.

final injection	no final injection
$\Omega \to 0$	$\Omega \to \infty$
$U \to 0$	$U \to \infty$
$p \to \infty$	$p \to 0$

4.4.1 *Dynamics from initial rest conditions*

Among the possible initial conditions for the lumped mass, initial rest conditions are considered under two scenarios, absolute rest and relative rest. In both scenarios, the mass is initially held at a fixed height, the motion of the sliding sleeve starts at $t = 0$, and the mass is subsequently released at a time t_r.

The initial absolute rest condition is represented by

$$X(L, t_r) = \dot{X}(L, t_r) = Y(L, t_r) = \dot{Y}(L, t_r) = 0, \tag{184}$$

which are equivalent to the following initial relative coordinate values

$$\begin{aligned} &x(L, t_r) = -u_g \cos(\omega t_r), && \dot{x}(L, t_r) = u_g \, \omega \sin(\omega t_r), \\ &y(L, t_r) = 0, && \dot{y}(L, t_r) = 0, \end{aligned} \tag{185}$$

The final state of the rod evaluated from the numerical integration of Eq. (181) is reported in Fig. 20 (left) for dissipation parameters $\zeta = 0.025$ and $\mu = 0.15$, and for different values of t_r (given as a fraction of the period on the sliding-sleeve motion $T = 1/f_{ex}$), showing no clear division in separated regions between the different behaviours. The system results sensitive to the timing (phase shifting) between the mass release and the sinusoidal motion of the sleeve.

Differently, the assumption of an initial relative rest condition, defined by

$$x(L, t_r) = \dot{x}(L, t_r) = y(L, t_r) = \dot{y}(L, t_r) = 0, \tag{186}$$

leads to a more clear distinction between the different behaviours, Fig. 20 (right). In this case, although the final state is still dependent on the timing t_r (phase shifting) of the mass release, the uncertainty region is well defined. It should be noted that there exist small islands of one behaviour within the main region of the other, however their size is strongly affected by the dissipation parameters and are expected to disappear for large enough values of dissipation.

With reference to initial relative rest conditions, two transition surfaces are found within the 3D space defined by the dimensionless parameters Ω, p and U as those separating datasets into regions related to one among the three possible final states: final injection, final ejection, and an unexpected quasi-periodic motion. The transition surfaces are shown in Fig. 21 for a null release time $t_0 = 0$ and dissipation parameters $\zeta = 0.025$

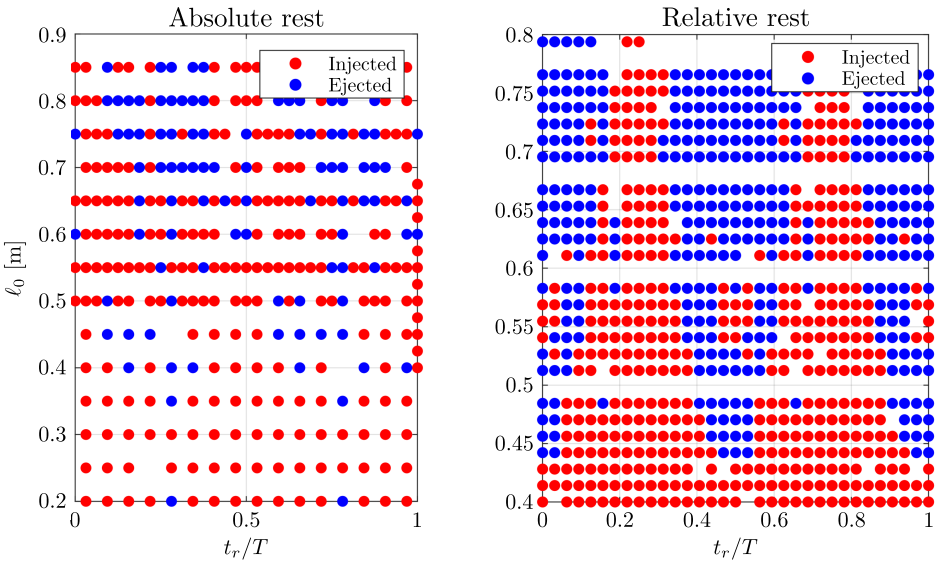

Figure 20: Comparison between the effects of the absolute (left) and relative (right) rest initial conditions for dissipation parameters $\zeta = 0.025$ and $\mu = 0.15$. The injection or ejection of the rod is shown as a function of the release time t_r (as a fraction of the excitation period T) and the initial external length of the rod ℓ_0. The behaviour of the system subject to the absolute rest initial conditions shows no clear pattern, while in the relative rest case a sinusoidal pattern emerges.

and $\mu = 0$. The red surface divides the region of complete injection from that of quasi-periodic motion, while the blue surface divides the region of quasi-periodic motion from that of complete ejection. It is also interesting to note that some portion of the two transition surfaces is coincident, implying therefore that a transition between final injection and final ejection occurs for a range of dimensionless parameters without any display of quasi-periodic motion (confirming the injection/ejection transition shown in Fig. 20, right). Therefore, through the transverse oscillation of the sliding sleeve, the system may gain a third attractor at finite length $\ell = \ell_m \neq 0$, in addition to the two trivial attractors corresponding to $\ell = 0$ and $\ell \to \infty$. To further substantiate the transition between these three behaviours, the time-series of the external length $\ell(t)$ for a null release time $t_0 = 0$ are shown in Fig. 22 for varying values of p. The three distinct behaviours can be appreciated as the system transitions from final ejection to a quasi-periodic motion to final injection as the value of p increases. Also, the inclusion of dry friction on the theoretical model has a mitigating effect on the ejection of the rod; see Fig. 22 (lower part).

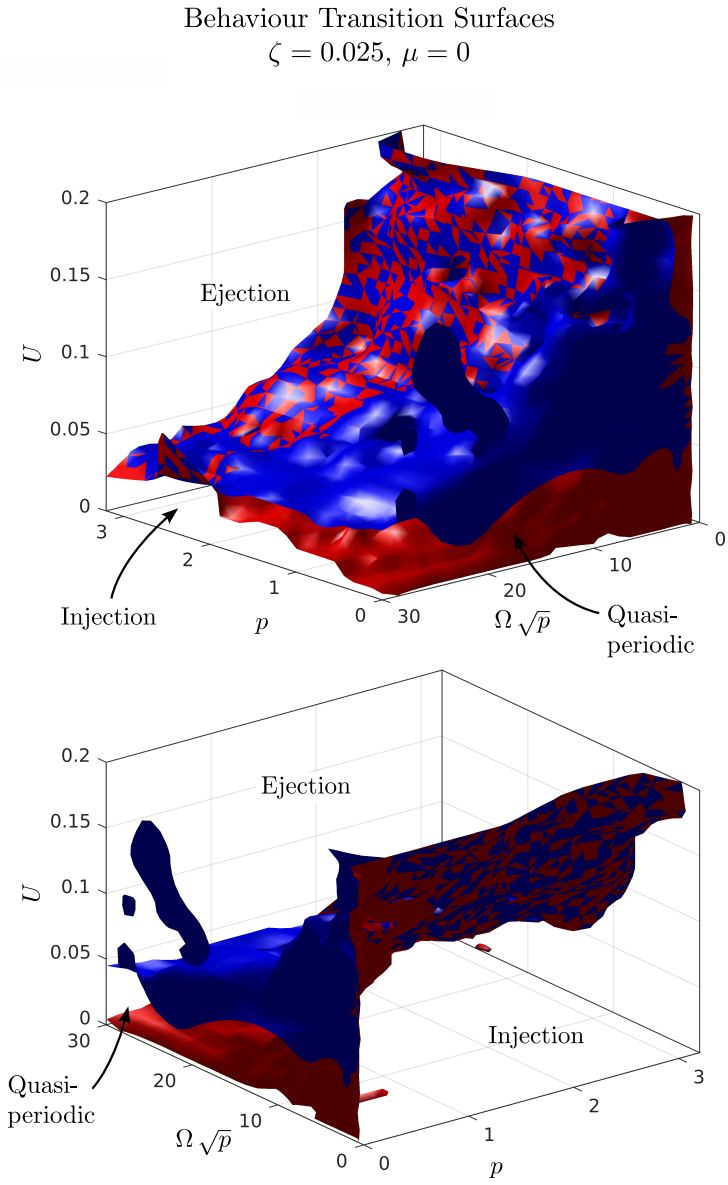

Figure 21: Transition surfaces dividing the three behaviour regions. Red surface defines the change from injection to quasi-periodic motion. Blue surface defines the change from quasi-periodic motion to ejection. Where the two surfaces coincide, there is a transition from injection to ejection without an intermediate quasi-periodic state (as shown in Fig. 20, right). The surfaces are representative for a null release time $t_r = 0$ and dissipation parameters $\zeta = 0.025$ and $\mu = 0$.

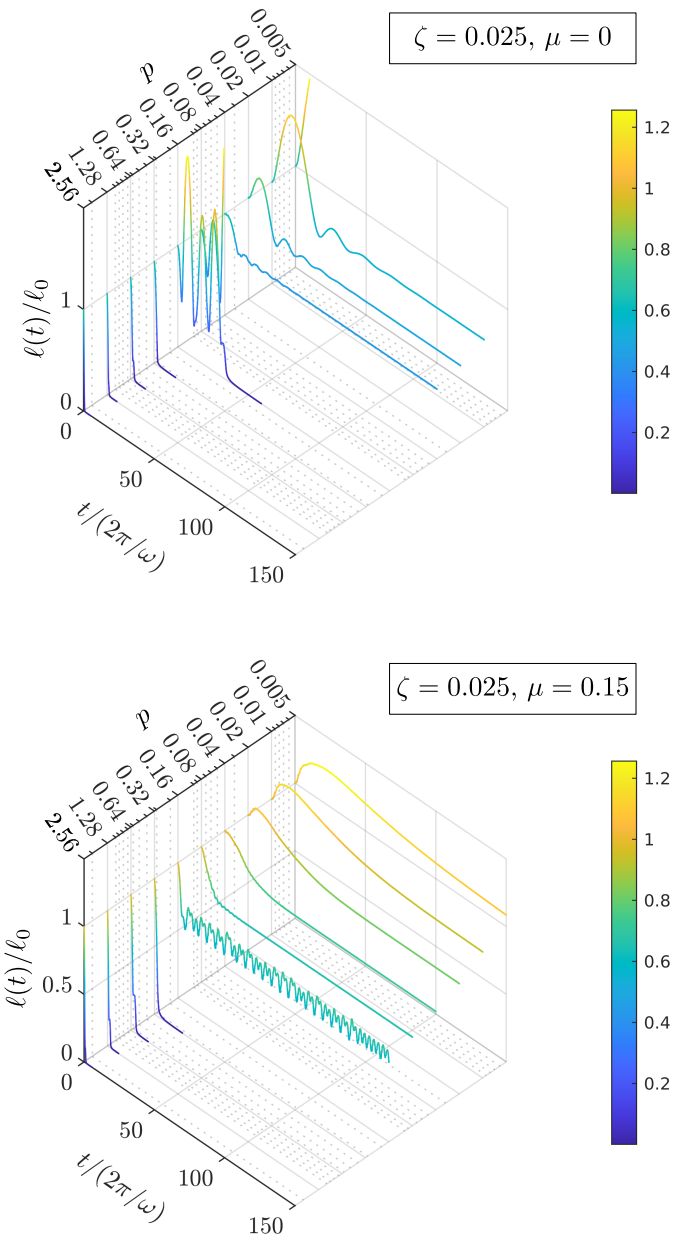

Figure 22: Time evolution of $\ell(t)$ with varying p and fixed dimensionless amplitude $U = 0.04$ and frequency $\Omega = 5$, for a null release time $t_r = 0$. Top, the system with only viscous damping $\zeta = 0.025$ and no dry friction $\mu = 0$. Bottom, system with viscous damping $\zeta = 0.025$ and dry friction $\mu = 0.15$.

4.4.2 *The search for an analytical periodic solution through asymptotic expansion*

In order to obtain an analytical prediction for the mass motion, the differential system (175) governing the end's relative position x_L, y_L is approximated through its expansion by taking $\beta(t) \approx \pi/2$ and small end rotation $\theta_L(t) \ll 1$,

$$\begin{aligned} &m\,\ddot{x}_L(t) + \frac{3B}{\ell^3(t)} x_L(t) = m\,\omega^2\,u_g\,\cos(\omega t), \\ &m\,(g + \ddot{y}_L(t)) = \frac{M^2(t)}{2B}, \end{aligned} \tag{187}$$

where, under small rotation, the following approximations hold

$$\begin{aligned} &M(t) = 2B\theta_L(t)/\ell(t), \\ &x_L(t) = \frac{2}{3}\ell(t)\,\theta_L(t), \\ &y_L(t) = \ell(t)\left[1 - \frac{4}{15}\theta_L^2(t)\right]. \end{aligned} \tag{188}$$

Introducing ℓ_m as the reference external rod's length during the periodic motion, a dimensionless time τ_m can be defined as

$$\tau_m = t\sqrt{\frac{g}{\ell_m}}, \tag{189}$$

as well as other dimensionless quantities as

$$\begin{aligned} &\tau_m = t\sqrt{\frac{g}{\ell_m}}, \quad \Omega_m = \omega\sqrt{\frac{\ell_m}{g}}, \quad p_m = \frac{mg\ell_m^2}{B}, \quad U_m = \frac{u_g}{\ell_m}, \\ &\lambda(\tau_m) = \frac{\ell(t)}{\ell_m}, \quad \xi(\tau_m) = \frac{x_L(t)}{\ell_m}, \quad \eta(\tau_m) = \frac{y_L(t)}{\ell_m}, \end{aligned} \tag{190}$$

and the approximated equations of motion (187) can be expressed in a non-dimensional form as

$$\begin{aligned} &\overset{**}{\xi}(\tau_m) + \frac{3}{p_m\lambda^3(\tau_m)}\xi(\tau_m) = \Omega_m^2 U_m \cos(\Omega_m\tau_m), \\ &1 + \overset{**}{\eta}(\tau_m) - \frac{2\theta_L^2(\tau_m)}{p_m\lambda^2(\tau_m)} = 0, \end{aligned} \tag{191}$$

where the symbol $\overset{*}{\cdot}$ stands for the derivative of the relevant quantity with respect to dimensionless time τ_m.

By assuming the unknown variations in time of the rotation $\theta(t)$ and in length $\lambda(t)$ as the following periodic functions of the small amplitudes ε_θ and ε_ℓ as

$$\theta_L(\tau_m) = \varepsilon_\theta \cos(\Omega_m \tau_m), \qquad \lambda(\tau_m) = 1 - \varepsilon_\ell \cos(2\Omega_m \tau_m), \tag{192}$$

the dimensionless approximated equations of motion (191) truncated at the smallest orders reduce to

$$\begin{aligned} &2\left[6\varepsilon_\theta - p_m\Omega_m^2(3U_m + 2\varepsilon_\theta)\right]\cos(\Omega_m\tau_m) \\ &\quad -3\varepsilon_\ell\left[2\varepsilon_\theta - p_m\Omega_m^2(3U_m + 8\varepsilon_\theta)\right]\cos(3\Omega_m\tau_m) \approx 0, \\ &15\left[p_m - \varepsilon_\theta^2 + \frac{p_m\varepsilon_\ell^2(1-8\Omega_m^2)}{2}\right] \\ &\quad -\left[15\varepsilon_\theta^2 + 30p_m\varepsilon_\ell - p_m\Omega_m^2\left(8\varepsilon_\theta^2 + 60\varepsilon_\ell\right)\right]\cos(2\Omega_m\tau_m) \approx 0. \end{aligned} \tag{193}$$

The annihilation of the time-independent term in Eqn. $(193)_2$ leads to

$$p_m = \frac{\varepsilon_\theta^2}{1 - 4\varepsilon_\ell^2\Omega_m^2}, \tag{194}$$

or, equivalently

$$\varepsilon_\theta = \sqrt{p_m}\sqrt{1 - 4\varepsilon_\ell^2\Omega_m^2} \qquad \text{or} \qquad \varepsilon_\theta = -\sqrt{p_m}\sqrt{1 - 4\varepsilon_\ell^2\Omega_m^2}, \tag{195}$$

disclosing the presence of twin solutions, one in phase ($\varepsilon_\theta U_m > 0$) and another in counter-phase ($\varepsilon_\theta U_m < 0$) with the ground motion.

Assuming that $\varepsilon_\ell\Omega_m \ll 1$, the previous equations reduce to

$$p_m = \varepsilon_\theta^2 \qquad \to \qquad \varepsilon_\theta = \sqrt{p_m} \qquad \text{or} \qquad \varepsilon_\theta = -\sqrt{p_m}, \tag{196}$$

which in turn simplifies Eqns. (193) as

$$\begin{aligned} &\varepsilon_\theta\left[6 - \varepsilon_\theta\Omega_m^2(3U_m + 2\varepsilon_\theta)\right]\cos(\Omega_m\tau_m) \\ &-3\varepsilon_\theta\varepsilon_\ell\left[2 - \varepsilon_\theta\Omega_m^2(3U_m + 8\varepsilon_\theta)\right]\cos(3\Omega_m\tau_m) \approx 0, \\ &-\varepsilon_\theta^2\left[15 + 30\varepsilon_\ell - \Omega_m^2\left(8\varepsilon_\theta^2 + 60\varepsilon_\ell\right)\right]\cos(2\Omega_m\tau_m) \approx 0, \end{aligned} \tag{197}$$

which show that the approximated equations of motion are satisfied at the smallest order when

$$\begin{aligned} &6 - \varepsilon_\theta\Omega_m^2(3U_m + 2\varepsilon_\theta) \approx 0, \\ &15 - \Omega_m^2\left(8\varepsilon_\theta^2 + 60\varepsilon_\ell\right) \approx 0. \end{aligned} \tag{198}$$

Equations (198) are now solved by considering three main cases defining the asymptotic order between the different involved parameters.

Case $|\varepsilon_\ell| \gg |\varepsilon_\theta|^2$

In this case the dimensionless amplitude and frequency have the following asymptotic order

$$|U_m| \gg |\varepsilon_\theta|, \qquad |\Omega_m| \approx \frac{1}{\sqrt{|\varepsilon_\ell|}}, \tag{199}$$

implying the following relations for $p_m \to 0$ and finite values of $\sqrt{p_m}\,\Omega_m^2$

$$U_m = \pm\frac{2}{\sqrt{p_m}\Omega_m^2}, \qquad \epsilon_\ell = \frac{1}{4\sqrt{p_m}\Omega_m^2}\sqrt{p_m}, \tag{200}$$

which can be rewritten in the dimensional terms as

$$l_m = \pm\frac{2}{\omega^2 u_g}\sqrt{\frac{B}{m}}, \qquad \epsilon_\ell = \pm\frac{u_g}{8}\sqrt{\frac{mg}{B}}, \tag{201}$$

revealing a gravity-insensitive average length ℓ_m.

Case $|\varepsilon_\ell| \ll |\varepsilon_\theta|^2$

In this case ε_ℓ remains undefined and the dimensionless amplitude and frequency have the following asymptotic order

$$|U_m| \approx |\varepsilon_\theta|, \qquad |\Omega_m| \approx \frac{1}{|\varepsilon_\theta|}, \tag{202}$$

implying the solutions valid for $p_m \to 0$ and finite values of $p_m\,\Omega_m^2$

$$U_m = \pm\frac{2\sqrt{p_m}}{5}, \qquad \Omega_m = \frac{1}{2}\sqrt{\frac{15}{2p_m}}, \tag{203}$$

and equivalent to

$$\ell_m = \frac{1}{2}\sqrt[3]{\frac{15B}{m\omega^2}}, \qquad u_g = \frac{1}{2}\sqrt[3]{\frac{9}{5\omega^4}}\sqrt[6]{\frac{B}{m}}\sqrt{g}. \tag{204}$$

Case $|\varepsilon_\ell| \approx |\varepsilon_\theta|^2$

In this case the dimensionless amplitude and frequency have the following asymptotic order

$$|U_m| \approx |\varepsilon_\theta|, \qquad |\Omega_m| \approx \frac{1}{|\varepsilon_\theta|}, \tag{205}$$

implying the solutions valid for $p_m \to 0$ and finite values of $p_m\,\Omega_m^2$

$$U_m = \pm\frac{2\,(3-p_m\,\Omega_m^2)}{3\,p_m\,\Omega_m^2}\,\sqrt{p_m}, \qquad \varepsilon_\ell = \frac{15-8\,p_m\,\Omega_m^2}{60 p_m\,\Omega_m^2}p_m. \tag{206}$$

Substituting the non-dimensional quantities with their dimensional counterparts in Eqn. (206)$_1$, the following equation is obtained

$$2g\left(\frac{\ell_m^3 m\omega^2}{B}-3\right)\pm 3\ell_m u_g\omega^2\sqrt{\frac{m\,g}{B}}=0. \tag{207}$$

By setting

$$\begin{aligned}\sigma &= \frac{u_g}{3\sqrt{g}}\sqrt[3]{\frac{3}{2}}\sqrt[6]{\frac{m\omega^8}{B}} = \frac{1}{3}\sqrt[3]{\frac{3}{2}}U_m\sqrt[6]{p_m}\sqrt[3]{\Omega_m^4},\\ \rho &= \ell_m\sqrt[3]{\frac{2}{3}}\sqrt[3]{\frac{m\omega^2}{B}} = \sqrt[3]{\frac{2}{3}}\sqrt[3]{p_m\Omega_m^2} > 0,\end{aligned} \tag{208}$$

both without any restriction in their magnitude within the present analysis, Eq. (207) can be rewritten as the two following cubic equations

$$\rho^3 - 2 \pm 3\,\rho\,\sigma = 0, \tag{209}$$

each one having only real and positive solution given by

$$\rho^{\pm} = \frac{\sqrt[3]{\left(1+\sqrt{1\pm\sigma^3}\right)^2}\mp\sigma}{\sqrt[3]{1+\sqrt{1\pm\sigma^3}}}, \tag{210}$$

reported as dimensionless average length ℓ_m^+ and ℓ_m^- curves as functions of the dimensionless ground displacement amplitude u_g in Fig. 23. In the case when $\sigma = u_g = 0$ the two average lengths become coincident, $\ell_m^+ = \ell_m^- = \ell_m$, and corresponding to that of the clamped rod when the excitation frequency coincides with its natural frequency, $\omega = \sqrt{3B/(m\ell_m^3)}$. For the case that $U_{sl}(t)$ and $\theta_L(t)$ are in phase, an inversion of the phase of $\ell(t)$ happens at the value $\rho = \sqrt[3]{5/4}$. The twin solutions $\ell^{\pm}(t) = \ell_m^{\pm}[1-\epsilon_\ell^{\pm}\cos(2\omega t)]$ and $\theta_L^{\pm}(t) = \epsilon_\theta^{\pm}\cos(\omega t)$ are shown in Fig. 24 for the parameters $m = 0.2$ kg, $B = 1.5$ Nm^2, $\omega = 10\pi$ rad/sec, and $u_g = 0.005$ m.

4.5 FROM PERIODIC TO QUASI-PERIODIC RESPONSE

The numerical integration of the (non-approximated) equations of motion (175) reveals that, when it has no final injection or ejection, the system may

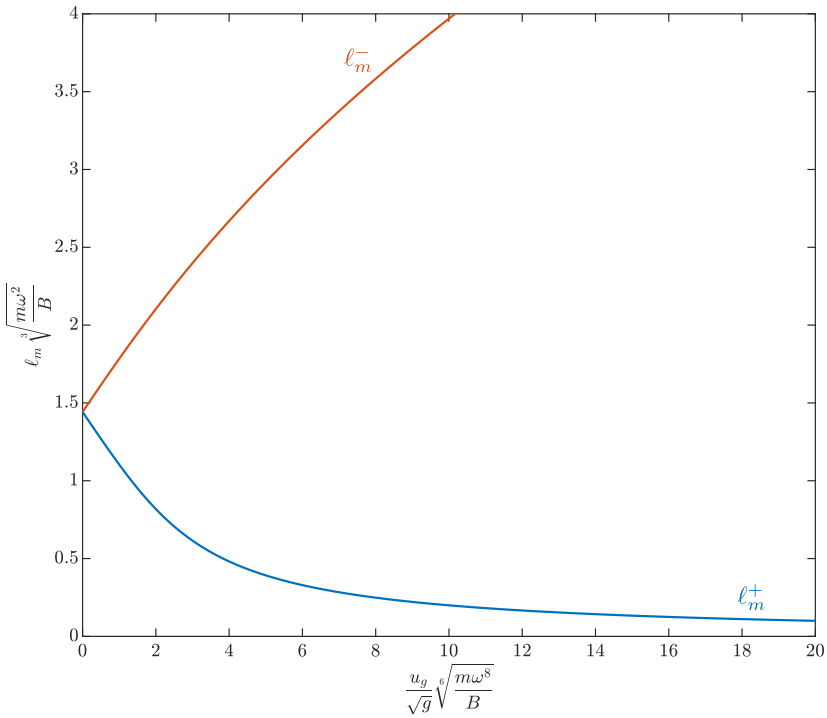

Figure 23: Dimensionless average lengths ℓ_m versus dimensionless ground displacement amplitude u_g (solid lines). The two average lengths convergence to the same value in the limit of vanishing ground motion amplitude u_g, $\ell_m = \sqrt[3]{3B/(m\omega^2)}$.

display a periodic or quasi-periodic response. This is shown in Figs. 25 and 26 where the transition from a periodic to a quasi-periodic behaviour occurs at increasing the sliding sleeve frequency $f_{ex} = \omega/(2\pi)$ in the presence of a small viscous dissipation ($\zeta = 0.005$, $\mu = 0$). In particular, the transition from periodic ($f_{ex} = 2\text{Hz}$) to quasi-periodic ($f_{ex} = \{3.2, 3.5\}\text{Hz}$) response can be appreciated through the phase portraits projections and the Poincaré sections (upper part) and the Fourier Transform (lower part) of the external length $\ell(t)$ (Fig. 25) and the rotation $\theta_L(t)$ (Fig. 26) in time. The results are related to time far after the transient effects are dissipated and the Poincaré sections are shown for two shifted timings, $t = 2k\pi/\omega$ and $t = (2k+1)\pi/\omega$ for the rotation and $t = 2k\pi/\omega$ and $t = (2k+0.5)\pi/\omega$ for the external length, with $k \in \mathbb{N}$ within the relevant time interval. Due to nonlinearities inherent to the system vibration, the periodic solution (192) becomes no longer representative of the sys-

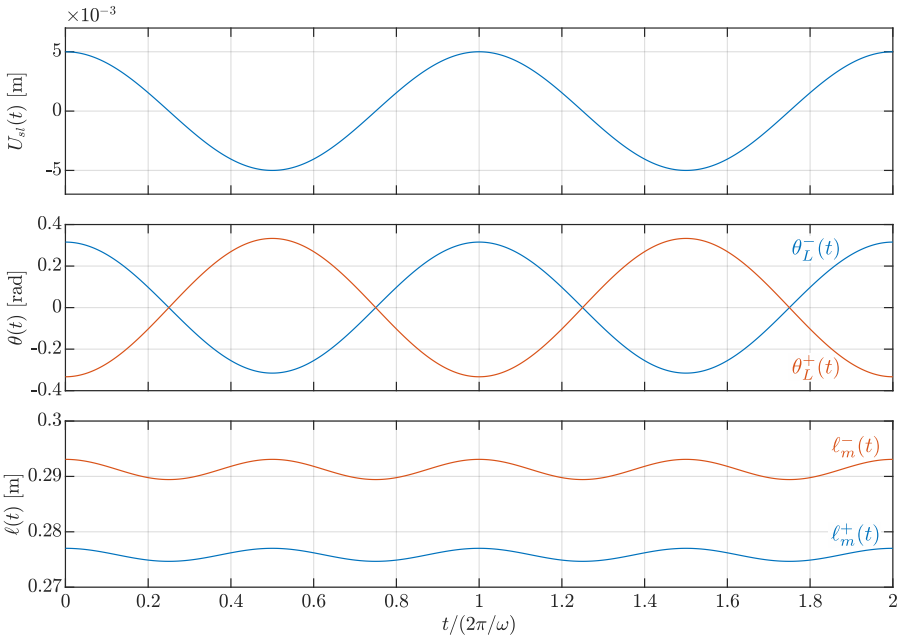

Figure 24: Time-series of the twin periodic solutions $\ell^{\pm}(t) = \ell_m^{\pm}[1 - \epsilon_\ell^{\pm}\cos(2\omega t)]$ and $\theta^{\pm}(t) = \epsilon_\theta^{\pm}\cos(\omega t)$ for parameters $m = 0.2$ kg, $B = 1.5$ Nm^2, $\omega = 10\pi$ rad/sec, and $u_g = 0.005$ m. $U_{sl}(t)$ and $\theta(t)$ can be in phase or differ by a phase of π, giving as a result a different value for ℓ_m but the same amplitude ε_ℓ.

tem response at increasing constraint frequency, showing a quasi-periodic motion described by multiple frequencies that are not rational multiples of the excitation frequency.

4.6 EXPERIMENTAL VALIDATION

The present theoretical findings are validated through the experimental setup shown in Fig. 27, manufactured and tested at the Instabilities Laboratory of the University of Trento. The sliding sleeve is realized through two parallel arrays of rollers kept at a fixed distance by means of two acrylic panels. More specifically, the distance between the roller arrays is set to have the constrained part of the rod straight but still freely sliding. The sliding sleeve constraint device is attached to an ElectroForce Linear motor 3300 Series II by Bose and screwed on a rail system that ensures the motion along one direction only. Above the sliding sleeve constraint, an adjustable height platform mounting and an electromagnet are installed

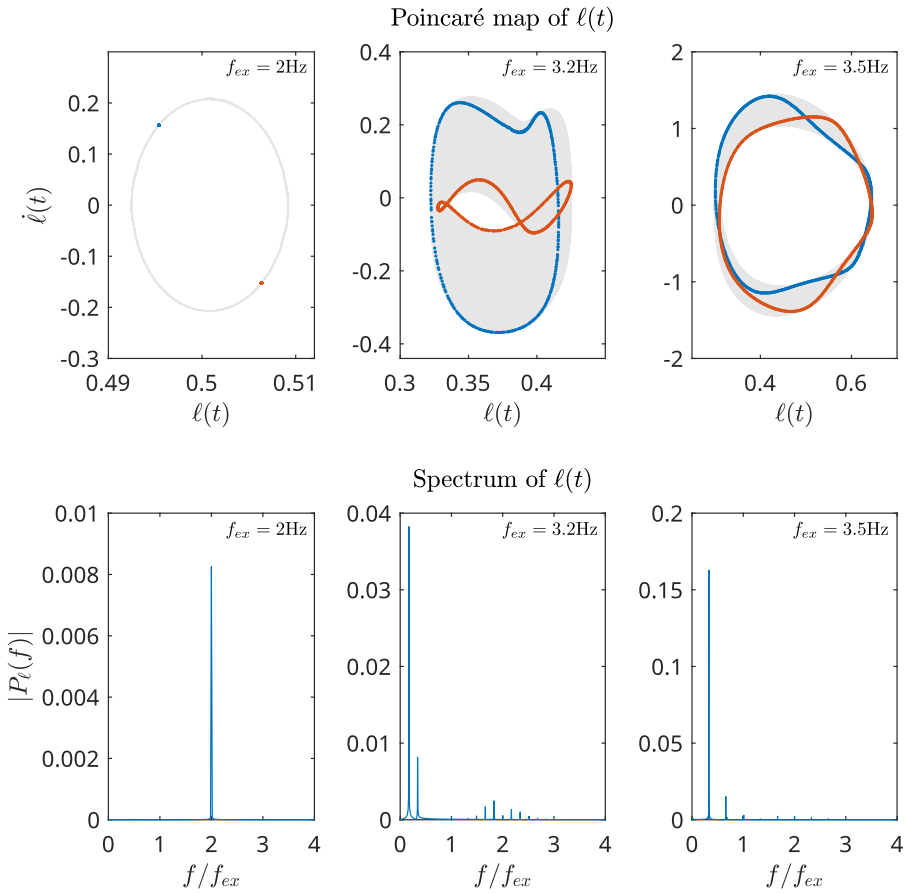

Figure 25: Projections of the phase portraits and the Poincare sections for two half-period shifted phases (upper part) and frequency spectrum of the response (lower part) for a system with $m = 130$gr, $u_g = 5$mm, and for dissipation parameters $\zeta = 0.005$, $\mu = 0$. Three cases are shown for $\ell(t)$: (Left) Periodic motion for excitation frequency $f_{ex} = 2$Hz, Quasi-periodic motion for (Centre) $f_{ex} = 3.2$Hz and (Right) $f_{ex} = 3.5$Hz.

in order to release the rod from a relative rest condition and specific external length. To this purpose, the mass at the tip of the rod is completed by a circular steel plate fitting the socket embedding the electromagnet.

The rod used is made from a carbon-fiber sheet and its properties are summarized in Table 3, and two values of the mass m are selected, $m = \{130, 303\}$gr. The range of excitation frequency f_{ex} and the excitation amplitude u_g that are allowed by the experimental setup are $f_{ex} \in [0, 20]$ Hz and $u_g \in [0, 10]$ mm. It should be noted that the mass of the rod (γL) is a significant fraction of the mass m considered in the experiments and as

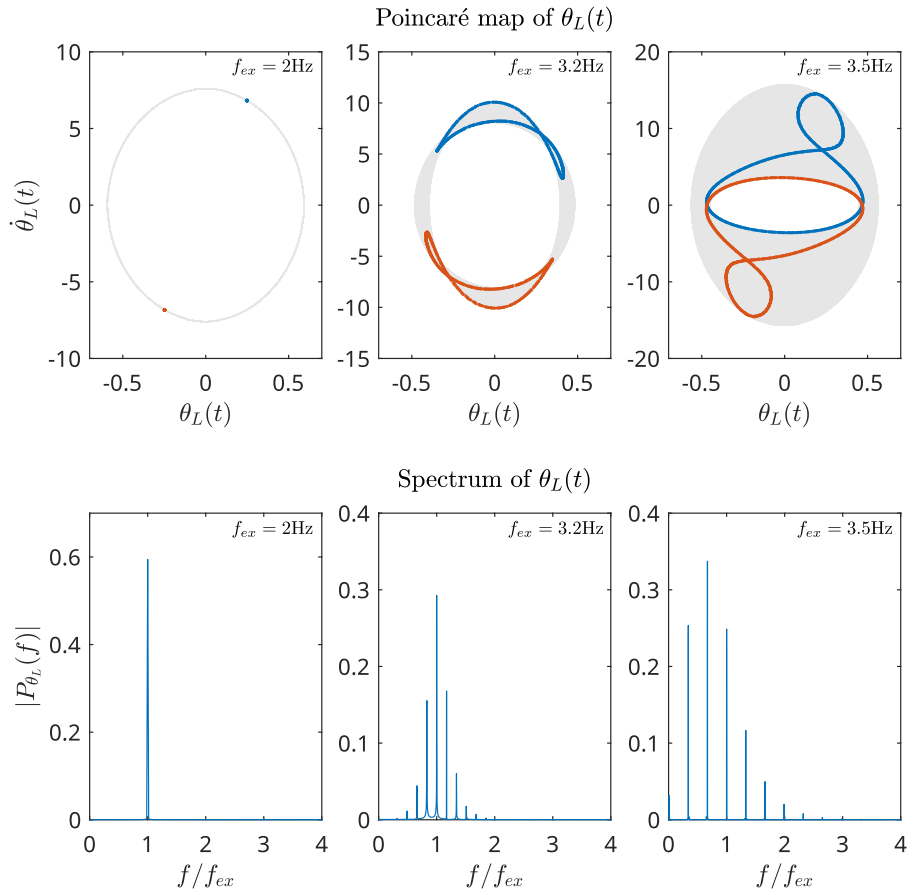

Figure 26: As for Fig. 25 but for $\theta_L(t)$.

a result in the analytical results reported along the experimental data an equivalent mass is used $m_{eq} = m + (\gamma L)$.

Table 3: Properties of the carbon-fiber rod used in the experiments.

	Property	Value
Carbon-fiber rod	Thickness	2.04 mm
	Width	25.33 mm
	Length L	800 mm
	Bending stiffness B	1.4363 Nm^2
	Mass (γL)	67 gr

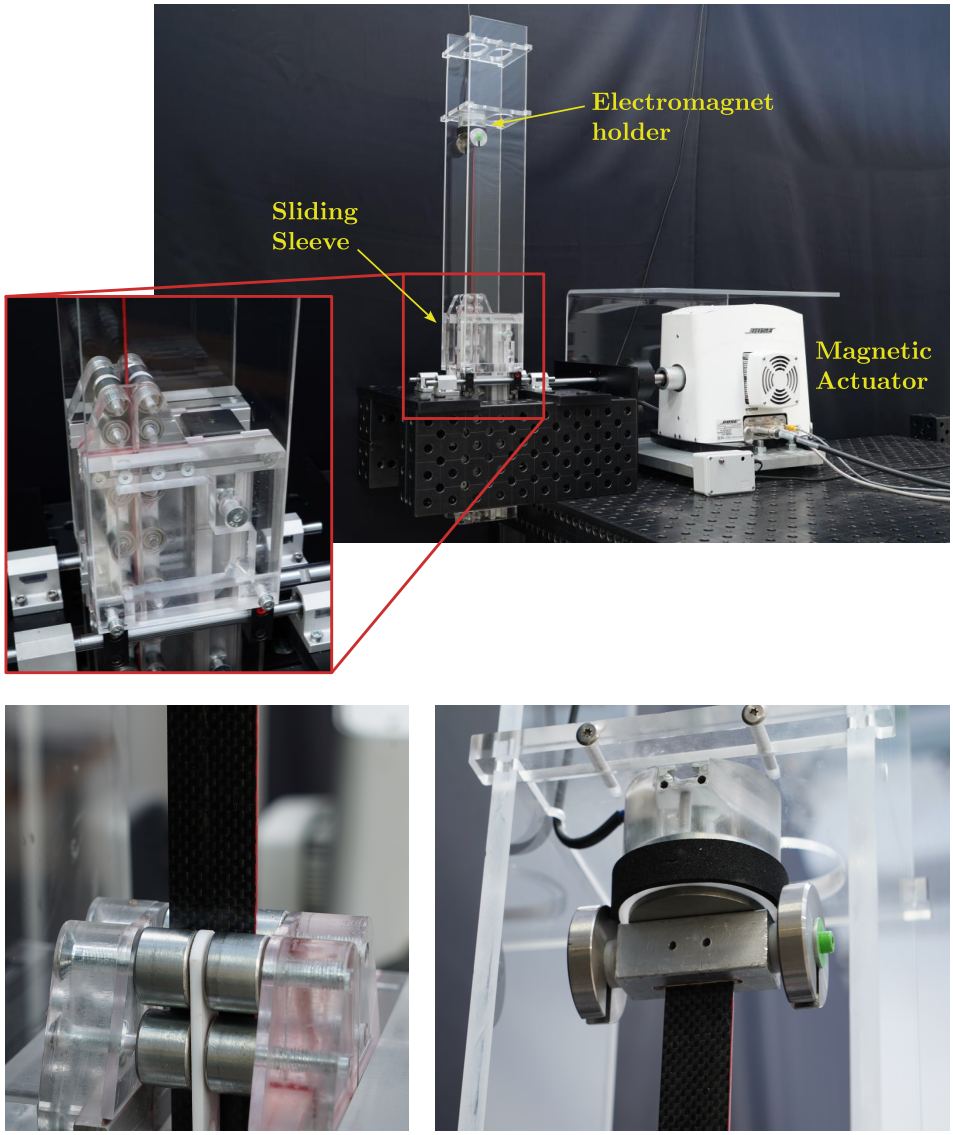

Figure 27: Experimental setup of the oscillating sliding-sleeve system realized in the Instabilities Laboratory of the University of Trento. Top part: general arrangement of the experimental setup. Lower part: details of the sliding sleeve exit (lower left) and the mass attachment at the tip of the rod (lower right).

The rod's dynamics is recorded during the experiments with a SONY PXW-FS5 and a SONY PXW-FS7 cameras, and the related videos are post-processed using a Matlab script in order to extract the time-histories of the mass relative coordinates $x_L(t)$ and $y_L(t)$ and the external length $\ell(t)$.

Although an accurate modelling of the dissipative forces is fundamental for the quantitative prediction of the motion, this task is made difficult by the high level of complexity and uncertainties related to the several dissipation sources associated with the sliding sleeve constraint. To this purpose, dissipative phenomena connected to the sliding sleeve have been limited as much as possible through the application of oil lubricant to the rod, in addition to using rollers with ball bearings.

Two types of experiments have been performed,

- *rod's release from relative rest conditions;*
- *monotonic variation in the amplitude or frequency of the sliding sleeve oscillation during the quasi-periodic motion of the rod.*

In the following, these types of experiments and the related results are separately described.

4.6.1 *Rod's release from relative rest conditions*

Experiments of releasing the rod from a relative rest condition during the harmonic oscillation of the sliding sleeve are performed to reveal the corresponding final state of the rod (quasi-periodic motion, final injection or ejection) with varying the release time. The strong influence of the release time on the final state is shown in Figs. 28 and 29 where a mass $m = 303$ gr is attached to a rod of initial length $\ell_0 = 45$ cm constrained by an oscillating sliding sleeve with amplitude $u_g = 10$ and frequency $f_{ex} = 10$ Hz is released at $t_r = 0.07\,T$ and $t_r = 0.71\,T$, where T is the period of the oscillation of the sliding-sleeve. In particular, the time-histories of the experimentally measured absolute mass coordinates X_L and Y_L are reported in Fig. 28 while the experimental mass trajectories, together with some deformed configuration, are reported in Fig. 29, showing the final quasi-periodic motion and the final injection for the rod's release at $t_r = 0.07\,T$ and $t_r = 0.71\,T$, respectively.

4.6.2 *Monotonic variation in the amplitude or frequency of the sliding sleeve oscillation*

After the stabilization of the rod's dynamics on a quasi-periodic motion, a monotonic variation in the amplitude or frequency of the harmonic sliding sleeve oscillation is performed in order to evaluate how the quasi-periodic motion changes and when it is lost, leading to injection of the rod.

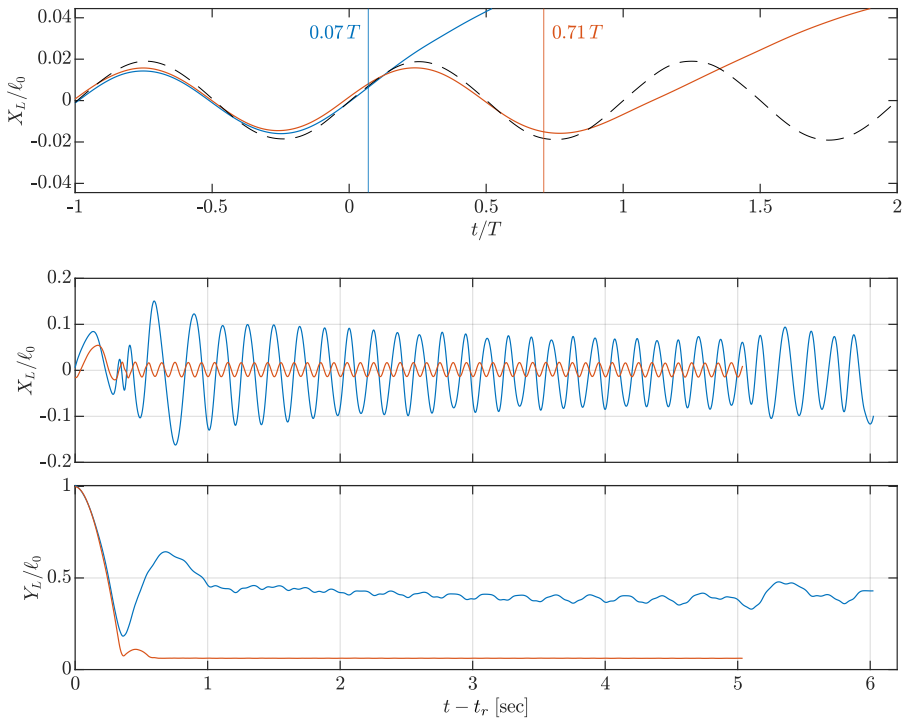

Figure 28: Time series of the experimentally measured trajectory of the mass m for $f_{ex} = 10$ Hz, $u_g = 10$ mm, $\ell_0 = 45$ cm, $m = 303$ gr, for two different release timings, $t_r = 0.07$ T and $t_r = 0.71$ T. (Top) Description of the release timing; the sliding sleeve motion is shown with a dashed line while the X component of the lumped mass trajectory for the two experiments close to the release time is shown along with the release time measurement. (Middle) The X components of the trajectories of the two experiments are shown, offset by the measured release time so that the release is matched. (Bottom) Same as middle part but for the Y components.

As both the excitation frequency f_{ex} and the amplitude u_g have an effect on the behaviour of the rod, two types of experiments were performed to independently assess the influence of the frequency and the amplitude of the input excitation, one for varying u_g while f_{ex} is constant, and one for varying f_{ex} while u_g is constant.

The performed experiments show that the behaviour of the system is significantly affected by the lubrication of the sliding sleeve. However, performing long experiment runs to assess the effect on the quasi-periodic motion of a monotonic variation in the frequency f_{ex} or in the amplitude u_g, the quality of the lubrication degrades and therefore the experimen-

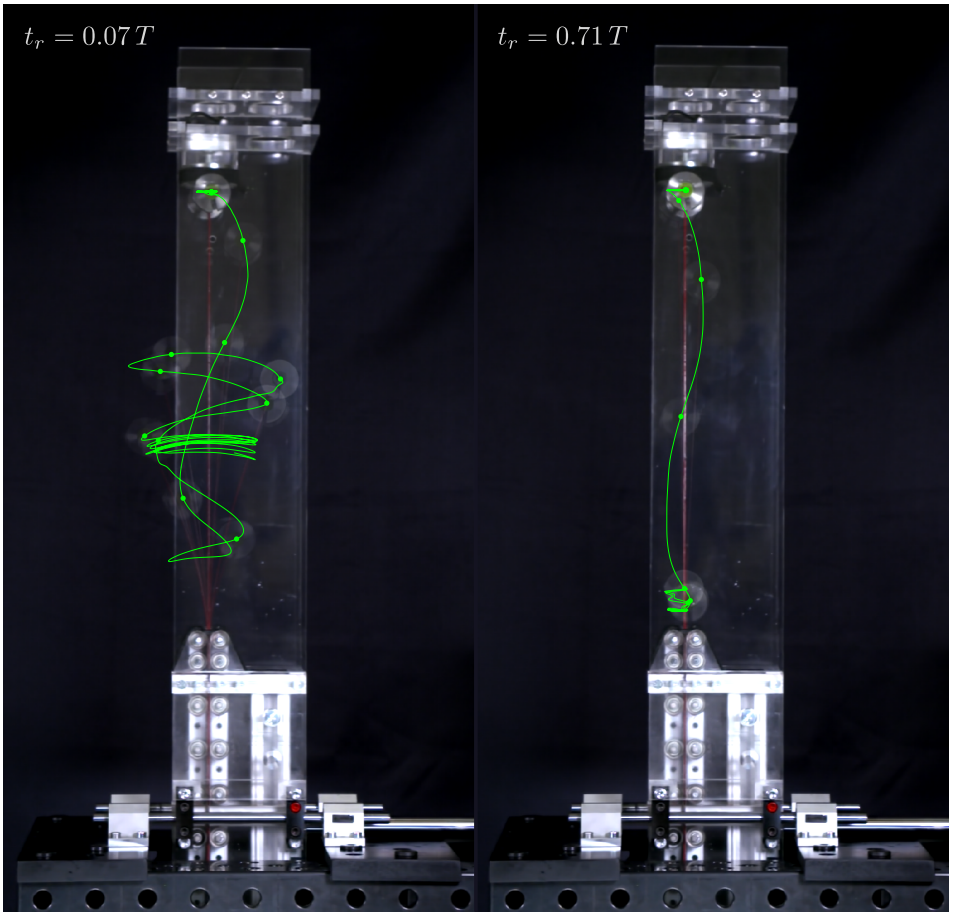

Figure 29: Composite image of the experimental setup during the experiments with relative rest initial conditions for $f_{ex} = 10$ Hz, $u_g = 10$ mm, $\ell_0 = 45$ cm, $m = 303$ gr, for two different release timings. (Left) $t_r = 0.07\,T$, (Right) $t_r = 0.71\,T$, where T is the period of the sliding-sleeve motion. The experimentally measured trajectory of the mass m is illustrated with green.

tal result is affected by this additional time-varying dissipation. As a result, the theoretical predictions can be validated through the experiments mainly qualitatively, because the loss of quasi-periodic motion can not exactly coincide.

In the amplitude-varying experiments, a value of the sliding oscillation frequency f_{ex} is fixed while the amplitude u_g is initially selected to be high enough to display a quasi-periodic motion. Next, the value of u_g is decreased at a rate of 0.1 mm every 10 seconds, until the rod is injected at a critical value $u_{g,cr}$. The value of u_g right before the injection is

recorded as the critical value $u_{g,cr}$ and the process is repeated for a range of frequencies. The critical amplitude is shown in Fig. 30, as a function of the excitation frequency $u_{g,cr}(f_{ex})$, for the two different masses that were used in the experimental campaign, $m = \{130, 303\}$ gr. At increasing values of the excitation frequency, the value of $u_{g,cr}$ is initially decreasing and then it increases until a local maximum, before a plateau region is reached. It should be noted that for a fixed value of u_g the critical curves can be interpreted also as defining the regions of frequencies f_{ex} for which the quasi-periodic motion cannot be sustained.

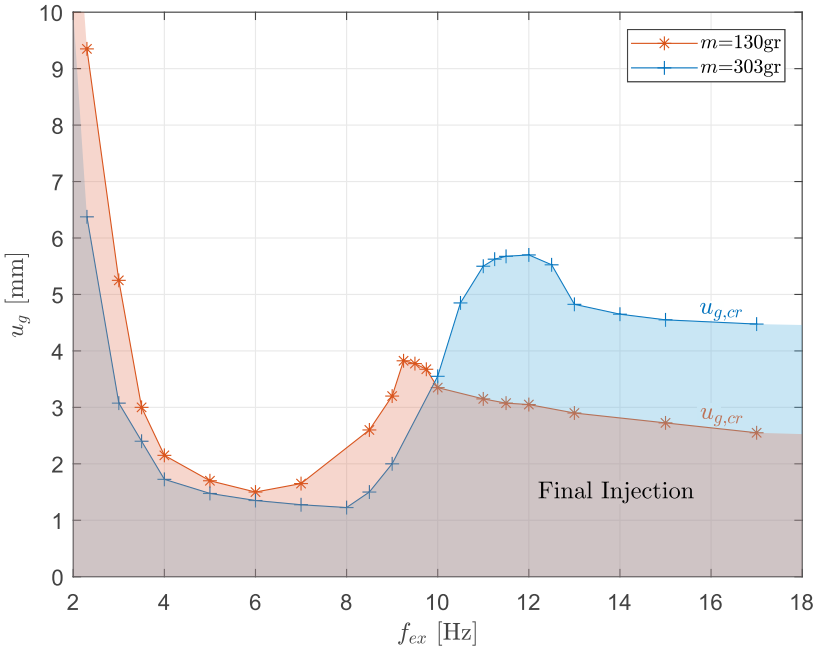

Figure 30: Experimental measure of the critical amplitude $u_{g,cr}$ for the rod's final injection as a function of the frequency f_{ex}. If the amplitude u_g becomes smaller than the critical value the rod is eventually injected. The red curve is for m=130gr and the blue curve for m=303gr.

In the frequency-varying experiments, a value of the amplitude u_g is fixed while the initial value for f_{ex} is selected in the range of values for which the quasi-periodic motion is predicted from Fig. 30. Then f_{ex} is either increased of decreased at a rate of 0.05 Hz every 15 seconds, in order to cover the entire range of frequencies allowed by the experimental setup. In more detail, data for fixed values of $u_g = \{3.5, 5\}$mm and $m = \{130, 303\}$gr were obtained for many starting values of f_{ex}. First, the

value for the starting frequency was selected to be $f_{ex} = 5$ Hz and two experiments were performed for each combination of u_g and m, one for increasing frequencies and one for decreasing. Then, the largest value of f_{ex} allowed by the experimental setup is selected for the starting value, and one experiment is performed for decreasing frequencies for every combination of u_g and m. In total three experiments for every u_g and m were performed and the results are shown in Fig. 31. The experimental results are shown in terms of the period-averaged external length ℓ_a, where the averaging period is the period of the sliding sleeve motion ($1/f_{ex}$), and depicted as a cloud of gray dots. Further, the analytically obtained average external lengths ℓ_m^+ and ℓ_m^- respectively for the in-phase and out-of-phase motions, as evaluated in the case $|\varepsilon_\ell| \approx |\varepsilon_\theta|^2$, Eq. (210), and the length of the resonant clamped-free rod ℓ_m^0 are shown. The analytically obtained lengths ℓ_m for the other ordering law ($|\varepsilon_\ell| \gg |\varepsilon_\theta|^2$ and $|\varepsilon_\ell| \ll |\varepsilon_\theta|^2$) are omitted as they are found not representative of the experimentally observed ordering between the rotation and length variation.

A major result derived during the experimental campaign is the confirmation of the prediction for the relation between the external length ℓ and the frequency of the input excitation; see Fig. 31. In a rough sense, the external length of the rod ℓ is shown to self-adjust (in an average sense) approximately within the range $[\ell_m^+, \ell_m^-]$, so that the rod mass system is close to its resonant state and a quasi-periodic motion is realized. However, the quasi-periodic motion can encounter some instability condition for which the rod trajectory loses the quasi-periodicity character and just converts into a final injection motion. This behaviour change is strongly dependent on the dissipation values and for this reason the critical dataset cannot be effectively evaluated. Finally, the experimental data are reported in a logarithmic scale, in order to highlight the exponential nature of the external length ℓ_m as a function of the excitation frequency f_{ex}.

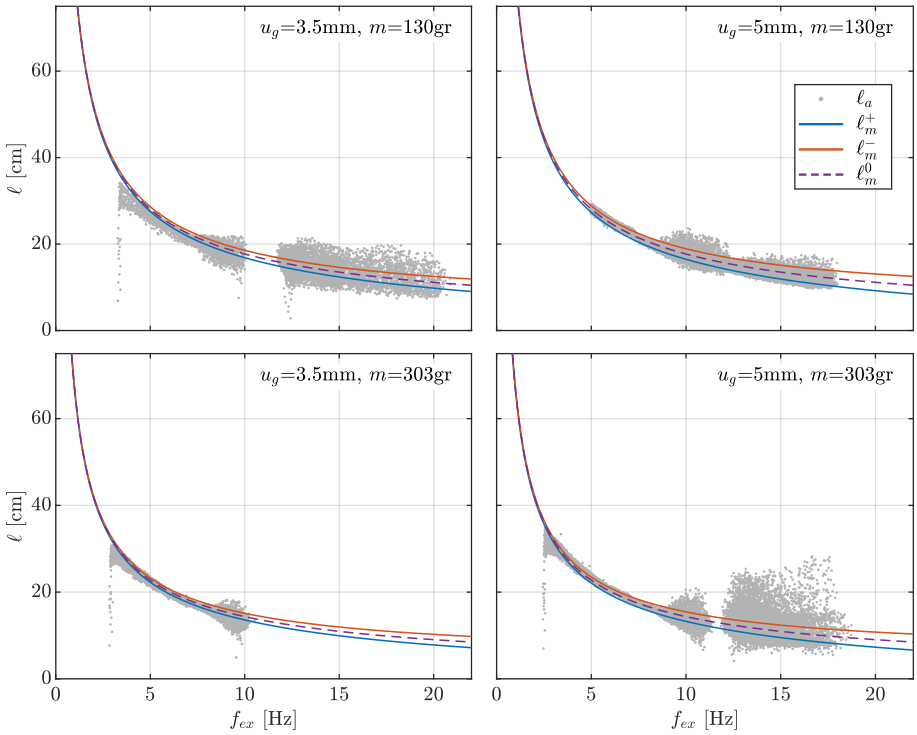

Figure 31: Period-average exterior length of the rod for $m = \{130, 303\}$gr and moving constraint amplitude $u_g = \{3.5, 5\}$mm. The gray points correspond to the measurements from the experiments, the blue and red solid line corresponds to the theoretical prediction of the in-phase and out-of-phase solutions respectively, and the dashed purple line represents the length of the clamped-free rod in its resonant state. Loss of stability can be observed for a range of frequencies, resulting to complete injection of the rod.

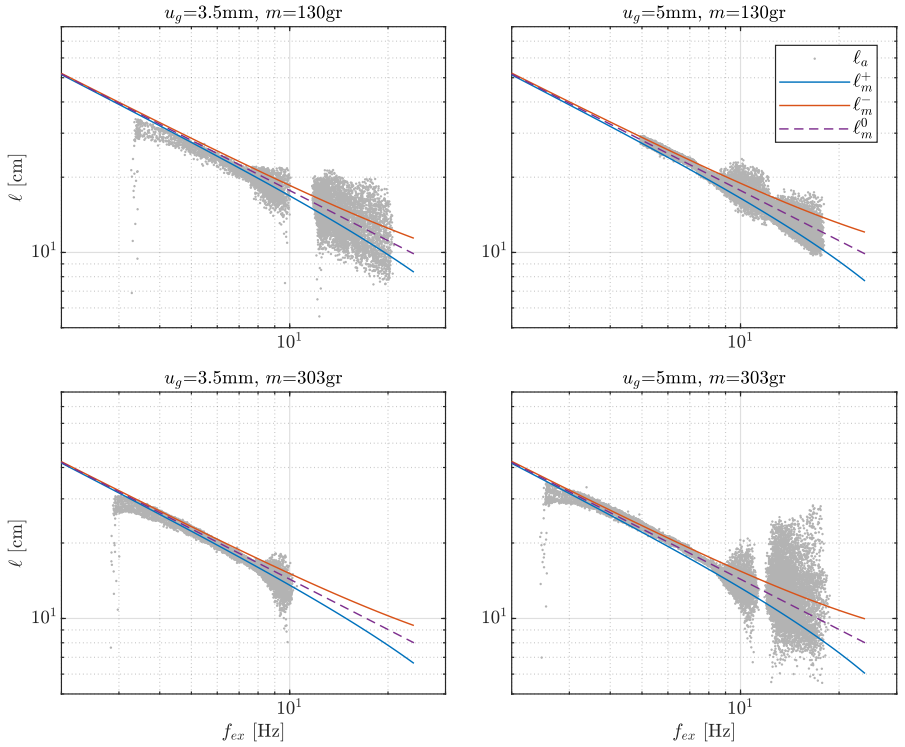

Figure 32: Same as Fig. 31 but in a log-log scale, revealing the exponential trend of the external length ℓ_m as a function of the input frequency f_{ex}.

5 CONCLUSIONS

In the present manuscript two structures with special constraints have been studied.

In Chapter 3, the extensible elastica has been analytically solved with an end constrained to move along a curved frictionless profile (with or without a discontinuous curvature value in correspondence of the straight configuration). The solution for the full non-linear structural response has revealed the following features.

- The values of profile curvature at the origin $f''(0)$ and of axial/flexural stiffness ratio q have a significant effect on the existence, number, and value of the bifurcation loads, which may be compressive or tensile;
- When bifurcation in compression occurs, the system may display a single or a double restabilization of the straight configuration (occurring at large compression, depending on $f''(0)$ and q).

An optimization algorithm has been proposed for the design of the profile shape, to obtain a prescribed post-critical response. The optimization algorithm was positively tested to realize a large variety of load-displacement curves (bilinear, sinusoidal, triangular), useful for applications as force-limiter or other passive mechanisms.

In Chapter 4, the basic structural system of variable-length beam supporting a lumped mass and constrained by an oscillating sliding-sleeve has been studied and an analytical prediction of the dynamic behaviour has been obtained. A position-based model has been formulated and developed to define a finite element framework. An experimental campaign validated the main theoretical predictions, which can be summarized as follows

- Twin asymptotic periodic motions are found around two different values of the average external rod's length ℓ_m.
- The system displays self-tuning properties, meaning that the system attempts to self-adjust its external length ℓ to realize a quasi-periodic motion around the corresponding resonant conditions of

the analogous fixed length rod. The self-tuning occurs successfully only within a certain range of frequency and amplitude parameters.

The present results pave the way to a novel class of resonant metamaterials based on configurational constraints.

FUTURE WORK

The two mechanisms can be used as part of more complex systems, such as building blocks for metamaterials with tunable properties. For example, the sliding hinge system can be used to create mechanical metamaterials with designed stress-strain properties. Such concepts are of great importance to the seismic engineering industry, as well as to high frequency vibration isolation technologies. Moreover, the ability of the sliding-sleeve system to work at resonant conditions for a broad range of frequencies make it important to applications that require high values of damping and energy dissipation. As a result, further work should be directed towards the exploration of possibilities to incorporate the concepts of the sliding-hinge and the sliding-sleeve mechanisms in the framework of mechanical metamaterials for applications in vibration isolation and damping.

In order to facilitate the manufacturing of such novel materials, additive manufacturing techniques could be employed. Multimaterial 3D printing technologies are suitable for large scale manufacturing of microarchitected materials and moving part can be embedded in a lattice without the need of complex assembling processes. More specifically, the adaptation of the sliding-hinge and sliding-sleeve mechanisms in the context of 3D-printed metamaterials is an important step towards practical applications. The reliability and reproducibility of the designed behaviour should be guaranteed when the mechanisms are scaled down and the nonlinear behaviour due to the materials used should be studied.

Moreover, apart from the adaptation of the designs to manufacturing techniques, the mechanisms could be further enhanced. In detail, the sliding-hinge system can be adapted to more complex behaviour, such as an initial zero-stiffness that increases incrementally as the displacement of the clamp is increased, or the implementation of multistability at null load by altering the shape of the curved profile to accommodate multiple points with zero deflection of the rod for non-zero values of the imposed displacement. Concerning the sliding-sleeve system, the possibility to have a self-oscillating system without the need for the additional

mass at the tip of the rod should be explored. Such a system would rely on the distributed mass of the rod in order to realize the self-sustaining motion.

Additional improvements can be considered for the methods used to study the two structures. For example, the numerical framework discussed in the previous chapters should be refined and the limitations can be improved. As a result, the numerical framework will be a robust tool that can assist the design process of technologies evolving from the proposed research.

Concerning the scientific findings during the study of the sliding-hinge system, it was shown that there exist a region in the parameter space of the system in which a double restabilization is observed in the theoretical model. However, in order to highlight the significance of the finding, experimental evidence is required. Therefore, further experimental study of the double restabilization effect is deemed important. In order to obtain a physical model with the properties required to experimentally test this theory, materials with very high compressibility are required and for this reason ideas from the field of microarchitected materials should be adopted.

APPENDIX

A

EXAMPLES OF ONE-DIMENSIONAL STRUCTURES DISPLAYING SMALL VALUES OF STIFFNESS RATIO q

To further substantiate the examples introduced in Sect. 3.1.1, a stiffness ratio evaluation is provided. The evaluation is based on the shear stiffness K_s, axial stiffness K_a (corresponding to K in the main text), and bending stiffness B of the Reissner beam equivalent to a helical spring [33]

$$K_s^{\text{spring}} = \frac{8EI_r L}{\pi n_a D^3}, \qquad K_a^{\text{spring}} = \frac{4GI_T L}{\pi n_a D^3}, \tag{211}$$

$$B^{\text{spring}} = \frac{2EIL}{\pi n_a D\left(1+\frac{EI}{GI_T}\right)}, \tag{212}$$

where E is the Young's modulus, G the shear modulus, I is the moment of inertia of the wire cross-section with respect to the radius of the spring coil passing through the centre of the cross-section, I_r is the moment of inertia of the wire cross-section with respect to the axis perpendicular to the radius passing through the centre of the cross-section, I_T is the torsion constant, L is the length of the spring, D is the coil diameter, and n_a is the number of (active) coils.

The dimensionless axial stiffness parameter q_a (corresponding to q in our manuscript) and shear stiffness parameter q_s are introduced as

$$q_a = \frac{K_a L^2}{\pi^2 B}, \qquad q_s = \frac{K_s L^2}{\pi^2 B}, \tag{213}$$

which reduce for a helical spring to

$$q_a^{\text{spring}} = \frac{2}{\pi^2}\left(1+\frac{GI_T}{EI}\right)\left(\frac{L}{D}\right)^2, \qquad q_s^{\text{spring}} = \frac{2EI_r}{GI_T} q_a^{\text{spring}}. \tag{214}$$

Interestingly, the ratio between the two stiffness ratios is given by

$$\frac{q_a^{\text{spring}}}{q_s^{\text{spring}}} = \frac{GI_T}{2EI_r}. \tag{215}$$

We are now in a position to quantify the value of q for the two cases below.

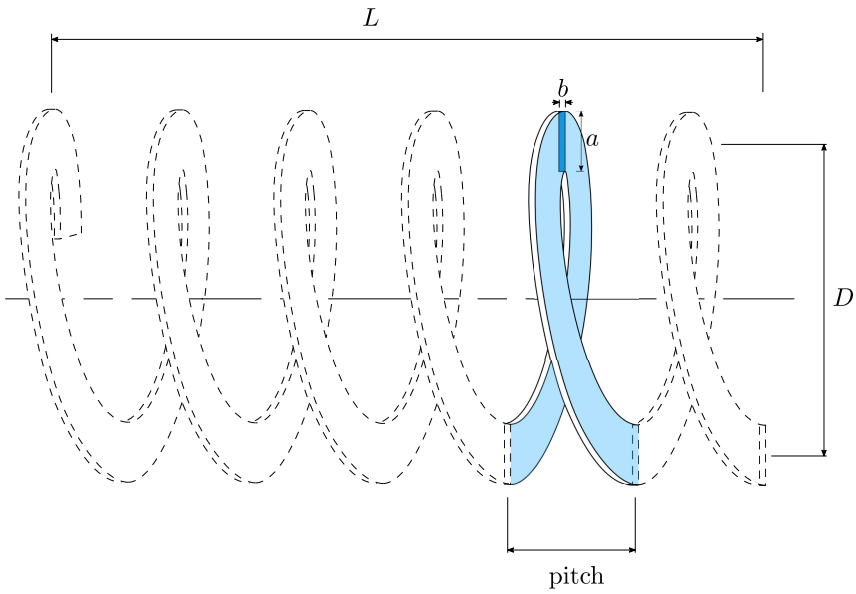

Figure 33: A rectangular wire helical spring realizing an equivalent one-dimensional rod with very small ratios between axial and bending/shear stiffnesses.

A.0.1 *Rectangular wire helical springs*

For a rectangular wire of edges a and b, as illustrated in Fig. 33, the moments of inertia are given by

$$I = \frac{ab^3}{12}, \qquad I_r = \frac{a^3 b}{12}, \tag{216}$$

and, in the considered case $a > b$ the torsion constant by

$$I_T \approx \left[1 - 0.63\frac{b}{a} + 0.052\left(\frac{b}{a}\right)^5\right]\frac{ab^3}{3}. \tag{217}$$

Considering a steel spring ($E = 2.6\,G$, with G being the shear modulus) and characterized by $L = 5D$ (similarly to examples reported in [23, 24, 59]), the stiffness ratios q_a^{spring} and q_s^{spring} are shown in Fig. 34 as increasing functions of the aspect ratio a/b of the rectangular cross section.

Finally, considering for example an aspect ratio $a/b = 8$ and setting the height b of the wire such that the ratio between b and the pitch of the coil is $1/20$, the corresponding spring (shown in Fig. 33) can be compressed up

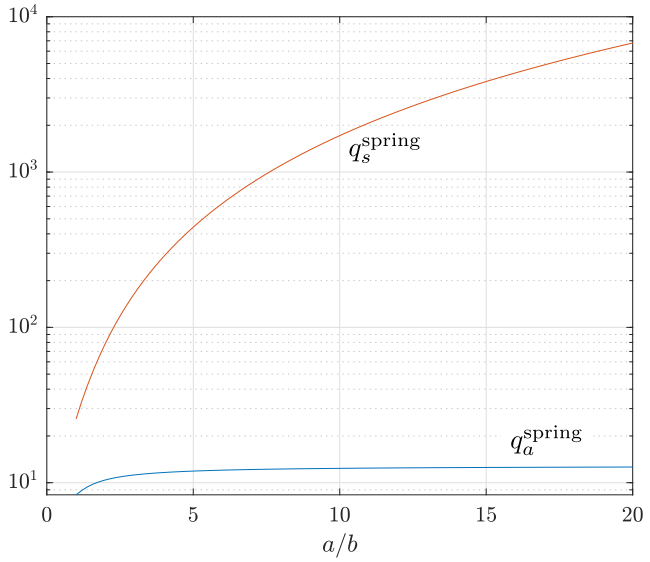

Figure 34: Semi-logarithmic plot of the stiffness ratios q_a^{spring} and q_s^{spring} for a rectangular wire helical spring, as functions of the aspect ratio a/b of the rectangular wire cross-section with $L/D = 5$ (reported in Fig. 33 for $a/b = 8$).

to 95% of its undeformed length and is characterized by the two following stiffness ratios

$$q_a^{\text{spring}} = 1.225 \cdot 10, \quad q_s^{\text{spring}} = 1.103 \cdot 10^3, \tag{218}$$

providing values for an equivalent rod with negligible shear effects and that could be modelled as the extensible elastica.

A.0.2 *Composite rod-spring element*

A helical spring is considered to contain a coaxial elastic rod, as shown in Fig. 35. While one end of the spring is fixed to the corresponding end of the rod, the remaining part of the spring can slide without friction along the rod.[1] Assuming that the spring and the rod react in parallel, the shear and bending stiffnesses of the equivalent one-dimensional element,

1 Although frictionless, the moving boundary problem realized through the relative motion of the spring with respect to the rod may realize configurational forces, whenever a non-null rod's curvature is displayed. Nevertheless, due to their higher-order character, such configurational forces do not affect the buckling analysis and therefore can be neglected [9]. This implies that the double restabilization feature is not compromised, so that only the post-buckling response changes.

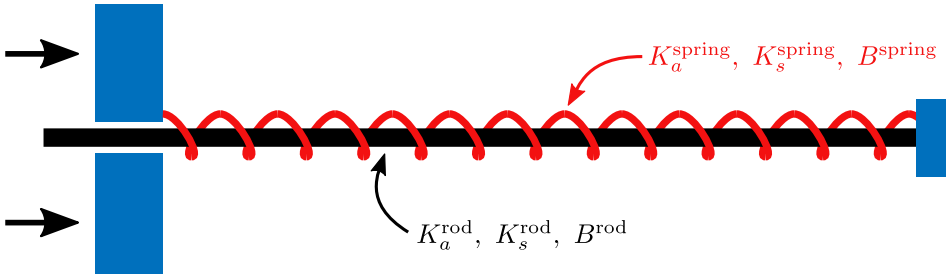

Figure 35: A one-dimensional element working as an axially-deformable elastica, characterized by high shear stiffness ratio q_s but low axial stiffness ratio q_a, obtained as an elastic rod inserted within a helical spring. The spring can slide along the rod so that the latter does not contribute to the axial stiffness of the structure.

working as an axially-deformable elastica, are simply the sum of that of the spring and of the rod, namely

$$K_s = K_s^{\text{rod}} + K_s^{\text{spring}}, \qquad B = B^{\text{rod}} + B^{\text{spring}}, \tag{219}$$

while, considering that loads are applied on the spring, the equivalent axial stiffness coincides with that of the spring because of its frictionless sliding along the rod,

$$K_a = K_a^{\text{spring}}. \tag{220}$$

It follows that the axial stiffness can be tuned independently of the bending and shear stiffnesses, to attain (almost) any pair of desired stiffness ratios q_a and q_s.

As an example for a round wire spring, the axial, shear and bending stiffnesses are given by

$$\begin{aligned} K_a^{\text{spring}} &= \frac{Gd^4L}{8n_aD^3}, \quad K_s^{\text{spring}} = \frac{Ed^4L}{8n_aD^3}, \\ B^{\text{spring}} &= \frac{Ed^4L}{32\left(1+\dfrac{E}{2G}\right)n_aD}, \end{aligned} \tag{221}$$

and for a circular rod of diameter D^{rod} as

$$K_s^{\text{rod}} = \frac{8\pi G\left(D^{\text{rod}}\right)^2}{37}, \quad B^{\text{rod}} = \frac{\pi E\left(D^{\text{rod}}\right)^4}{64}, \tag{222}$$

where for simplicity the rod and the spring have been considered as made up of the same material (differently, the selection of a material for the rod

stiffer than that constituting the spring, $E^{rod} > E^{spring}$ further facilitates satisfaction of the inequality $q_a \ll q_s$ with $q_a \approx 10$). The stiffness ratios of the equivalent one-dimensional element become

$$\begin{aligned} q_a &= \frac{4G}{\pi^2 n_a E \beta}\left(\frac{d}{D}\right)^4\left(\frac{L}{D}\right)^3, \\ q_s &= \frac{1}{\pi^2\beta}\left(\frac{L}{D}\right)^2\left[\frac{4}{n_a}\left(\frac{d}{D}\right)^4\left(\frac{L}{D}\right)+\frac{256\pi G}{37E}\left(\frac{D^{rod}}{D}\right)^2\right], \end{aligned} \tag{223}$$

where

$$\beta = \frac{1}{\left(1+\frac{E}{2G}\right)n_a}\left(\frac{d}{D}\right)^4\left(\frac{L}{D}\right)+\frac{\pi}{2}\left(\frac{D^{rod}}{D}\right)^4. \tag{224}$$

The stiffness ratios described by Eq. (223) are shown in Fig. 36 as monotonic increasing functions of the ratio L/D, by assuming $d/D = 0.1$, $D^{rod}/D = 0.8$ and the pitch of the coil has been selected in order to have 95% maximum compression with respect to the undeformed length. Finally, assuming for example $L/D = 50$, the stiffness ratios are

$$q_a = 1.211 \cdot 10^{-1}, \qquad q_s = 2.107 \cdot 10^3, \tag{225}$$

corresponding to values of an equivalent rod with negligible shear effects and that could be properly modelled through the extensible elastica considered in the present paper.

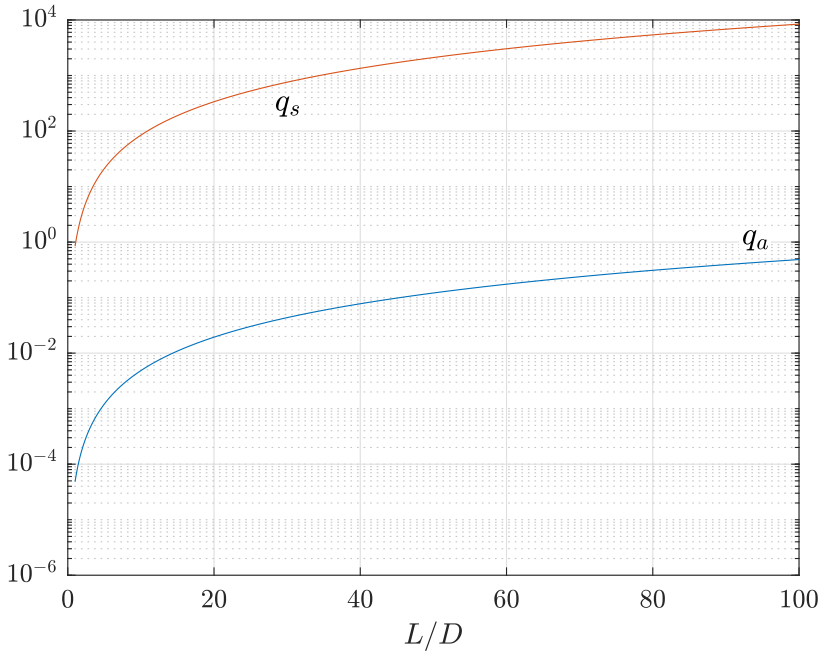

Figure 36: Semi-logarithmic plot of the stiffness ratios q_a and q_s for a composite rod-spring element (Fig. 35) as functions of L/D.

B

ASYMPTOTIC BEHAVIOUR OF BIFURCATION LOAD FOR VANISHING PROFILE CURVATURE AT THE ORIGIN FOR THE SLIDING-HINGE SYSTEM

Asymptotic expressions for the bifurcation load in the limit of vanishing profile curvature at the origin can be obtained by solving the first-order expansion in $f''(0) \to 0^{\pm}$ of Eq. (95). It follows that the critical load under tension has the following singular asymptote[1]

$$\lim_{f''(0)\to 0^-} p_{cr}^{(+)} = -\frac{1}{f''(0)} - 1 - \frac{\operatorname{sgn}(f''(0))}{\pi\sqrt{q}}. \tag{226}$$

Concerning the bifurcation loads under compression, $p \in (-1, 0)$, the asymptotic behaviour determines the presence of two critical loads (corresponding to destabilization and restabilization of the trivial configuration) for a number N of critical modes depending on q. The asymptotic expression for the destabilization $p_{de}^{(-)[n]}$ and restabilization $p_{re}^{(-)[n]}$ loads, pertaining to the n-th mode, results to be a finite value independent of the sign of the profile curvature

$$\begin{aligned}\lim_{f''(0)\to 0^+} \left\{p_{de}^{(-)[n]}, p_{re}^{(-)[n]}\right\} &= \lim_{f''(0)\to 0^-} \left\{p_{de}^{(-)[n]}, p_{re}^{(-)[n]}\right\} \\ &= \frac{1}{2}\left(-1 \pm \frac{\sqrt{-1-4n-4n^2+q}}{\sqrt{q}}\right),\end{aligned} \tag{227}$$

where the number N of existing critical modes is given by

$$N = \max\left\{\left\lfloor \frac{\sqrt{q}-1}{2} \right\rfloor, 0\right\}, \tag{228}$$

with the symbol $\lfloor\cdot\rfloor$ standing for the integer part of the relevant argument.

It is interesting to note that in the limit of $f''(0) \to 0^{\pm}$ the structure reduces to an extensible rod connected to a sliding clamp on its left end and with the right end constrained only in the horizontal direction. In this case, the tensile bifurcation load approaches infinity ($p_{cr}^{(+)} \to \infty$), so that tensile buckling is excluded.

1 The asymptotic expression (226) also holds for p within the (meaningless) range $(-\infty, -1] \cup [0, \infty)$, as it can be appreciated from Fig. 37.

Finally, the compressive bifurcation loads in the inextensible limit ($q \to \infty$) match those pertaining to a cantilever Euler beam (with clamped-free boundary conditions),

$$\lim_{q\to\infty} \left\{ P_{de}^{(-)[n]} \right\} = -\frac{(2n+1)^2\pi^2 B}{4L^2}, \tag{229}$$

while restabilization does not occur because the corresponding load assumes a negative infinite value

$$\lim_{q\to\infty} \left\{ P_{re}^{(-)[n]} \right\} = -\infty. \tag{230}$$

As an example, the bifurcation conditions for the dimensionless load pq with varying the dimensionless radius of profile curvature $1/f''(0)$ are reported in Fig. 37 for $q = 10$ (left) and for $q = 400$ (right). It can be appreciated that the asymptotic behaviour (drawn as dashed lines) for $1/f''(0) \to \pm\infty$ is symmetric in the range $p \in [-1, 0]$, as predicted by Eq. (227), and that only one asymptote exists for $1/f''(0) \to -\infty$ for positive p, as predicted by Eq. (226).

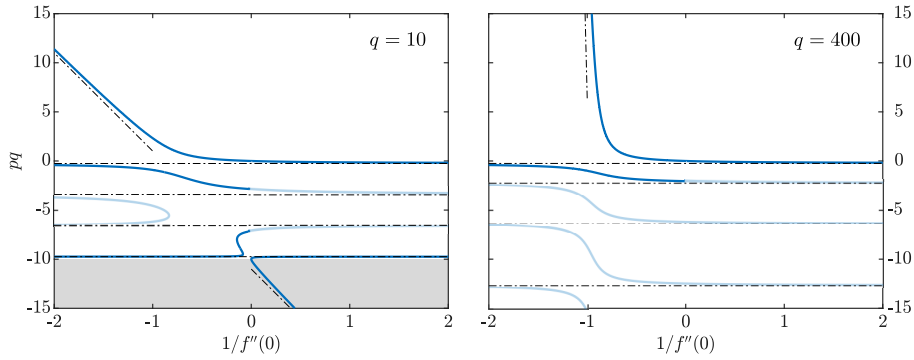

Figure 37: Bifurcation dimensionless load $pq = PL^2/(\pi^2 B)$ as a function of the dimensionless radius of profile curvature at the origin, $1/f''(0)$, for fixed values of q, ($q = 10$ on the left and $q = 400$ on the right). The asymptotic behaviour, Eqs. (226) and (227), is represented by dashed lines.

C

COMPARISON OF NUMERICAL SOLUTION STRATEGIES OF THE DISCRETIZED MODEL OF THE ELASTICA

In order to compare the different choices that can be made regarding the solution of the finite element model of the elastica, a rod attached to a rotating clamp is assumed. The clamp is rotating in a predetermined manner and the system is examined in the quasistatic and dynamic cases. To highlight the fidelity of the present method, the solution of the system is also provided with the solution given in [5], where the solution is given by means of the velocity field of the curve obtained by an implicit Euler scheme, in contrast with the position field in the present method, and the inextensibility is imposed by collocation at the nodes of the discrete model, instead of the Galerkin method opted in the present work.

For the quasistatic case, the convergence of the spatial discretization is compared between the collocation and the Galerkin methods for the satisfaction of the inextensibility condition. The total length of the rod, the moment at the clamp and the angle θ_L at the free end are the three quantities that were selected for the test. The clamp was rotated at an angle $\alpha = \frac{3\pi}{4}$. The results plotted in Fig. 38 show that the Galerkin method shows better convergence characteristics for an increasing number of elements for all three quantities of interest. It is noteworthy that the length is preserved within machine precision even for a very small number of elements; see Fig. 38. For θ_L, where the relative error of the Galerkin approach is 2-3 orders of magnitude smaller than collocation.

In the dynamic case, the clamp is rotated slowly and the rod deforms before it snaps. To highlight the fidelity of the present method, two other numerical schemes were selected for comparison. The first method considered for the comparison is the method of [5], where the solution is the velocity field of the curve obtained by an implicit Euler scheme, in contrast with the position field in the present method, and the inextensibility is imposed by collocation at the nodes of the discrete model instead of the Galerkin method opted in the present work. As the rod snaps, the dynamics of the system as fast, meaning that the velocities involved are much greater than the rotational velocity of the clamp. As a result, the rotating clamp case is ideal for the comparison energy preservation properties of

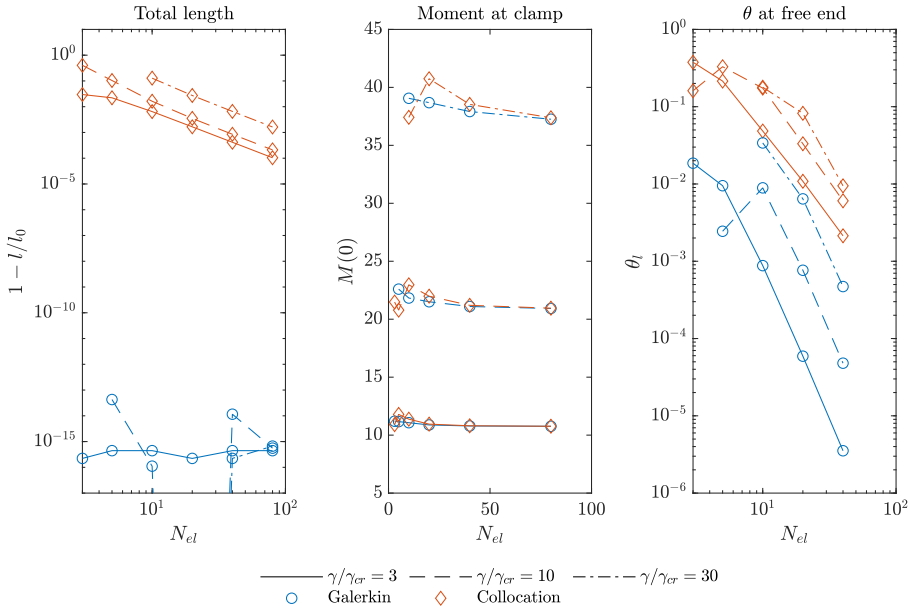

Figure 38: Convergence of the quasistatic rotating-clamp problem for the length L (left), the moment at the clamp M (centre), and the rotation of the free end θ_L (right).

the time-integration schemes; see Fig. 39. Further, the Galerkin method is found to be superior to the collocation method for the preservation of the length of the rod; see Fig. 40.

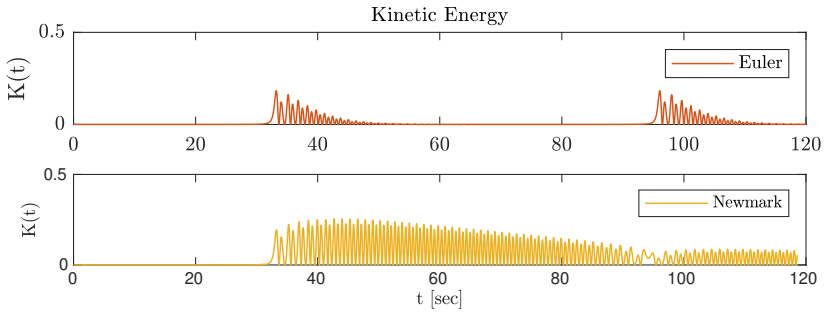

Figure 39: Kinetic energy of the snapping rod as the clamp is rotated. The Implicit Euler and the Newmark methods are compared.

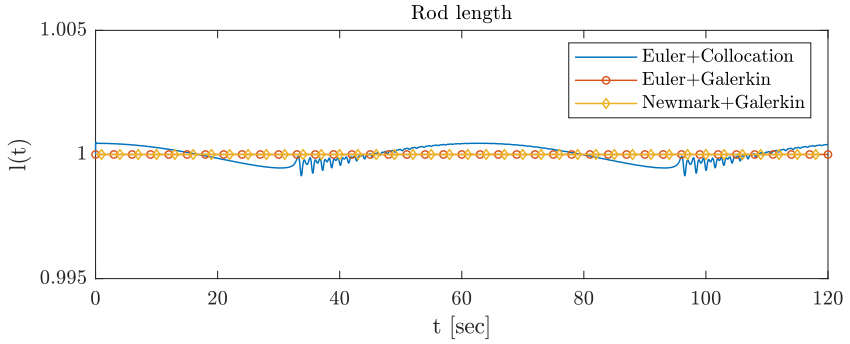

Figure 40: Comparison of the length preservation capabilities of the Collocation and Galerkin methods of the snapping rod as the clamp is rotated.

BIBLIOGRAPHY

[1] P. M. Alabuzhev and E. I. Rivin. *Vibration Protection And Measuring Systems With Quasi-Zero Stiffness*. Applications of Vibration Series. Taylor & Francis, 1989. ISBN: 9780891168119.

[2] I. A. Antoniadis, S. Kanarachos, K. C. Gryllias, and I. E. Sapountzakis. "KDamping: A stiffness based vibration absorption concept." In: *Journal of Vibration and Control* 24 (2018), pp. 588 –606.

[3] C. Armanini, F. Dal Corso, D. Misseroni, and D. Bigoni. "Configurational forces and nonlinear structural dynamics." In: *Journal of the Mechanics and Physics of Solids* 130 (2019), pp. 82–100. ISSN: 0022-5096. DOI: 10.1016/j.jmps.2019.05.009.

[4] K. Avramov and Yu. V. Mikhlin. "Snap-Through Truss as a Vibration Absorber." In: *Journal of Vibration and Control* 10 (2004), pp. 291 –308.

[5] S. Bartels. "A simple scheme for the approximation of elastic vibrations of inextensible curves." In: *IMA Journal of Numerical Analysis* 36.3 (Oct. 2015), pp. 1051–1071. ISSN: 0272-4979. DOI: 10.1093/imanum/drv054.

[6] M. Batista. "A closed-form solution for Reissner planar finite-strain beam using Jacobi elliptic functions." In: *International Journal of Solids and Structures* 87 (2016), pp. 153–166.

[7] F. Bendjellal, G. Walfisch, C. Steyer, J.-Y. F. Bruno, and X. Trosseille. "The combination of a new air bag technology with a belt load limiter." In: *Proc. of the 16th Int. Technical Conf. on the Enhanced Safety of Vehicles*. 1998.

[8] K. Bertoldi, P. M. Reis, S. Willshaw, and T. Mullin. "Negative Poisson's ratio behavior induced by an elastic instability." In: *Advanced materials* 22.3 (2010), pp. 361–366.

[9] D. Bigoni, F. Bosi, F. Dal Corso, and D. Misseroni. "Instability of a penetrating blade." In: *Journal of the Mechanics and Physics of Solids* 64 (2014), pp. 411–425.

[10] D. Bigoni, F. Bosi, D. Misseroni, F. Dal Corso, and G. Noselli. "New phenomena in nonlinear elastic structures: from tensile buckling to configurational forces." In: *Extremely Deformable Structures*. Ed. by D. Bigoni. Vienna: Springer Vienna, 2015, pp. 55–135. ISBN: 978-3-7091-1877-1. DOI: 10.1007/978-3-7091-1877-1_2.

[11] D. Bigoni, D. Misseroni, G. Noselli, and D. Zaccaria. "Effects of the constraint's curvature on structural instability: tensile buckling and multiple bifurcations." In: *Proceedings of the Royal Society A: Mathematical, Physical and Engineering Sciences* 468.2144 (2012), pp. 2191–2209.

[12] F. Bosi, D. Misseroni, F. Dal Corso, and D. Bigoni. "An elastica arm scale." In: *Proceedings of the Royal Society A: Mathematical, Physical and Engineering Sciences* 470.2169 (2014), p. 20140232.

[13] F. Bosi, D. Misseroni, F. Dal Corso, and D. Bigoni. "Development of configurational forces during the injection of an elastic rod." In: *Extreme Mechanics Letters* 4 (2015), pp. 83–88. ISSN: 2352-4316. DOI: 10.1016/j.eml.2015.04.007.

[14] F. Bosi, D. Misseroni, F. Dal Corso, and D. Bigoni. "Self-encapsulation, or the 'dripping'of an elastic rod." In: *Proceedings of the Royal Society A: Mathematical, Physical and Engineering Sciences* 471.2179 (2015), p. 20150195.

[15] F. Bosi, D. Misseroni, F. Dal Corso, S. Neukirch, and D. Bigoni. "Asymptotic self-restabilization of a continuous elastic structure." In: *Phys. Rev. E* 94 (6 2016), p. 063005. DOI: 10.1103/PhysRevE.94.063005.

[16] M. Brojan, D. Terwagne, R. Lagrange, and P. M. Reis. "Wrinkling crystallography on spherical surfaces." In: *Proceedings of the National Academy of Sciences* 112.1 (2015), pp. 14–19.

[17] M. L. Brumbelow, B. C. Baker, and J. M. Nolan. "Effects of seat belt load limiters on driver fatalities in frontal crashes of passenger cars." In: *International Technical Conference on the Enhanced Safety of Vehicles, Paper*. 07-0067. 2007.

[18] A. Carrella, M. J. Brennan, and T. P. Waters. "Static analysis of a passive vibration isolator with quasi-zero-stiffness characteristic." In: *Journal of sound and vibration* 301.3-5 (2007), pp. 678–689.

[19] L. D'Aulerio, G. Whitman, L. Sicher, A. Cantor, and M. Markushewski. "Forensic Performance Analysis of Load-Limiting Devices in Automotive Seat Belt Retractors." In: *Journal of forensic sciences* 64.3 (2019), pp. 754–764.

[20] R. DeSalvo. "Passive, nonlinear, mechanical structures for seismic attenuation." In: (2007).

[21] L. Dong and R. Lakes. "Advanced damper with high stiffness and high hysteresis damping based on negative structural stiffness." In: *International Journal of Solids and Structures* 50.14 (2013), pp. 2416–2423. ISSN: 0020-7683. DOI: 10.1016/j.ijsolstr.2013.03.018.

[22] S. Fang, S. Zhou, D. Yurchenko, T. Yang, and W.-H. Liao. "Multistability phenomenon in signal processing, energy harvesting, composite structures, and metamaterials: A review." In: *Mechanical Systems and Signal Processing* 166 (2022), p. 108419. ISSN: 0888-3270. DOI: 10.1016/j.ymssp.2021.108419.

[23] J. A. Haringx. "On highly compressible helical springs and rubber rods, and their application for vibration-free mountings." In: *Philips Res. Rep.* 3 (1948), pp. 401–449.

[24] J. A. Haringx. "Instability of springs." In: *Philips Tech. Rev.* 11 (1950), pp. 245–251.

[25] N. Hu and R. Burgueño. "Buckling-induced smart applications: recent advances and trends." In: *Smart Materials and Structures* 24.6 (2015), p. 063001. DOI: 10.1088/0964-1726/24/6/063001.

[26] A. Humer. "Elliptic integral solution of the extensible elastica with a variable length under a concentrated force." In: *Acta mechanica* 222.3 (2011), pp. 209–223.

[27] A. Humer. "Exact solutions for the buckling and postbuckling of shear-deformable beams." In: *Acta Mechanica* 224.7 (2013), pp. 1493–1525.

[28] R. A. Ibrahim. "Recent advances in nonlinear passive vibration isolators." In: *Journal of sound and vibration* 314.3-5 (2008), pp. 371–452.

[29] J. C. Ji, Q. Luo, and K. Ye. "Vibration control based metamaterials and origami structures: A state-of-the-art review." In: *Mechanical Systems and Signal Processing* 161 (2021), p. 107945.

[30] L. Jin, R. Khajehtourian, J. Mueller, A. Rafsanjani, V. Tournat, K. Bertoldi, and D. M. Kochmann. "Guided transition waves in multistable mechanical metamaterials." In: *Proceedings of the National Academy of Sciences* 117.5 (2020), pp. 2319–2325.

[31] H. Kalathur and R. S. Lakes. "Column dampers with negative stiffness: high damping at small amplitude." In: *Smart materials and structures* 22.8 (2013), p. 084013.

[32] K. A. Kapasakalis, I. A. Antoniadis, and E. J. Sapountzakis. "KDamper Concept for Base Isolation and Damping of High-Rise Building Structures." In: *Proceedings of the 14th International Conference on Vibration Problems*. Ed. by E. J. Sapountzakis, M. Banerjee, P. Biswas, and E. Inan. Singapore: Springer Singapore, 2021, pp. 265–289. ISBN: 978-981-15-8049-9.

[33] V. Kobelev. *Durability of Springs*. Springer International Publishing, 2021. ISBN: 9783030592530.

[34] P. Koutsogiannakis, D. Bigoni, and F. Dal Corso. "Double restabilization and design of force–displacement response of the extensible elastica with movable constraints." In: *European Journal of Mechanics - A/Solids* (2022), p. 104745. ISSN: 0997-7538. DOI: 10.1016/j.euromechsol.2022.104745.

[35] X. Liu, X. Huang, and H. Hua. "On the characteristics of a quasi-zero stiffness isolator using Euler buckled beam as negative stiffness corrector." In: *Journal of Sound and Vibration* 332.14 (2013), pp. 3359–3376.

[36] J. Ma, J. Song, and Y. Chen. "An origami-inspired structure with graded stiffness." In: *International Journal of Mechanical Sciences* 136 (2018), pp. 134–142.

[37] A. Magnusson, M. Ristinmaa, and C. Ljung. "Behaviour of the extensible elastica solution." In: *International Journal of Solids and Structures* 38.46-47 (2001), pp. 8441–8457.

[38] H. Mori, T. Waters, N. Saotome, T. Nagamine, and Y. Sato. "The effect of beam inclination on the performance of a passive vibration isolator using buckled beams." In: *Journal of Physics: Conference Series*. Vol. 744. 1. IOP Publishing. 2016, p. 012229.

[39] A. Niknam and K. Farhang. "Vibration instability in a large motion bistable compliant mechanism due to stribeck friction." In: *Journal of Vibration and Acoustics* 140.6 (2018).

[40] M. Ohsaki and S. Nishiwaki. "Shape design of pin-jointed multistable compliant mechanisms using snapthrough behavior." In: *Structural and Multidisciplinary Optimization* 30.4 (2005), pp. 327–334.

[41] S. P. Pellegrini, N. Tolou, M. Schenk, and J. L. Herder. "Bistable vibration energy harvesters: a review." In: *Journal of Intelligent Material Systems and Structures* 24.11 (2013), pp. 1303–1312.

[42] Alf Pflüger. *Stabilitätsprobleme der Elastostatik*. Springer-Verlag, 2013.

[43] H. Poincaré. "Sur l'équilibre d'une masse fluide animée d'un mouvement de rotation." In: *Acta Mathematica* 259.380 (1885), pp. 1871–2509. DOI: 10.1007/BF02402204.

[44] A. Rafsanjani and K. Bertoldi. "Buckling-induced kirigami." In: *Physical review letters* 118.8 (2017), p. 084301.

[45] P. M. Reis. "A Perspective on the Revival of Structural (In)Stability With Novel Opportunities for Function: From Buckliphobia to Buckliphilia." In: *Journal of Applied Mechanics* 82.11 (Sept. 2015). ISSN: 0021-8936. DOI: 10.1115/1.4031456.

[46] E. Reissner. "On one-dimensional finite-strain beam theory: the plane problem." In: *Zeitschrift für angewandte Mathematik und Physik ZAMP* 23.5 (1972), pp. 795–804.

[47] E. I. Rivin. *Passive vibration isolation*. Amer Society of Mechanical, 2003.

[48] W. Robertson, R. Wood, B. Cazzolato, and A. Zander. "Zero-stiffness magnetic springs for active vibration isolation." In: (2006).

[49] E. J. Sapountzakis, P. G. Syrimi, I. A. Pantazis, and I. A. Antoniadis. "KDamper concept in seismic isolation of bridges with flexible piers." In: *Engineering Structures* 153 (2017), pp. 525–539.

[50] S. Shan, S. H. Kang, J. R. Raney, P. Wang, L. Fang, F. Candido, J. A. Lewis, and K. Bertoldi. "Multistable architected materials for trapping elastic strain energy." In: *Advanced Materials* 27.29 (2015), pp. 4296–4301.

[51] J. Shim, C. Perdigou, E. R. Chen, K. Bertoldi, and P. M. Reis. "Buckling-induced encapsulation of structured elastic shells under pressure." In: *Proceedings of the National Academy of Sciences* 109.16 (2012), pp. 5978–5983.

[52] J. J. Stoker. *Nonlinear elasticity*. Gordon and Breach, 1968.

[53] S. H. Strogatz. *Nonlinear Dynamics and Chaos: With Applications to Physics, Biology, Chemistry, and Engineering*. Studies in Nonlinearity. Avalon Publishing, 2014. ISBN: 9780813349114.

[54] R. Tao, L. Ji, Y. Li, Z. Wan, W. Hu, W. Wu, B. Liao, L. Ma, and D. Fang. "4D printed origami metamaterials with tunable compression twist behavior and stress-strain curves." In: *Composites Part B: Engineering* 201 (2020), p. 108344. ISSN: 1359-8368. DOI: 10.1016/j.compositesb.2020.108344.

[55] R. Tao, L. Xi, W. Wu, Y. Li, B. Liao, L. Liu, J. Leng, and D. Fang. "4D printed multi-stable metamaterials with mechanically tunable performance." In: *Composite Structures* 252 (2020), p. 112663.

[56] D. Terwagne, M. Brojan, and P. M. Reis. "Smart morphable surfaces for aerodynamic drag control." In: *Advanced materials* 26.38 (2014), pp. 6608–6611.

[57] L. N. Virgin, S. T. Santillan, and R. H. Plaut. "Vibration isolation using extreme geometric nonlinearity." In: *Journal of Sound and Vibration* 315.3 (2008), pp. 721–731.

[58] M. Vladimir and S. Vladimir. "Optical tables vibration isolation during precision measurements." In: *Procedia Engineering* 111 (2015), pp. 561–568.

[59] A. M. Wahl. *Mechanical Springs*. McGraw-Hill, 1963.

[60] S. Waitukaitis, R. Menaut, B. G. Chen, and M. Van Hecke. "Origami multistability: From single vertices to metasheets." In: *Physical review letters* 114.5 (2015), p. 055503.

[61] W. Wang. "Bifurcation." In: *Encyclopedia of Ecology*. Ed. by S. E. Jørgensen and B. D. Fath. Oxford: Academic Press, 2008, pp. 335–345. ISBN: 978-0-08-045405-4. DOI: 10.1016/B978-008045405-4.00176-2.

[62] J. Winterflood, D. G. Blair, and B. Slagmolen. "High performance vibration isolation using springs in Euler column buckling mode." In: *Physics Letters A* 300.2 (2002), pp. 122–130. ISSN: 0375-9601. DOI: 10.1016/S0375-9601(02)00258-X.

[63] S. Xu, Z. Yan, K.-I. Jang, W. Huang, H. Fu, J. Kim, Z. Wei, M. Flavin, J. McCracken, R. Wang, et al. "Assembly of micro/nanomaterials into complex, three-dimensional architectures by compressive buckling." In: *Science* 347.6218 (2015), pp. 154–159.

[64] H. Yang and L. Ma. "Multi-stable mechanical metamaterials by elastic buckling instability." In: *Journal of materials science* 54.4 (2019), pp. 3509–3526.

[65] X. Yu, J. Zhou, H. Liang, Z. Jiang, and L. Wu. "Mechanical metamaterials associated with stiffness, rigidity and compressibility: A brief review." In: *Progress in Materials Science* 94 (2018), pp. 114–173.

[66] D. Zaccaria, D. Bigoni, G. Noselli, and D. Misseroni. "Structures buckling under tensile dead load." In: *Proceedings of the Royal Society A: Mathematical, Physical and Engineering Sciences* 467.2130 (2011), pp. 1686–1700.

[67] Q. Zhang, D. Guo, and G. Hu. "Tailored Mechanical Metamaterials with Programmable Quasi-Zero-Stiffness Features for Full-Band Vibration Isolation." In: *Advanced Functional Materials* 31.33 (2021), p. 2101428.

[68] Y. Zheng, X. Zhang, Y. Luo, B. Yan, and C. Ma. "Design and experiment of a high-static–low-dynamic stiffness isolator using a negative stiffness magnetic spring." In: *Journal of Sound and Vibration* 360 (2016), pp. 31–52.

[69] N. Zhou and K. Liu. "A tunable high-static–low-dynamic stiffness vibration isolator." In: *Journal of Sound and Vibration* 329.9 (2010), pp. 1254–1273.

COLOPHON

This document was typeset using a personalized version of the typographical look-and-feel classicthesis developed by André Miede. The style was inspired by Robert Bringhurst's seminal book on typography "*The Elements of Typographic Style*". classicthesis is available for both LaTeX and LyX:

https://bitbucket.org/amiede/classicthesis/

More info about the author, Panagiotis Koutsogiannakis, can be found on the website:

https://pankouts.com

Although instabilities and large oscillations are traditionally considered as conditions to be avoided in structures, a new design philosophy based on their exploitation towards the achievement of innovative mechanical features has been initiated in the last decade. In this spirit, instabilities are exploited towards the development of systems that can yield designed responses in the post-critical state. Further, the presence of oscillating constraints may allow for a stabilization of the dynamic response. These subjects entail a rich number of phenomena due to the non-linearity, so that the study of such mechanical systems becomes particularly complex, from both points of view of the mechanical modeling and of the computational tools.

Two elastic structures are studied. The first consists of a flexible and extensible rod that is clamped at one end and constrained to slide along a given profile at the other. This feature allows one to study the effect of the axial stiffness of the rod on the tensile buckling of the system and on the compressive restabilization. A very interesting effect is that in a region of parameters double restabilization is found to occur, involving four critical compressive loads. Also, the mechanical system is shown to work as a novel force limiter that does not depend on sacrificial mechanical elements. Further, it is shown that the system can be designed to be multi-stable and suitable for integration in metamaterials.

The second analyzed structure is a flexible but inextensible rod that is partially inserted into a movable rigid sliding sleeve which is kept vertical in a gravitational field. The system is analytically solved and numerically and experimentally investigated, when a horizontal sinusoidal input is prescribed at the sliding sleeve. In order to model the system, novel computational tools are developed, implementing the fully nonlinear inextensibility and kinematic constraints. It is shown that the mathematical model of the system agrees with the experimental data. Further, a study of the inclusion of dissipative terms is developed, to show that a steady motion of the rod can be accomplished by tuning the amplitude or the frequency of the sliding sleeve motion, in contrast with the situation in which a complete injection of the rod inside the sleeve occurs. A special discovery is that by slowly decreasing the frequency of the sleeve motion, the length of the rod outside the sleeve can be increased significantly, paving the way to control the rod’s end trajectory through frequency modulation.

Panagiotis Koutsogiannakis